PHYSIK-DEPARTMENT

Thermal effects in laser-heated freestanding permalloy and multiferroic hybrid structures forming magnonic grating couplers and prototype spin wave multiplexers

Dissertation
von
Florian Brandl

TECHNISCHE UNIVERSITÄT MÜNCHEN

TECHNISCHE UNIVERSITÄT MÜNCHEN
Lehrstuhl für Physik funktionaler Schichtsysteme, E10

Thermal effects in laser-heated freestanding permalloy and multiferroic hybrid structures forming magnonic grating couplers and prototype spin wave multiplexers

Florian Brandl

Vollständiger Abdruck der von der Fakultät für Physik der Technischen Universität München zur Erlangung des akademischen Grades eines

Doktors der Naturwissenschaften

genehmigten Dissertation.

Vorsitzender: Univ.-Prof. Dr. Martin Zacharias
Prüfer der Dissertation:
1. Univ.-Prof. Dr. Dirk Grundler
2. apl. Prof. Dr. Martin S. Brandt

Die Dissertation wurde am 24.07.2014 bei der Technischen Universität München eingereicht und durch die Fakultät für Physik am 01.10.2014 angenommen.

Abstract

Thermal effects in freestanding ferromagnets have been studied. The necessary preparation technique and a laser-based heating setup have been developed. The anisotropic magnetoresistance and the conventional Seebeck effect as well as the anomalous Nernst effect have been found in these structures. A transverse spin Seebeck effect voltage was not resolved. Large in-plane temperature gradients have been realized. In a second part spin waves in multiferroic hybridstructures providing a magnonic crystal have been investigated. Besides large spin wave group velocities, the magnonic grating coupler effect has been found. Furthermore a prototype spin wave multiplexer was realized.

In freitragenden Ferromagneten wurden thermische Effekte untersucht. Die benötigten Präparationstechniken und ein laserbasierter Heizaufbau wurden entwickelt. Der anisotrope Magnetowiderstandseffekt und der konventionelle Seebeck-Effekt, sowie der anomale Nernst-Effekt konnten in diesen Strukturen nachgewiesen werden. Eine Signatur des transversalen Spin Seebeck-Effekts konnte nicht gefunden werden. Es wurden hohe Temperaturgradienten in der Probenebene realisiert. Im zweiten Teil wurden Spinwellen in multiferroischen Hybridstrukturen, die einen magnonischen Kristall bilden, untersucht. Neben hohen Gruppengeschwindigkeiten der Spinwellen wurde der magnonische Gitterkopplungseffekt gefunden. Desweiteren konnte ein Prototyp eines Spinwellenmultiplexers realisiert werden.

Contents

Scientific Collaboration

Parts of this thesis have benefited from scientific collaborations. The following parts have been contributed by the respective collaborators:

- The samples consisting of CoFeB based on $SrTiO_3$ and $BaTiO_3$ have been provided by Prof. Dr. Sebastiaan van Dijken and his group, Aalto University School of Science, Finland.
- Magneto-optic Kerr microscopy has been performed and provided by Kévin Franke, Aalto University School of Science, Finland.
- Micromagnetic simulations have been performed and provided by Sampo Hämäläinen, Aalto University School of Science, Finland.

The author would like to express his gratitude for the productive collaborations.

1. Introduction

In most conventional electronic devices used during the last decades the spins of electrons were ignored and only their charge was relevant. More recently a new field arised attributing the spins of electrons as a carrier of information. This field is called spintronics [Wol01]. The aim of the related research is to utilize spin-dependent effects and possibly combine them with conventional electronics in order to create a new generation of low power consuming devices. First effects are already used in modern technologies, i.e. in read heads of hard drives or in non-volatile memories called MRAM [Teh99]. There, effects like the giant magnetoresistance (GMR) [Bai88, Bin89], awarded with the Nobel prize in physics in 2007, or the tunneling magnetoresistance (TMR) effect [Jul75, Miy95] are used. In order to realize more devices based on spintronics many research groups contribute on several topics. We will introduce and address two topics in the following, spin caloritronics and magnonics.

1.1. Spin caloritronics

Spin caloritronics ('calor', Latin for heat [Bau10a]) deals with the interaction of heat currents and spins [Bau12]. This interaction was already theroretically predicted in 1987 by Johnson et al. [Joh87] but not in the focus of research for many years. The research field was mainly fueled by the discovery of the transverse spin Seebeck effect by Uchida et al. in 2008 [Uch08], where the generation of a pure spin current in the presence of a temperature gradient in a magnetic material is key. The inverse spin Hall effect [Sai06] can then be used to transform a pure spin current [LÖ7, Yan08] to a charge current. This could lead to an efficient way to convert heat in electricity. Besides this many other thermal effects have been subject to intense studies [Boo14]. Some examples are the spin-dependent Peltier effect [Fli12], the planar and anomalous Nernst effect [Sch13a, Yin13] and the longitudinal spin Seebeck effect [Uch10]. Besides the encouraging progress in the field of spin caloritronics it is still under discussion in the community what is the origin of the trans-

verse spin Seebeck effect. Especially the long-range character of the effect led to the assumptions that phonons in the substrate could play a role [Xia10, Jaw10, Jaw11, Uch12]. Accordingly experiments where the bulk substrates were substituted by thin membranes have been performed. Here the transverse spin Seebeck effect was not resolved [Ave12]. In this thesis, we go a step further and investigate the transverse spin Seebeck effect while we exclude the substrate via a new preparation technique for freestanding magnetic stripes with Pt contacts. Besides the exclusion of phonons this has a second positive aspect for the investigations. As the substrate cannot act as a heat sink anymore large temperature gradients are expected. Large gradients provide the basis for pronounced spin caloric transport effects.

1.2. Magnonics

Magnonics deals with the generation, manipulation and detection of spin waves, also called magnons in the particle picture [Blo30, Neu09, Kru10]. Several techniques are used for the investigation of spin waves, i.e. electrically detected ferromagnetic resonance [Gui07, Goe07], Brillouin light scattering [Car97, Dem01, Hil05] or vector network analyzer ferromagnetic resonance [Kal06, Bil07b, Neu08, Neu10]. Recently, reconfigurable magnonic crystals [Shi04, Tac10, Top10, Top11, Din11, Din12] and metamaterials [Hub13b] were shown to be of great interest for the field of magnonics. Magnonic crystals can be created either by the periodic patterning of ferromagnets or by the implementation of periodic domains and show artificially tailored band structures for magnons. It was recently shown by Vogt et al. [Vog14] that magnonic devices can act as spin wave multiplexers providing the possibility to control the propagation path of spin waves. They might therefor provide the basis for future spin logic devices. Additionally Yu et al. [Yu13] demonstrated a grating coupler in a 2D periodic array of magnetic dots in a magnetic matrix that allows the multidirectional emission of short-wavelength spin waves and might be essential in spin wave based electronics. Often the properties of magnonic crystals are controlled via quasi-static magnetic fields or by short field pulses [Ver12]. However, the generation of a magnetic field typically needs the flow of charge and leads to heat dissipation what is in contrast to the need of low power consuming electronic devices. In order to realize

energy-saving devices a new approach might be key. Multiferroic materials [Eer06] are promising as they combine the possibility to control the material properties either by magnetic as well as by electric fields. Examples for multiferroics are hybrid structures of piezoelectric or ferroelectric substrates where a ferromagnetic film is attached [Khi08, Goe08, Rov10]. The application of an electric field to the substrate leads to a strain that causes anisotropies in the ferromagnetic film and changes the ferromagnetic resonance [Bot06, Wei09]. It was recently shown, that ferroelectric $BaTiO_3$ substrates in the tetragonal phase that form a periodic pattern of a_1 and a_2 domains provide a full pattern transfer to a ferromagnetic film attached to the substrate via magnetostriction. A periodic stripe array of alternating anisotropy was realized [Lah11b, Lah11a]. Additionally the application of a large enough electric field was shown to induce a rotation of the anisotropy axis in each stripe [Lah12, Fra12]. So far, for the investigations crystalline magnetic materials like CoFe were used. However, it was shown by Yu et al. [Yu12] that magnetically isotropic, amorphous CoFeB is a promising material for magnonics and that it provides large spin wave group velocities. In this thesis, we aim to merge the promising properties of amorphous $Co_{40}Fe_{40}B_{20}$ with ferroelectrics. The magnetic material is therefor grown on $BaTiO_3$ substrates and we investigate the dynamic properties of the multiferroic system using the vector network analyzer ferromagnetic resonance technique. The periodic stripe pattern of the hybrid structure is found to form a magnonic crystal without patterning the homogeneous ferromagnetic film laterally. With this hybrid structure we aim to combine the low power consuming features of multiferroic devices with the intriguing characteristics of spin wave multiplexers and magnonic grating couplers in one and the same sample.

1.3. Overview of the thesis

The thesis is arranged as follows. In chapter 2 we describe the theoretical background on magnetism, spin waves, magnetic and thermal effects and ferroelectricity. In chapter 3 we introduce the materials used in this study. Afterwards, we will continue in chapter 4 with the explanation on relevant preparation techniques, where we include a full description of a newly developed process for the fabrication of freestanding ferromagnets. In chapter 5 we explain the experimental techniques and methods. We

introduce the all electrical spin wave spectroscopy, a laser-based heating setup and magneto-optic Kerr microscopy. Later, in chapter 6 we discuss our investigations on laser-induced thermal gradients in freestanding ferromagnets. Chapter 7 addresses our findings on multiferroic hybrid structures and deals with the electric field controllability of magnonic effects. We close this thesis with a summary and an outlook in chapter 8.

2. Theory

In this chapter we present an overview on the theoretical background for this thesis. In the beginning we will explain basic properties of magnetism and define relevant energy contributions. We will then discuss the dynamic behavior of magnetization and spin waves. There we will present relevant dispersion relations and an analytical model for spin waves. Afterwards we will give a short overview over thermoelectric and thermomagnetic effects and will end the chapter with a brief description on ferroelectricity. The following sections are described following mainly the Refs. [Blu01, Gur96, Sta09, Kit99, Hil02, Hel76, Mar00, Sko08, Ash76, Bil07a, Neu11a, Dür12, Hub13a, Sch13b, Bie12, O'H99, Lah13].

2.1. Magnetism

Ferromagnets are materials that show a spontaneous magnetization **M** although there is no external magnetic field **H** applied.
In general materials are classified via the magnetic susceptibility $\hat{\chi}$ by

$$\mathbf{M} = \hat{\chi}\mathbf{H}, \tag{2.1}$$

where **M** is the sum of magnetic moments **m** per volume [Cul09]

$$\mathbf{M} = \frac{\mathrm{d}\mathbf{m}}{\mathrm{d}V}. \tag{2.2}$$

The susceptibility $\hat{\chi}$ is a tensor as **M** and **H** do not have to be collinear. For an isotropic material ($\hat{\chi} = \chi$) the value of the susceptibility classifies materials as follows [Hel76]:

$\chi >> 0$	ferro- or ferrimagnet	Both materials show spontaneous magnetization without external field applied. In a ferromagnetic lattice the spins show a parallel alignment. The ferrimagnet consists of two (differently orientated) ferromagnetic sublattices where the overall magnetization does not cancel out. Often ferrimagnetism is based on two lattices of different atoms. Heated above the Curie temperature T_C ferro- and ferrimagnets get paramagnetic.
$\chi > 0$	paramagnet	Paramagnetic materials contain permanent magnetic moments that align with the external field. The interaction between the moments is negligible. Without an external field there is no magnetization left.
$\chi > 0$	antiferromagnet	Here we have a similar set of sublattices of magnetic moments, and the magnetic moments cancel exactly out. For $T \to 0$ and the field applied along an easy axis of a crystal $\chi \approx 0$.
$\chi < 0$	diamagnet	Diamagnets have no permanent magnetic moments. With an applied external field a moment is induced in the electronic shells of atoms that counteracts the external field after the Lenz's law.

Table 2.1.: Classification of magnetic materials depending on the susceptibility χ.

In this study all magnetic materials investigated are ferromagnets ($\chi >> 0$). Solids from the three elements Co, Fe and Ni are ferromagnetic at room temperature. Their alloys are also often ferromagnetic. In this thesis we use $Ni_{80}Fe_{20}$ and $Co_{40}Fe_{40}B_{20}$ (see chapter 3). Here, boron is added for structural reasons. We aim at an amorphous and magnetically isotropic material.
The magnetic flux density **B** is defined as

$$\mathbf{B} = \mu_0(\mathbf{M} + \mathbf{H}) = (\hat{\chi} + 1)\mathbf{H}. \tag{2.3}$$

with μ_0 the permeability in vacuum. $\hat{\chi} + 1$ is defined as permeability $\hat{\mu}$.

2.2. Static magnetization and energies in ferromagnets

The magnetization state of a ferromagnet is determined by an interplay of several energy contributions that we discuss in the following. The knowledge about the magnetization state is essential to describe the dynamics later on. We use the continuum model. There the magnetization is given as the sum of the magnetic moments in the volume. Additionally we will give some energy contributions in polar coordinates for a magnetic thin film in the x-y-plane [Figure 2.1 (a)] with an uniaxial anisotropy in the plane of the film. The polar coordinates are defined in Figure 2.1 (b). The angles θ and θ_H mark the polar angles of the magnetization **M** and the external field **H**, respectively. φ and φ_H are the corresponding azimuthal angles.

Zeeman energy

This contribution is based on the interaction between the magnetization **M** and the external field **H**. The energy density is described by

$$\mathscr{E}_Z = -\frac{\mu_0}{V}\int \mathrm{d}V \mathbf{M}\cdot\mathbf{H}. \tag{2.4}$$

The energy is minimal if the magnetization is aligned with the external field. In polar coordinates and with β the angle between **H** and **M** this energy reads as:

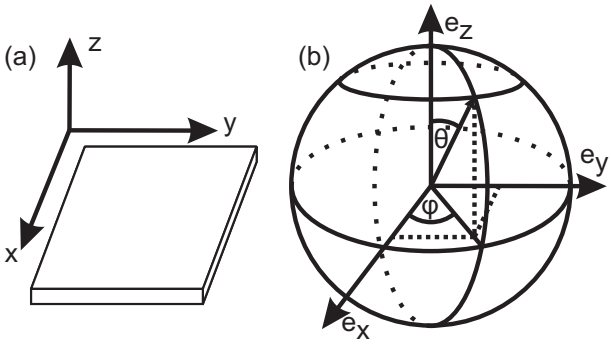

Figure 2.1.: (a) Cartesian coordinate system. Here, the magnetic thin film extends in the x- and y-direction. (b) Definition of the polar coordinates. The azimuthal angle is φ, the polar angle is θ.

$$\begin{aligned} \mathscr{E}_Z &= -\mu_0 |\mathbf{H}| \cdot |\mathbf{M}| \cdot \cos\beta \\ &= -\mu_0 |\mathbf{H}| \cdot |\mathbf{M}| \cdot (\cos\theta \cos\theta_\mathrm{H} + \sin\theta_\mathrm{H} \sin\theta \cos(\varphi - \varphi_\mathrm{H})). \end{aligned} \tag{2.5}$$

Please note that in a large field in particular $|\mathbf{M}| = M_\mathrm{sat}$ with M_sat being the saturation magnetization.

Exchange energy

The exchange interaction has its origin in the Coulomb interaction on the one hand and the Pauli exclusion principle on the other hand [Chi97]. Imagine two atoms with non-paired electrons approach each other. When the spins of these electrons are antiparallel they are allowed to share an orbital state. This increases the Coulomb energy. If the spins are aligned parallel, the Pauli exclusion principle forbids a shared orbit. Separate orbits are formed and the Coulomb energy is decreased. Consequently parallel alignment of neighboring spins $\mathbf{S}_i$ and $\mathbf{S}_j$ is energetically favorable concerning the exchange energy. The energy term for N atoms can be written as

$$\mathscr{E}_{ex} = -\sum_{i,j}^{N} J_{ij}(\mathbf{S}_i \cdot \mathbf{S}_j) = -2\sum_{i<j}^{N} J_{ij}(\mathbf{S}_i \cdot \mathbf{S}_j), \tag{2.6}$$

where J_{ij} is the exchange integral, that quantifies the strength of the interaction. As the interaction strength decreases rapidly with increasing distance between the atoms the summation is often limited to next neighbors. Using the Stoner model [Blu01] the ferromagnetism of itinerant ferromagnets is described. When the density of states $D(E_\mathrm{F})$, with E_F the Fermi energy, is large enough the ferromagnetic ordering is energetically favorable as the increase in kinetic energy is overcompensated by the decrease in Coulomb energy. This is valid for

$$\mu_0 \mu_\mathrm{B}^2 \lambda_\mathrm{St} D(E_\mathrm{F}) \geq 1, \tag{2.7}$$

where λ_St is the average exchange field and $\mu_\mathrm{B} = \frac{e\hbar}{2m_e}$ is the Bohr magneton, describing the magnetic moment of an electron. With a Taylor approximation one can derive an expression for the exchange energy from Eq. 2.6 to be [Gie05]

$$\mathscr{E}_{ex} = \frac{A_\mathrm{ex}}{V} \int (\nabla \cdot \mathbf{M})^2 \mathrm{d}V, \tag{2.8}$$

with A_ex the exchange stiffness.

Demagnetization energy

This contribution comes from the long range dipole-dipole interaction between spins. It reads as

$$\mathscr{E}_\mathrm{dem} = -\frac{\mu_0}{2V} \int \mathrm{d}V \mathbf{M(r)} \cdot \mathbf{H}_\mathrm{dem}(r), \tag{2.9}$$

where $\mathbf{H}_\mathrm{dem}(r)$ is the corresponding position-dependent demagnetization field that is also often called shape anisotropy field as the shape of the body itself is responsible for this contribution. Starting from the Maxwell equations one finds

$$\nabla \cdot \mathbf{B} = \mu_0 \nabla \cdot (\mathbf{M} + \mathbf{H}_\mathrm{dem}) = 0 \quad \text{and} \tag{2.10}$$

$$\nabla \times \mathbf{H}_{\text{dem}} = 0. \tag{2.11}$$

In the general case the calculation of the demagnetizing field is not trivial. However, for the special case of a uniformly magnetized ellipsoid [Aha06] one finds

$$\mathbf{H}_{\text{dem}} = \hat{N}\mathbf{M} \quad \text{and} \quad \mathscr{E}_{\text{dem}} = \frac{\mu_0}{2}\mathbf{M}\hat{N}\mathbf{M}. \tag{2.12}$$

Choosing an appropriate coordinate system the demagnetizing tensor $\hat{N}$ can be diagonalized and reads

$$\hat{N} = \begin{pmatrix} N_x & 0 & 0 \\ 0 & N_y & 0 \\ 0 & 0 & N_z \end{pmatrix}. \tag{2.13}$$

The sum of the diagonal elements of the dimensionless tensor is $N_x + N_y + N_z = 1$. Throughout this thesis we are solely interested in the special case of an infinitely extended film in the x-y plane [Fig. 2.1 (a)] where the elements are given as $N_x = N_y = 0$ and $N_z = 1$. With this we express the demagnetization energy as

$$\mathscr{E}_{\text{dem}} = \frac{\mu_0}{2} M_{\text{sat}}^2 \cos^2\theta. \tag{2.14}$$

Uniaxial anisotropy energy and magnetoelastic energy

A further volume anisotropy contribution might originate from an uniaxial anisotropy term that depends on the direction of the magnetization **M**. A uniaxial anisotropy can be induced in several ways, i.e. by stresses and inverse magnetostriction (see below). At this stage we state the uniaxial anisotropy constant K_{uni} to be a phenomenological parameter. If we choose the x-axis as the direction of the uniaxial anisotropy axis, the energy density is expressed as

$$\mathscr{E}_{uni} = -K_{\text{uni}} m_x^2, \quad \text{with } m_x = \mathbf{M} \cdot \mathbf{e}_x. \tag{2.15}$$

For $K_{\text{uni}} < 0$ the x-axis is a so called hard-axis direction, meaning that the magnetization tries to align in a perpendicular direction. For $K_{\text{uni}} > 0$ the x-axis gets an easy-axis direction and an alignment of the magnetization

with the x-axis is energetically favorable.
In polar coordinates the energy density reads

$$\mathscr{E}_{uni} = -K_{\text{uni}} \sin^2\theta \cos^2\varphi. \tag{2.16}$$

Let us now pick one possible reason for a uniaxial anisotropy, i.e. a mechanical stress giving rise to a magnetoelastic anisotropy. This effect is also known as inverse magnetostriction. The strength of the magnetoelastic anisotropy constant K_{me} depends on the stress σ to the magnetic material and on the material parameter λ_{s} which is the magnetostriction. Following Ref. [O'H99] the anisotropy constant for an isotropic material is given as:

$$K_{me} = -\frac{3}{2}\sigma\lambda_{\text{s}}. \tag{2.17}$$

Most amorphous materials are isotropic in the sense of magnetoelastic anisotropy [Lac82]. The stress σ is connected with the total strain e_{tot} via

$$e_{\text{tot}} = \frac{\sigma}{E_{\text{M}}} + \frac{3}{2}\lambda_{\text{s}}(\cos^2\gamma - \frac{1}{3}), \tag{2.18}$$

where E_{M} is the Young's modulus for fixed magnetization controlling the pure elastic strain (first term). The second term is the magnetostrictive contribution, where γ is the angle between the magnetization and the direction of the strain.
For $\lambda_{\text{s}} > 0$ and $\sigma > 0$ the magnetization is, at least for this contribution, favorably orientated in the direction of the stress. If one of the two parameters is negative the magnetization preferably tilts away from the direction of the stress.

Surface anisotropy energy

Besides the volume anisotropies there exist surface anisotropies. These do usually not occur in bulk ferromagnets but become important for thin films. The anisotropy originates from the fact that atoms lying close to the surface of a magnetic material face a different energetic landscape as atoms in the center of the magnetic material as for surface atoms neighbors in one direction are missing. This anisotropy becomes more and more important

with a decreasing film thickness. The energy density is given as

$$\mathscr{E}_{\perp} = -\frac{K_{\perp}}{d} m_z^2 \tag{2.19}$$

with the film thickness d and the surface anisotropy constant $K_{\perp}$. For ultra thin films ($d \leq 1$ nm) the surface anisotropy can be the dominating contribution and the magnetization turns out of the plane for $K_{\perp} > 0$. This contribution in polar coordinates looks like

$$\mathscr{E}_{\perp} = -\frac{K_{\perp}}{d} \cos^2 \theta \tag{2.20}$$

Total energy

Summing up all contributions we find the total energy density

$$\mathscr{E}_{tot} = \mathscr{E}_Z + \mathscr{E}_{ex} + \mathscr{E}_{\text{dem}} + \mathscr{E}_{\text{uni}} + \mathscr{E}_{\perp}. \tag{2.21}$$

In a ferromagnet the magnetization will align in a way that the total energy is minimal. Thus, the equilibrium position of the magnetization can be calculated. The total energy allows to define an effective field $\mathbf{H}_{\text{eff}}$ as [Gil04]

$$\mathbf{H}_{\text{eff}} = -\frac{1}{\mu_0} \nabla_{\mathbf{M}} \mathscr{E}_{tot}. \tag{2.22}$$

In the static case the magnetization $\mathbf{M}$ is collinear with the effective field $\mathbf{H}_{\text{eff}}$. We will see in the next section that a displacement of the magnetization leads to a precession of the magnetization. The precession axis is collinear with the direction of the effective field $\mathbf{H}_{\text{eff}}$.

2.3. Magnetization dynamics

2.3.1. Landau-Lifshitz-Gilbert equation

In the previous section we discussed static effects in ferromagnets and introduced the effective magnetic field $\mathbf{H}_{\text{eff}}$. Let us now introduce a dynamical model. We consider all the magnetic moments to be represented by a macrospin, i.e. the magnetization vector $\mathbf{M}$. An equation proposed by Landau and Lifshitz in 1935 [Lan35] is given as:

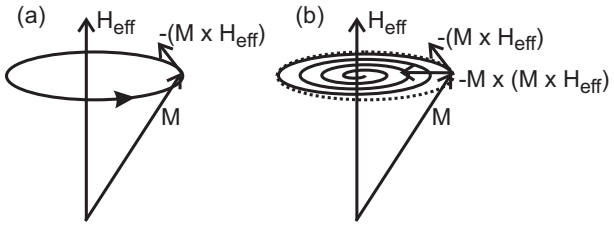

Figure 2.2.: The macrospin precesses around the effective field $\mathbf{H}_{\text{eff}}$ (a). Adding the phenomenological damping causes the macrospin to align with the effective field in a spiral way (b). The length of vector $\mathbf{M}$ is assumed to be constant.

$$\frac{d\mathbf{M}}{dt} = -\gamma\mu_0\mathbf{M} \times \mathbf{H}_{\text{eff}} \tag{2.23}$$

with $\gamma = g|e|/(2m_e) \approx 176 \cdot 10^9$ GHz/T being the gyromagnetic ratio for a free electron. e and m_e are the charge and the mass of a free electron and $g \approx 2.002$ is the electron g-factor. A displacement of the magnetization from the direction of the effective field results in a torque and a continuous precession of the magnetization (cf. Fig. 2.2 (a)). However, this behavior is not observed in the real sample. Instead, relaxation takes place. A phenomenological damping term is introduced. Landau and Lifshitz proposed the modified precession equation as:

$$\frac{d\mathbf{M}}{dt} = -\gamma\mu_0\mathbf{M} \times \mathbf{H}_{\text{eff}} - \frac{\lambda}{M_{\text{sat}}}\mathbf{M} \times (\mathbf{M} \times \mathbf{H}_{\text{eff}}) \tag{2.24}$$

where λ is a damping parameter. Additionally to the precessional torque on the macrospin, a torque component points towards the center of the circular motion. The resulting picture is a spiral-like precession [cf. Fig. 2.2 (b)], so that the magnetization aligns with the effective field after a certain time. However, it was found that the Landau-Lifshitz damping term is not valid for large λ. Hence, Gilbert suggested another phenomenological damping term [Gil04]. This results in the Landau-Lifshitz-Gilbert equation:

$$\frac{d\mathbf{M}}{dt} = -\frac{\gamma\mu_0}{1+\alpha^2}\mathbf{M} \times \mathbf{H}_{\text{eff}} - \frac{\gamma\mu_0\alpha}{M_{\text{sat}}(1+\alpha^2)}\mathbf{M} \times (\mathbf{M} \times \mathbf{H}_{\text{eff}}) \tag{2.25}$$

with α the damping parameter. For low damping equations 2.24 and 2.25 are equal. A simplification for Eq. 2.25 is valid for low damping:

$$\frac{d\mathbf{M}}{dt} = -\gamma\mu_0\mathbf{M}\times\mathbf{H}_{\text{eff}} - \frac{\gamma\mu_0\alpha}{M_{\text{sat}}}\mathbf{M}\times(\mathbf{M}\times\mathbf{H}_{\text{eff}}) \ . \tag{2.26}$$

All materials used in this thesis show low damping ($\alpha \approx 10^{-2} - 10^{-3}$).

2.3.2. Dynamic susceptibility and ferromagnetic resonance

The dynamic susceptibility connects the dynamic magnetization $\mathbf{m}(t)$ with the excitation magnetic field $\mathbf{h}_{\text{rf}}(t)$:

$$\mathbf{m} = \hat{\chi}(\omega)\mathbf{h}_{\text{rf}} = (\hat{\chi}' - \mathrm{i}\hat{\chi}'')\mathbf{h}_{\text{rf}} \ . \tag{2.27}$$

In the following we need some assumptions: First, the static parts, the magnetization and the magnetic field, lie in the x direction. Second, the absolute value of $\mathbf{M}$ is constant and the dynamic parts are in the y and z direction:

$$\mathbf{H}_{\text{ext}} = \begin{pmatrix} H_{\text{ext}} \\ h_y(t) \\ h_z(t) \end{pmatrix} \quad , \quad \mathbf{M} = \begin{pmatrix} M \\ m_y(t) \\ m_z(t) \end{pmatrix} \ . \tag{2.28}$$

We consider a thin film without anisotropies except for demagnetization effects. The effective field then reads $\mathbf{H}_{\text{eff}} = \mathbf{H}_{\text{ext}} - \hat{N}\mathbf{M}$. For now, we will not use the simplified demagnetization tensor for a thin film. Instead, we use the general diagonalized form. We get the effective field as

$$\mathbf{H}_{\text{eff}} = \begin{pmatrix} H_{\text{ext}} - N_x M_{\text{sat}} \\ h_y(t) - N_y m_y(t) \\ h_z(t) - N_z m_z(t) \end{pmatrix} \ . \tag{2.29}$$

If we assume harmonic time dependencies $\mathbf{h}(t) = \mathbf{h}\ \exp(\mathrm{i}\omega t)$ and $\mathbf{m}(t) = \mathbf{m}\ \exp(\mathrm{i}\omega t)$ and consider equations 2.26, 2.27 and 2.29 together with Ref. [Gie05] the following expressions for the real and imaginary parts of the susceptibility (exemplarily for the y-components) can be given:

$$\chi'_{yy} = \frac{\omega_M(\omega_0^2 - \omega^2)(\omega_H + (N_z - N_x)\omega_M)}{(\omega_0^2 - \omega^2)^2 + \alpha^2\omega^2\left[2\omega_H + (N_y + N_z - 2N_x)\omega_M\right]^2} + \frac{\alpha^2\omega^2\left[2\omega_H + (N_y + N_z - 2N_x)\omega_M\right]}{(\omega_0^2 - \omega^2)^2 + \alpha^2\omega^2\left[2\omega_H + (N_y + N_z - 2N_x)\omega_M\right]^2} \tag{2.30}$$

and

$$\chi''_{yy} = \alpha\omega\omega_M \left[\frac{(\omega_0^2 - \omega^2)}{(\omega_0^2 - \omega^2)^2 + \alpha^2\omega^2\left[2\omega_H + (N_y + N_z - 2N_x)\omega_M\right]^2} + \frac{(\omega_H + (N_z - N_x)\omega_M)(2\omega_H + (N_y + N_z - 2N_x)\omega_M)}{(\omega_0^2 - \omega^2)^2 + \alpha^2\omega^2\left[2\omega_H + (N_y + N_z - 2N_x)\omega_M\right]^2} \right]. \tag{2.31}$$

Here, we use $\omega_M = \gamma\mu_0 M_{\text{sat}}$ and $\omega_H = \gamma\mu_0 H_{\text{ext}}$.
ω_0 is defined as:

$$\omega_0^2 = (\omega_H + (N_y - N_x)\omega_M)(\omega_H + (N_z - N_x)\omega_M)\,. \tag{2.32}$$

The imaginary part can be approximated by a Lorentzian function. The full width half maximum (FWHM) Δf of this Lorentzian is linked with the damping parameter α. We will discuss this dependency later.
The frequency f_{res} where the Lorentzian exhibits a maximum is called the ferromagnetic resonance (FMR) frequency. By rewriting Eq. 2.32 we state the Kittel formula:

$$f_{\text{res}} = \frac{\gamma\mu_0}{2\pi}\sqrt{(H_{\text{ext}} + (N_y - N_z)M_{\text{sat}})(H_{\text{ext}} + (N_z - N_x)M_{\text{sat}})}\,. \tag{2.33}$$

This formula is valid for homogeneously magnetized ferromagnets. For the case of a thin film in the *x*-*y* plane and the external magnetic field as well as the magnetization pointing in the film plane we get the FMR frequency by inserting the demagnetization tensor ($N_x = 0,\ N_y = 0$ and $N_z = 1$) in Eq. 2.33. For the case of an external magnetic field pointing perpendicular to the film plane we would have to adjust Eq. 2.28 and redo

the whole formalism. Or, even simpler, we rewrite the demagnetization tensor according to $N_x = 1,\ N_y = 0$ and $N_z = 0$.
For the two different geometries we get the following resonance frequencies:

In-plane magnetic field:

$$f_{\text{res}} = \frac{\gamma\mu_0}{2\pi}\sqrt{H_{\text{ext}}(H_{\text{ext}} + M_{\text{sat}})} \tag{2.34}$$

Out-of-plane magnetic field larger than the saturation magnetization:

$$f_{\text{res}} = \frac{\gamma\mu_0}{2\pi}(H_{\text{ext}} - M_{\text{sat}}) \tag{2.35}$$

In the presence of a surface anisotropy the relevant magnetization term in the above-noted expressions changes from the saturation magnetization M_{sat} to the effective magnetization $M_{\text{eff}} = M_{\text{sat}} - \frac{2K_{\text{sur}}}{d\mu_0 M_{\text{sat}}}$ [Bil07a].

Linewidth and damping

The relation between Δf and α can be given following Kalarickal et al. [Kal06]. For the out-of-plane geometry the Kittel formula is provided by Eq. 2.35. The linewidth Δf for a frequency-sweep experiment is connected to the linewidth ΔH observed in a magnetic field sweep experiment by [Kal06]:

$$\Delta f = \Delta H \frac{\delta f_{\text{res}}(H_{\text{ext}})}{\delta\,(H_{\text{ext}})} = \frac{|\gamma|}{2\pi}\mu_0 \Delta H \quad . \tag{2.36}$$

This equation has been discussed by Patton [Pat68] and by Kuanr et al. [Kua05]. Equation 2.36 would have to be extended by a field-dragging term [Far13] if magnetic anisotropies are present. The additional contribution depends on the angle between the magnetization and the external field. However, even in the case of an anisotropy the angle between **M** and **H** vanishes if the field is applied in an easy or hard axis direction (cp. Figure 2.5). The field-dragging term can then be neglected. In general the linewidth ΔH in equation 2.36 consists of two parts:

$$\Delta H = \Delta H_0 + \frac{4\pi\alpha f}{\gamma} \quad . \tag{2.37}$$

The linewidth can be separated into the frequency (f) independent linewidth ΔH_0 and an intrinsic Gilbert-like contribution [Liu03]. ΔH_0 consists of several contributions:

$$\Delta H_0 = \Delta H_{\text{mae}} + \Delta H_{\text{mos}} + \Delta H_{\text{inhom}} + \Delta H_{\delta k} + \Delta H_{\text{2magnon}} + ... \quad (2.38)$$

where ΔH_{mae} is attributed to the magnetic anisotropy. ΔH_{mos} is the contribution of mosaicity. This part has to be considered if the magnetic material is no mono-crystal. All the materials investigated in this thesis are not mono-crystalline. ΔH_{inhom} can be caused by inhomogeneities in the external magnetic field. $\Delta H_{\delta k}$ occurs when the excitation is not limited to a single wave vector but consists of a finite distribution of several wave vectors. We will see later, that in our specific case the excitation is not limited to a single wave vector. The last contribution we discuss is $\Delta H_{\text{2magnon}}$ which is caused by two-magnon scattering. This originates in a scattering process where a uniform precession magnon ($k = 0$) is annihilated and a $k \neq 0$ magnon is created [Bil07a]. Bland and Heinrich [Bla05] and Landeros, Arias and Mills [Lan08] have however shown, that for a large magnetic field perpendicular to the film plane the two-magnon scattering contribution can be neglected.
Inserting Eq. 2.37 in Eq. 2.36 we get:

$$\Delta f = \frac{\gamma}{2\pi}\mu_0 \Delta H_0 + 2\alpha f \ . \quad (2.39)$$

The frequency linewidth Δf is linearly increasing with the resonance frequency f. The damping parameter α is given as half the slope of a straight line when plotting Δf as a function of f. The y axis intercept of the corresponding straight line provides the frequency independent contributions to the linewidth shown in Eq. 2.38.

2.4. Spin waves

So far, we addressed the uniform magnetization precession. The magnetic moments precess at the same frequency and same phase. This corresponds to a wave with infinite wavelength, i.e. wave vector $k = 0$. Now, we focus on excitations with finite wavelength. This collective excitation of spins is called a spin wave, or in a quantized scheme magnons. A sketch

of a spin wave with finite wavelength is given in Fig. 2.3. We will give a short introduction on magnetostatic spin waves. In the following we will neglect exchange interaction as the wavelengths we consider in this thesis are much larger than the relevant length scale for the exchange interaction.

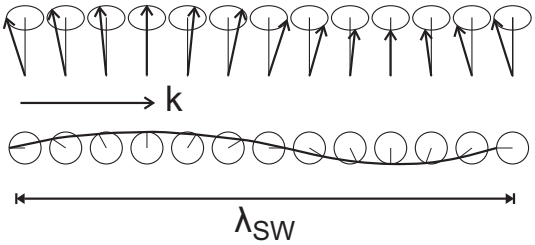

Figure 2.3.: Spin wave in a one-dimensional chain of spins. The wavelength λ_{SW} and the direction of k are defined for $\mathbf{M} \perp \mathbf{k}$.

We start with the Maxwell equations in the magnetostatic limit [Gur96]:

$$\nabla \times \mathbf{H} = 0 \ ; \quad \nabla \cdot \mathbf{B} = 0 \ ; \quad \nabla \times \mathbf{E} = -\dot{\mathbf{B}} \ . \tag{2.40}$$

The magnetic induction is given by:

$$\mathbf{B} = \mu_0(1 + \hat{\chi})\mathbf{H} \ . \tag{2.41}$$

Introducing the magnetostatic scalar potential Ψ with $\mathbf{H} = -\nabla\Psi$, we can write [Wal57, Sta09]:

$$(1 + \chi)\left[\frac{\partial^2\Psi}{\partial x^2} + \frac{\partial^2\Psi}{\partial y^2}\right] + \frac{\partial^2\Psi}{\partial z^2} = 0 \ , \tag{2.42}$$

where χ is assumed to be position independent. Equation 2.42 is based only on the magnetostatic equations (first two equations in Eq. 2.40). Therefor solutions of Eq. 2.42 are usually called magnetostatic modes. However, please note that they are not totally static as high frequency variations are taken into account. Assuming that $\Psi \propto \exp(ik \cdot r)$, it follows the connection between the susceptibility (that depends on the frequency) and the wave vector:

$$(1 + \chi)(k_x^2 + k_y^2) + k_z^2 = 0 \ . \tag{2.43}$$

Hereby, we assume the component k_z perpendicular to the expansion direction of the film to be quantized due to the confinement in the thin film of thickness d:

$$|k_z| = n\frac{\pi}{d},\ n \in \mathbb{N}\ . \tag{2.44}$$

We will only consider waves in the *x*-*y* plane and therefor set $n = 0$.
We determine the group and phase velocities of the waves as

$$v_{group} = \frac{\partial\omega}{\partial k}\ ;\quad v_{phase} = \frac{\omega}{k}\ ,\ \text{with}\ \omega = 2\pi f\ . \tag{2.45}$$

In the following we will give an overview on three special kinds of magnetostatic waves given by Ref. [Sta09]. The modes are determined by the angle between the magnetization and the film plane and the angle between the magnetization and the in-plane wave vector $\left(k_{||} = \sqrt{k_x^2 + k_y^2}\right)$. Here, we neglect anisotropies and again exchange interaction.

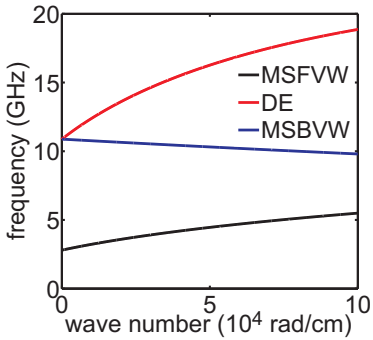

Figure 2.4.: Calculated spin wave dispersions for three magnetostatic waves. The parameters, used for calculation are: $\mu_0 M_{\text{sat}} = 1.41$ T, $H_{\text{ext}} = 0.1$ T and $d = 47$ nm.

- **Magnetostatic Surface Waves (MSSW)**:
  As these waves were described by Damon and Eshbach for the first time [Dam61], they are also called Damon-Eshbach (DE) modes. These modes occur when the magnetization is perpendicular to the

wave vector $k_{||}$ and lies in the film plane. The dispersion relation is given by [Sta09]:

$$\omega^2_{\text{MSSW}} = \omega_H(\omega_H + \omega_M) + \frac{\omega_M^2}{4}(1 - e^{-2k_{||}d}) \ . \tag{2.46}$$

For the case $k_{||} \to 0$ we find Eq. 2.32. The MSSW is called a surface mode as the wave amplitude is not distributed equally through the whole film. Instead, the amplitude decays exponentially with increasing distance to the surface of the film. As the group and phase velocities point in the same direction, this wave is a forward wave.

- **Magnetostatic Backward Volume Waves (MSBVW)**:
  These waves appear when the magnetization lies in the film plane and points parallel to the wave vector. These are called backward waves as the group and phase velocities point in opposite directions. The wave is called a volume wave as the amplitude is distributed throughout the whole volume of the sample. The dispersion relation reads [Sta09]:

$$\omega^2_{\text{MSBVW}} = \omega_H \left[\omega_H + \omega_M \left(\frac{1 - e^{-k_{||}d}}{k_{||}d}\right)\right] \ . \tag{2.47}$$

  Again, for $k_{||} \to 0$ we find Eq. 2.32.

- **Magnetostatic Forward Volume Waves (MSFVW)**:
  These modes occur when the magnetization is perpendicular to the film plane. They are also called forward waves because the group and the phase velocity point in the same direction like for a MSSW. The wave amplitude is distributed through the whole volume (volume wave). The dispersion does not depend on the direction $k_{||}$ if anisotropies are not relevant. The wave propagates isotropically in the plane of the film. The dispersion relation $\omega(k)$ reads as [Sta09]:

$$\omega^2_{\text{MSFVW}} = \omega_H \left[\omega_H + \omega_M \left(1 - \frac{1 - e^{-k_{||}d}}{k_{||}d}\right)\right] \ . \tag{2.48}$$

The aforementioned three special cases are plotted in Fig. 2.4. We see that the MSFVW and DE modes increase in frequency with rising k (positive

group velocity) while the BVMSW shows a negative velocity. These three special cases are helpful for the investigation of isotropic ferromagnetic thin films. However, if we want to model spin waves in films with arbitrary anisotropies we follow a different formalism. Hillebrands [Zhu05, Car00] therefor introduces an effective energy density $\mathscr{E}_{\text{eff}}$ consisting of all anisotropies except the demagnetizing field. For the discussion later in chapter 7 the relevant contributions are given as

$$\mathscr{E}_{\text{eff}} = \mathscr{E}_{\text{uni}} + \mathscr{E}_{\perp}. \tag{2.49}$$

In general a formalism describing spin wave dispersions with arbitrary anisotropy is not trivial and needs numerical methods. However, in the case of in-plane magnetized thin films, where $d \cdot k_{||} \ll 1$ is valid, an analytical formula is given by [Hil05]:

$$\begin{aligned}\left(\frac{\omega}{\gamma}\right)^2 = &\left(\frac{1}{M_{\text{sat}}}\frac{\partial^2 \mathscr{E}_{\text{eff}}}{\partial\theta^2} + H_{\text{ext}}\cos(\varphi-\varphi_{\text{H}}) + \frac{2A_{\text{ex}}}{M_{\text{sat}}}k^2\right.\\ &+ 4\pi M_{\text{sat}} f' \cdot \left(1 - \frac{1}{2}k_{||}d\right)\Bigg) \times \left(\frac{1}{M_{\text{sat}}}\frac{\partial^2 \mathscr{E}_{\text{eff}}}{\partial\varphi^2} + H_{\text{ext}}\cos(\varphi-\varphi_{\text{H}})\right.\\ &\left.+ \frac{2A_{\text{ex}}}{M_{\text{sat}}}k^2 + 2\pi M_{\text{sat}} f' k_{||} d \sin^2(\varphi-\varphi_{\text{H}})\right) - \frac{1}{M_{\text{sat}}^2}\left(\frac{\partial^2 \mathscr{E}_{\text{eff}}}{\partial\theta\partial\varphi}\right)^2.\end{aligned} \tag{2.50}$$

Here, $k^2 = k_{||}^2 + k_z^2$ is the total wave vector and f' is the demagnetizing factor with $f' \approx 1$ for the film thicknesses used in this thesis. f' is different from 1 only for ultra thin films on the order of a few mono layers [Hei88]. Please note that the equation has been reproduced in cgs units whereas all previous equations are defined in SI units.

The terms $\frac{\partial^2 \mathscr{E}_{\text{eff}}}{\partial\theta^2}$, $\frac{\partial^2 \mathscr{E}_{\text{eff}}}{\partial\varphi^2}$ and $\frac{\partial^2 \mathscr{E}_{\text{eff}}}{\partial\theta\partial\varphi}$ can be calculated with Eq. 2.16, 2.20 and 2.49.

2.4.1. Plane film model

The formalism given in equation 2.50 has been introduced to determine relevant anisotropy constants from measured spectra [Hil05]. This formalism

requires the knowledge about the angles φ and θ. They are calculated by minimizing the total energy density given in equation 2.21 for both angles. In the presence of a uniaxial anisotropy the direction of the magnetization depends on the strength and the direction of the external field as well as the strength of the anisotropy. In the following we show an example of a possible dependency $\varphi(\varphi_H)$. Let us assume a 47 nm thick ferromagnetic film in the x-y-plane and the external field applied in the plane of the film. The uniaxial anisotropy axis is along the x-axis and $K_{\text{uni}} > 0$. Consequently, θ and θ_H are both close to 90°. First, we define the anisotropy field H_{uni} as [Gur96]

$$H_{\text{uni}} = \frac{K_{\text{uni}}}{M_{\text{sat}}}. \tag{2.51}$$

In Figure 2.5 we plot the angle φ of the magnetization as a function of the external field angle φ_H for several ratios of $H_{\text{ext}}/H_{\text{uni}}$.

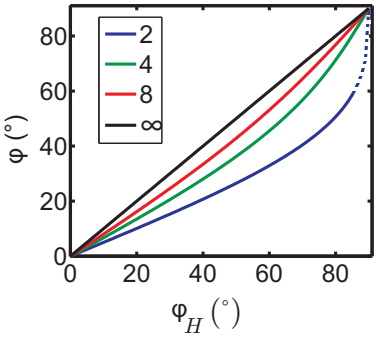

Figure 2.5.: Angle of the magnetization φ as a function of the magnetic field angle φ_H for several ratios of $H_{\text{ext}}/H_{\text{uni}}$. Field and magnetization are in the plane of the sample. The dashed line stands for a configuration that is not realized as domains are likely to form [Gur96].

For an infinitely large field $\varphi(\varphi_H)$ is a straight line. The magnetization points in the same direction as the external field. If the external field is decreased the magnetization direction varies from the direction of the field for angles $0° < \varphi_H < 90°$. The deviation gets large for small fields. Only if the field is applied along an easy or a hard axis $\mathbf{M}$ coincides with $\mathbf{H}_{\text{ext}}$

if $H_{\text{ext}}/H_{\text{uni}} > 2$ [Gur96]. The dashed line in Figure 2.5 indicates that this solution is not relevant as no uniform magnetization is given for these values. Instead domain formation takes place [Gur96].

With the knowledge about the magnetization direction we can use Eq. 2.50 to calculate the resonance frequencies for in-plane fields. Hereby, we have three free parameters: the external field angle φ_H, the field strength H_{ext} and the in-plane wave vector $k_{||}$. In general we choose one parameter as a sweep parameter while the other two values are fixed. The plane-film-model is valid for an infinitely extended film and does not consider any contributions of the shape of the ferromagnet except the finite thickness.

2.4.2. Micromagnetic simulations

In this thesis micromagnetic simulations are shown that were performed by Sampo Hämäläinen from the group of Prof. S. van Dijken at Aalto University, Finland. In the following we will give a short overview on the simulations.
The calculations were done by the simulation software OOMMF (Object Oriented Micromagnetic Framework). The ferromagnet is divided into a mesh of simulation cells within each the magnetization is uniform. An external field and anisotropies can be added for each simulation cell and boundary conditions can be chosen. First of all, the equilibrium position of the magnetization **M(r)** is calculated for each cell by minimizing all energy contributions. This enters the LLG equation (Eq. 2.26) as the ground state. For the dynamic simulations the LLG equation has to be solved numerically. An excitation pulse (here a step pulse) is added for a fixed time that displaces the magnetization vector in each cell. The drop time of the pulse is set to 20 ps making simulations up to 26.5 GHz - like achievable in the experiment - possible. After the application of the pulse the dynamic simulations are performed for 5 ns. A data set $\mathbf{M}(\mathbf{r}, t)$ is generated. The time-dependent simulation results are transformed to the frequency domain in order to be compared with experimental results. A phase-sensitive Fourier transformation of the out-of-plane component of the magnetization is performed providing amplitude and phase of the magnetization oscillation in each cell.

2.5. Magnetic and thermal effects

So far, we have concentrated on energies in ferromagnets and the effect of high frequency displacement of the magnetization. In the following we focus on the Anisotropic Magnetoresistance (AMR), the Seebeck effect, the Spin Seebeck effect (SSE) and close this section with the Anomalous Nernst effect (ANE).

2.5.1. Anisotropic Magnetoresistance

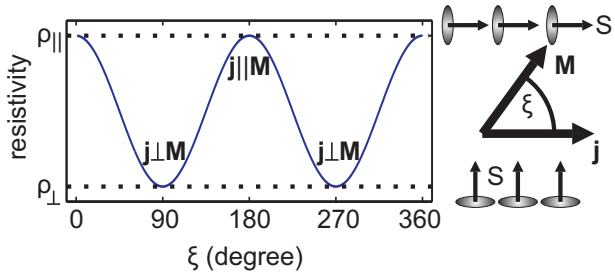

Figure 2.6.: AMR resistivity as a function of the angle between current direction and magnetization. The resistivity is at maximum if the current is collinear with the magnetization. On the right side, the orbitals are sketched that are relevant for the assumed spin-dependent scattering.

In 1865 W. Thomson found in a piece of nickel that in the presence of a magnetic field, the conductivity of the metallic magnet depended on the relative alignment of field and electric current [Tho57]. It was found that the resistivity reached a maximum for a collinear orientation of the magnetization **M** and the current density **j** and a minimum if they pointed perpendicular (Fig. 2.6). The dependency is described by [McG75]

$$\rho(\alpha) = \rho_{\perp} + (\rho_{||} - \rho_{\perp}) \cos^2 \xi, \tag{2.52}$$

where ξ is the angle between the direction of the current **j** and the direction of the magnetization **M**. The change in resistance can be on the order of some percent of the total resistance. Today there is a descriptive explanation for the AMR effect. The origin lies in the spin-orbit coupling. For 3d-ferromagnets the charge distribution in the orbitals is not a sphere but

is deformed in one direction (cp. right side of Fig. 2.6). The orientation of these orbitals in space depends on the direction of the spin. The origin of the AMR is now based on the scattering cross section that is different for electrons approaching the deformed orbitals from different directions. This varies the relevant scattering cross section as a function of angle ξ.

2.5.2. Thermoelectric effect (Seebeck effect)

The Seebeck effect was discovered in 1821 by Thomas Johann Seebeck when he found that a compass needle was deflected by a pair of two metals that touch in two points. The two junctions however were at different temperatures. As Seebeck did not realize that this effect is due to an electric current he called the finding thermomagnetic effect. Later the term was corrected in thermoelectric effect. The origin of the effect is the following: If a metal is heated at one side the Fermi-Dirac distribution function is broadened at the hot side [Bau12]. Energy states above the Fermi energy are occupied by hot electrons. Furthermore holes remain below the Fermi energy. Both hot electrons and hot holes diffuse to the cold side. The conductivity is however dependent on the energy and is larger for higher energy. This leads to a net charge flow towards the cold side as the electron current is larger than the hole current. The increase in charge at the cold end causes an electric field between the two ends. Then the electric field $\mathbf{E}$ can be given as [Ash76]:

$$\mathbf{E} = S\nabla T \tag{2.53}$$

where S is the Seebeck coefficient or Thermopower and ∇T is the temperature gradient. S can be written as:

$$S = -\frac{\pi^2}{3}\frac{k_B^2 T}{e}\frac{\sigma'}{\sigma}. \tag{2.54}$$

Here, k_B is the Boltzmann constant, σ is the conductivity and σ' is its derivative after the energy.

Although the Seebeck effect is present in a single piece of metal, it is hard to be measured on the individual material due to the following reason. Imagine a single metal rod, hot at the one end, cold at the other. If you would like to measure the voltage along the rod, it has to be contacted for

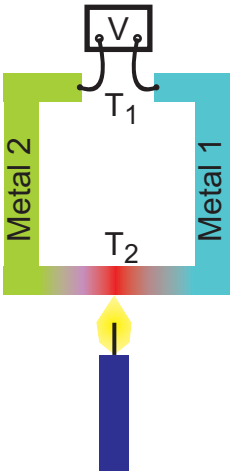

Figure 2.7.: Seebeck effect: Two metals exhibiting different Seebeck coefficients are in contact at two places. One junction is heated, the other one is connected via a voltmeter. A net voltage is measured.

example by two metal probe tips connected to a voltmeter. However, the probe tips would experience different temperatures and exhibit the Seebeck effect themselves. Instead a thermoelectric device usually consists of a pair of metals, i.e. a thermocouple (Fig. 2.7). There two different metals are connected at two points. One junction is heated (T_2) and the cold sides (T_1) are connected via a voltmeter. The measured voltage is given by [Hel76]

$$V = -\int_{T_1}^{T_2} (S_1 - S_2)\mathrm{d}T \tag{2.55}$$

with S_1 and S_2 the Seebeck coefficients of metal 1 and metal 2. For small enough temperature gradients and a constant Seebeck coefficient equation 2.55 simplifies to

$$V = -(S_1 - S_2)\Delta T, \quad \text{where } \Delta T = T_2 - T_1. \tag{2.56}$$

2.5.3. Transversal spin Seebeck effect

The transversal spin Seebeck effect (TSSE) was introduced in 2008 by Uchida et al. [Uch08] and gained remarkable interest in the community. The authors stated that in a thin film ferromagnet that is subject to a heat gradient ∇T in the plane of the sample there is a spin current $\mathbf{j}_s$ generated along the temperature gradient. A spin current is defined in analogy to a charge current as a flow of spin angular momentum. A pure spin current therefor means that there is a transport of spins without a net flow of charge. As a spin current can not be detected directly, the measurement is based on the inverse process of the Spin Hall effect [Sai06, Kim07, Mos10]. Therefor a piece of normal metal (NM) is attached to the ferromagnet. The conversion of spin to charge current takes place when the spin current with the spin polarization vector $\boldsymbol{\sigma}_s || \mathbf{M}$ enters the NM and follows the equation

$$\mathbf{j}_c = D_{\text{ISHE}}\, \mathbf{j}_s \times \boldsymbol{\sigma}_s. \tag{2.57}$$

D_{ISHE} is a measure for the conversion efficiency that depends on the spin-orbit coupling in the material. Often Pt is used for an NM as it shows a large D_{ISHE}.

Uchida et al. [Uch08] explained the spin Seebeck effect due to the fact that spin-up and spin-down conduction electrons exhibit different scattering rates and densities and thus concluded that this is equivalent to different Seebeck coefficients for the two different kinds of spin. Consequently the effect was called spin Seebeck effect. More precise they postulated that the spin current resulted from a difference in the chemical potential for spin-up and spin-down electrons at each end of the ferromagnet due to the temperature gradient. In Fig. 2.8 (a) we show an excerpt of the original publication of Uchida et al. by which the authors aimed at explaining the observations. The spin current is generated along the temperature gradient in the sample plane. At the cold and the hot end, Pt stripes are attached perpendicular to the temperature gradient. The spin current diffuses into the Pt layer and is spin dependently separated (ISHE). As there is an imbalance in the ratio of spin-up and spin-down electrons at each side the electric field built up in the Pt stripes is opposite for the cold and the hot end respectively. As it can be seen from equation 2.57 the measureable

voltage along the Pt stripes depends on the cross product of spin current direction and spin polarization direction. The relevant spin current always flows out of the sample plane across the boundary of NM/FM. The spin polarization direction is dependent on the magnetization direction. Imagine an external field large enough to fully saturate the magnet in the plane of the sample. When rotating the field both the magnetization and the spin polarization vector follow the external field. When the field is applied along the temperature gradient, so perpendicular to the long axis of the Pt stripes, the electric field due to the ISHE is along the Pt stripe. Hence the measureable voltage value is at its maximum [Fig. 2.8 (b)]. By rotating the magnetic field by 90 degree, E_{ISHE} is pointing perpendicular to the Pt stripes and is therefor not detectable along the long axis. A full rotation of the magnetic field therefor yields a sinusoidal response in the voltage signal. At the two ends of the FM, so with a temperature gradient pointing in the opposite direction, the detected voltages are opposite.

However, the microscopic origin of the detected voltages is still not understood and was strongly debated in the community for the last years. Especially the long range character of the detected signal that is orders of magnitude larger than the spin diffusion length gives rise to the assumption that the effect is based on phonons in the substrate [Jaw10, Jaw11, Xia10, Uch12, Hua12]. A second assumption is that another effect, the anomalous Nernst effect (see next section) that is based on an out-of-plane temperature gradient, is mimicking the TSSE signal. Both effects show the same field and angular dependencies if the field is applied in the plane of the sample. However, for the anomalous Nernst effect an out-of-plane temperature gradient is relevant, while for TSSE in-plane gradients contribute to the voltage. Both assumptions were subject to further investigations. A common experiment is based on thin membranes taken as a substrate [Ave12, Sch13a]. This should reduce the influence of phonons in the substrate and the influence of the substrate as a heat sink. The latter should prevent unwanted temperature gradients in the out-of-plane direction. However, in such experimental approaches a TSSE was not resolved. This even more fueled the discussion if the TSSE works like predicted or if it exists at all. In chapter 6 we will contribute a piece to the puzzle by completely excluding the substrate in the heated region. We will show data on freestanding ferromagnets and perform investigations on the TSSE.

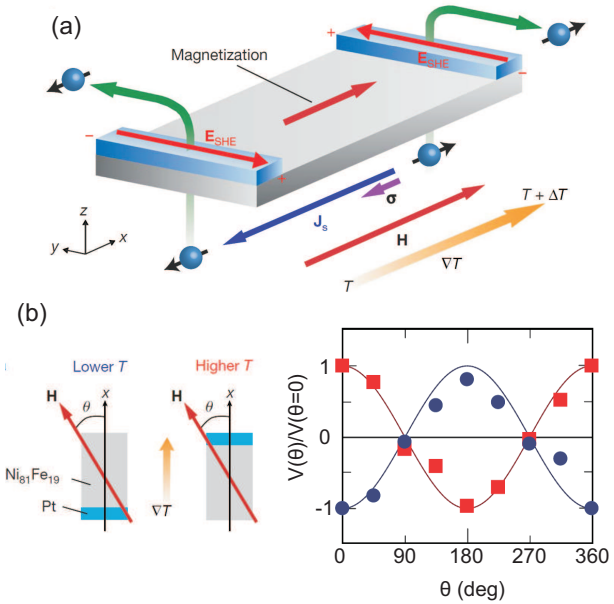

Figure 2.8.: (a) Sketch of the transverse spin Seebeck effect geometry. Pt stripes (blue) are attached to the ferromagnetic film (grey) that is subject to a temperature gradient ∇T. (b) The voltage measured along the Pt stripes depends on the orientation of the magnetization. At the lower and the higher temperature end the resulting voltage is opposite. Pictures taken and adapted from Ref. [Uch08]

2.5.4. (Anomalous) Nernst effect

The Seebeck effect that we previously explained is a thermoelectric effect. We now focus on a thermomagnetic effect, the Nernst effect (NE) [Ner87]. We start from a metal that is subject to a temperature gradient ∇T. Equivalent to the Seebeck effect (section 2.5.2) the heat gives rise to a broadening of the Fermi-Dirac distribution. This leads to a net flow of charge from one end to the other. These charges are electrons from energy states above the Fermi energy as well as holes below the Fermi energy. If we now apply a magnetic field **H** perpendicular to the gradient the Lorentz force will act on the moving charge carriers and separate the holes from the electrons. The upcoming electric field can be written as:

$$\mathbf{E}_{\mathrm{NE}} = N\ \mu_0 \mathbf{H} \times \boldsymbol{\nabla} T, \tag{2.58}$$

with N being the Nernst coefficient.

If the metal is ferromagnetic the heat gradient gives rise to an electric field, too. However the separation of the charge carriers is dependent on the magnetization **M** instead of the external field. This effect is called Anomalous Nernst effect (ANE). Equation 2.58 then changes to

$$\mathbf{E}_{\mathrm{ANE}} = N_{\mathrm{ANE}}\ \mu_0 \mathbf{M} \times \boldsymbol{\nabla} T \tag{2.59}$$

with N_{ANE} being the anomalous Nernst coefficient. Even if the phenomenological description of NE and ANE might offer similarities, the origin is different. It was recently shown, that the ANE is of the same origin as the anomalous Hall effect (AHE) [Miy07]. The AHE however generates a voltage perpendicular to both, the current in a ferromagnet and the field applied normal to the current. It is based on the transverse Hall conductivity σ_{xy}. The reasons for the AHE are of intrinsic (inter-band effect [Kar54] and skew scattering [Smi55, Smi58]) and extrinsic (side-jump [Ber70] and Berry phase [Mac04]) nature. For a detailed consideration of microscopic aspects the interested reader is referred to Ref. [Nag10]. For data analysis we will make use of equation 2.59.

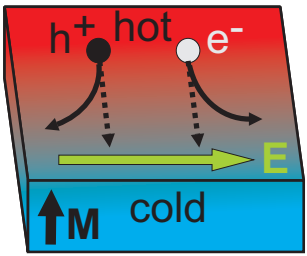

Figure 2.9.: Sketch of the anomalous Nernst effect. A ferromagnetic metal is subject to a temperature gradient. Holes and electrons diffuse from the hot to the cold side and the charges are separated due to the Lorentz force. An electric field builds up perpendicular to **M** and ∇T.

2.6. Ferroelectricity

In the following basic characteristics of ferroelectric materials are discussed. So far, we have discussed the response of a material subject to a magnetic field. If we apply an electric field to a material positive and negative ions might be displaced causing dipole moments. The polarization **P** (in analogy to the magnetization) is defined as the vector sum of microscopic dipole moments per volume. A polarization is shown by every material. A spontaneous polarization is observable in crystals belonging to special symmetry classes [Hel76]. 20 of the 32 point groups do not have an inversion center and show an electric polarization under the influence of a mechanical distortion. They are piezoelectric. This also means that they show a mechanical deformation when an electric field is applied to the material. 10 of these 20 classes have exactly one polar axis and exhibit macroscopic polarization without an applied electric field or strain. The spontaneous polarization depends on the temperature known as pyroelectricity. The polarization of some of the pyroelectric materials can be switched by a sufficiently large electric field **E** applied in the opposite direction. These materials are called ferroelectric. A typical example for a ferroelectric material is $BaTiO_3$ (see chapter 3). The ferroelectricity has an upper temperature limit, the ferroelectric Curie temperature T_C. Furthermore, specific temperatures exist below T_C where the crystal phase and the electrical properties change.

In general for piezoelectric materials the components of the polarization **P** are given as [Jos95]

$$P_i = d_{ijk} X_{jk} + \chi_{ij} E_j, \tag{2.60}$$

where $i \in \{x, y, z\}$ and the summation of j and k runs over x, y, z. d_{ijk} is the 3-dimensional piezoelectric strain coefficient tensor, X_{jk} is the applied mechanical stress tensor, χ_{ij} is the dielectric susceptibility tensor and E_j is the external electric field component.

In section 2.2 we discussed stress-induced contributions to the total energy of a ferromagnet entering the effective field H_{eff} and thereby modifying the spin dynamics. In the course of this thesis we investigated ferroelectric/ferromagnetic heterostructures to implement electric-field control of

magnonic properties. We will discuss in chapter 3 the special properties of the ferroelectric $BaTiO_3$ substrates used in this thesis in detail.

3. Materials

In this chapter we will give an overview over the materials used in this thesis. We will start with a description of the ferroelectric material barium titanate. Furthermore we will introduce the magnetic materials permalloy and cobalt iron boron.

3.1. Barium titanate

3.1.1. Structure

Barium titanate ($BaTiO_3$) is a material that is ferroelectric, pyroelectric as well as piezoelectric. Due to its large dielectric constant, $BaTiO_3$ is often used in capacitors. Above 1460°C it is of a non-ferroelectric hexagonal form [Jaf71]. Below this temperature it crystallizes in the perovskite structure (Figure 3.1) which is ferroelectric for certain temperatures. In the center of the cube there is a Ti^{4+} ion, on the corners Ba^{2+} ions are located and in the center of the faces there are O^{2-} ions. The crystal shows some phase transitions from the cubic structure to the tetragonal, orthorhombic and rhombohedral structure depending on the temperature. The forms of the unit cell and the temperature-dependent phase transition diagram are shown in Figures 3.2 and 3.3 respectively.

Above about 120°C the relevant form is the cubic structure with edge length a. If the temperature is decreased the cell of the perovskite elongates along one edge ($c > a$) and forms a tetragonal lattice. The polarization **P** points parallel to an edge of length c. Cooling down even further the next transition takes place around 0°C. The structure gets orthorhombic as the unit cell elongates along a face diagonal ($b' = c' > a$) and the polarization **P** points in the same direction. At even lower temperatures below -90°C the crystal elongates along a room diagonal and forms a rhombohedral structure where all edges are of length a. The polarization is orientated along the room diagonal.

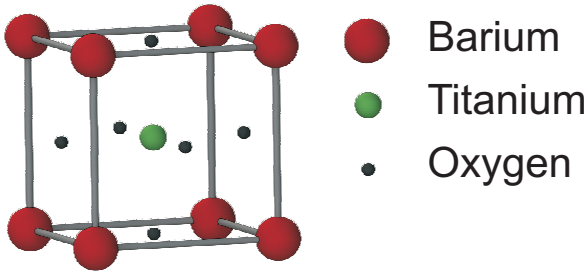

Figure 3.1.: Sketch of the perovskite structure of $BaTiO_3$. The center of the cube is a Ti^{4+} ion, on the corners there are Ba^{2+} ions in the center of the faces O^{2-} ions are located.

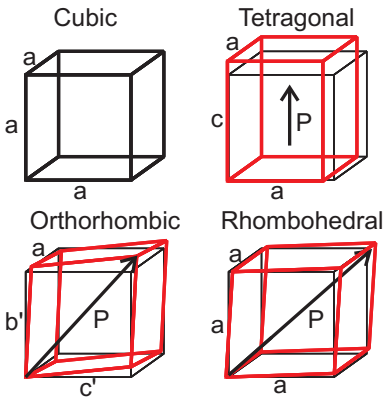

Figure 3.2.: Sketch of the four structures that occur in $BaTiO_3$. The cubic structure shows no polarization, for the tetragonal, orthorhombic and rhombohedral case the polarization direction is drawn with a black arrow. The deviation of the cubic structure (black) is drawn as a red cell.

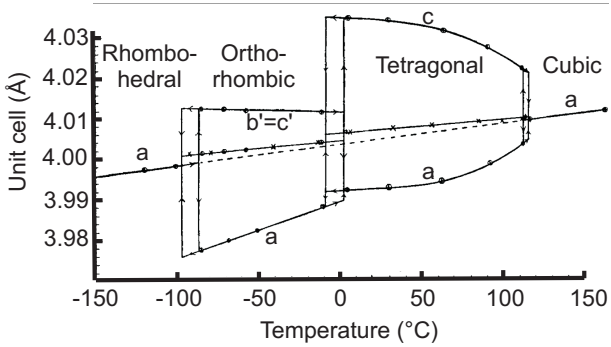

Figure 3.3.: Phase transitions of the $BaTiO_3$ crystal as a function of temperature. The relevant lattice parameters are given. Figure taken and adapted from Ref. [Kay49].

3.1.2. Ferroelectric domains and ferroelectric/ferromagnetic hybridstructures

In ferroelectric substrates it was shown that it can be energetically favorable to form domain patterns [Pom93]. A domain describes a region in a ferroelectric material where the polarization **P** in neighboring cells is parallel. If several domains with different orientation of **P** exist in a substrate the polarization has to change the direction at some point. The change does not take place abruptly between neighboring cells but the direction changes successively over a few cells. The area between neighboring domains where the polarization change takes place is called ferroelectric domain wall.
There are several possible domain configurations, i.e. $180°$ domain walls [Per95] where the polarization is out-of-plane and is rotated by $180°$ in neighboring domains or $90°$ domain walls [PÖ99] where the in-plane polarization is organized in a head-to-tail configuration with an angle of $90°$. The $BaTiO_3$ substrates used in this thesis belong to the latter case and form a regular pattern of a_1 and a_2 domains with a domain width of $5-8$ µm (see Figure 3.4). The polarization of both a_1 and a_2 domains enclose an angle of $45°$ with the domain boundary, the domain wall. **P** originates in an elongation of the lattice in the tetragonal phase which amounts to about $+1.1\%$ (cp. Figure 3.3). If a magnetic film is attached to the ferroelectric substrate

the strain due to the lattice elongation might induce a uniaxial anisotropy in the magnetic film because of magnetostriction (cp. section 2.2). The ferroelectric regular domain patterning is transferred to the ferromagnet. Ferromagnetic domain walls exist as well but are not under investigation in this thesis. However, the ferromagnetic domain walls are wider than the ferroelectric domain walls and can be charged, if the magnetization points head-to-head, or uncharged, if the magnetization points head-to-tail. The kind of domain wall can be changed by the magnetic history.

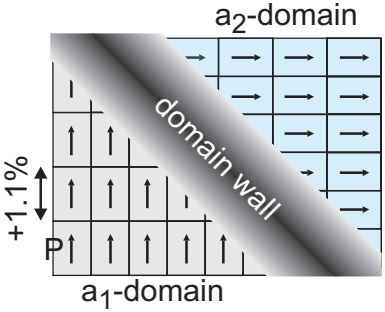

Figure 3.4.: Schematic picture of the domain wall between a_1 and a_2 domains. The lattice elongation in each domain amounts to about +1.1%. The polarization directions in neighboring domains enclose an angle of 90° between each other and 45° with the domain boundaries.

3.1.3. Application of an electric field

In order to influence the ferroelectric domain structure an electric field can be applied across the thickness of the $BaTiO_3$ substrate. For large enough fields the a_1 and a_2 pattern in the ferroelectric substrate then switches to a uniform c-domain. The polarization vector is pointing out-of-plane. It is important that the field can be applied also during AESWS measurement (cp. section 5.1). In Figure 3.5 we show a sketch of the board used for the application. On a copper square with the size of the sample the substrate side of the sample is mounted with double-sided conductive tape. The side of the ferromagnetic film is bonded to another copper contact. The two copper contacts can be connected with cables. As we want to perform AESWS measurements in flip chip geometry the sample has to be mounted

face down on the conducting CPW which is connected to the VNA. The application of large DC voltages (up to several hundreds of volts) to the sample could therefor endanger the sensitive ports of the VNA. We followed three points to secure the ports:

- The CPW is insulated with Al_2O_3 deposited by atomic layer deposition as well as a second layer of sputtered SiO_2.
- DC blocks are mounted in front of the two ports of the VNA.
- The side of the sample that is directly facing the CPW - the ferromagnetic side - is grounded, while the other side is set to a positive voltage.

Another aspect to be considered is that the ferroelectric substrate experiences structural changes during the application of an electric field. Therefor the electric field has to be applied very carefully during the experiment. The maximum sweep rate during application is set to 30 V/min. Then the lattice has enough time to relax preventing a cracking of the whole sample.

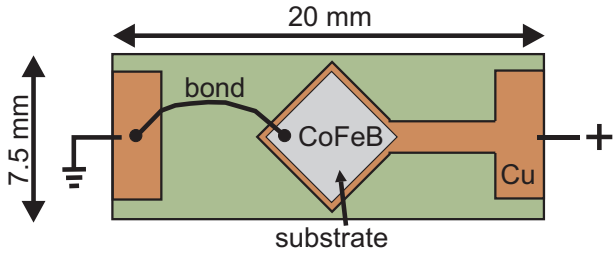

Figure 3.5.: Sketch of the board used to apply large electric voltages to the $BaTiO_3$ substrate. The sample is positioned on a conductive copper plate connected to positive voltage source. The ferromagnetic side of the sample is bonded to a grounded copper plate.

3.2. Permalloy ($Ni_{80}Fe_{20}$)

Permalloy is an alloy of the two magnetic elements nickel and iron. In literature permalloy is described as "an alloy of remarkable magnetic properties" [Arn23]. The material shows a large permeability which reaches a

maximum close to a nickel content of 80%. This large permeability led to the name permalloy. Furthermore the alloy provides small coercivity, near zero magnetostriction and a significant anisotropic magnetoresistance [Nah10]. The low magnetostriction makes permalloy an interesting material for industrial purposes where variable stresses would otherwise distort the magnetic properties too much. The alloy is often used as a spin injector in spin valve experiments as it shows reliable spin-polarized currents because of a high asymmetry in the itinerant d-electron spin density [Boc07, Vog09, Nah10]. In ferromagnetic resonance experiments the intrinsic damping parameter for a thin film is on the order of 0.005 [Pat75].

3.3. Cobalt iron boron ($\mathbf{Co_{40}Fe_{40}B_{20}}$)

Cobalt is known as the only element that increases the saturation magnetization and the Curie temperature if it is alloyed with iron [Jil98, Cul09]. This makes these alloys interesting for some applications. They exhibit a high permeability and low anisotropies. Additionally it was shown that CoFe alloys show large magnetostriction [Wil32]. CoFe alloys are usually given in a crystalline structure. If boron is added to a certain extent the resulting alloy is amorphous and can be sputtered. Soft magnetic properties can be improved by a low-temperature annealing. Furthermore, if a magnetic field is applied during annealing it is possible to induce an anisotropy. The dynamic magnetic properties of CoFeB are good as it shows low damping parameters between 0.01 and 0.001. Especially in the field of tunneling magnetoresistance (TMR) experiments CoFeB alloys gained a lot of interest as amorphous CoFeB guarantees smooth surfaces on an atomic scale [He10, Liu11]. It was found that the boron atoms that were initially substituted interstitially in the CoFe lattice are depleted during annealing and the layer forms a bcc lattice of CoFe [Rum10].

4. Preparation technique

In this chapter we show the preparation steps of the samples investigated in this thesis. First we will explain several preparation techniques we used and finally we give an insight on a complete fabrication procedure of a suspended ferromagnet with integrated platinum contacts.

4.1. Lithography

In order to produce micro- or nanostructures on a given substrate one has to apply certain techniques to define a mask and deposit material on the wafer in a controlled manner. One technique is called lithography whereof we introduce two types in the following.

4.1.1. Photo lithography

The CPWs described in section 5.1.2 and one freestanding ferromagnetic bridge layout (later in section 4.2.1) are fabricated via photo lithography. Typical preparation steps are the following:

- Create an optical mask using a laser writer
- Clean the piece of substrate with acetone using ultrasonic
- Rinse strongly with isopropanol and dry with nitrogen
- Coat the sample with LOR 5A photo resist using a spin coater at 4500 rpm for 60 seconds and bake the sample on a hot plate for one minute at $180\,^{\circ}\mathrm{C}$
- Coat the sample with S1813 photo resist using a spin coater at 6000 rpm for 60 seconds and bake the sample on a hot plate for one minute at $115\,^{\circ}\mathrm{C}$
- Bring sample and optical mask in close contact and expose with UV light of power density 12 mW/cm^2 for 3.5 - 4 seconds depending on the feature size

- Develop the exposed sample in MF26-A developer for 25 seconds, rinse with deionized water and dry with nitrogen
- Deposit the specific material in the evaporation chamber
- Do a lift-off process by putting the sample into 1165 remover, use ultrasonic if necessary, rinse with isopropanol and dry with nitrogen

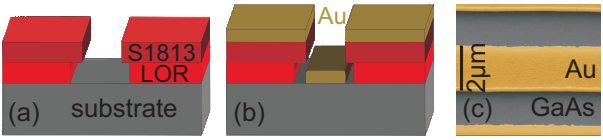

Figure 4.1.: Sketch of the double layer resist undercut structure before (a) and after (b) deposition of i.e. Au. Due to the undercut design tear-off edges are avoided. (c) Colored microscope picture of the 2 µm wide signal line of a coplanar waveguide prepared with a double layer resist.

This technique is a fast way to deposit material on the sample in a defined way and is used for structures with a minimum feature size of 2 µm. The position accuracy with the lithography device available for this thesis is estimated to be on the order of 5 µm.
As shown above the sample is coated with two different kinds of photo resist. Thereby the resist coated first is more sensitive to UV light than the top layer resist. Hence after exposure and development of the double layer resist an undercut geometry is created [Fig. 4.1 (a)]. The resulting advantage is that material that is deposited on the substrate in the predefined region has no direct contact to any resist layer [see Fig. 4.1 (b)]. This improves the edge roughness of the fabricated features as tear-off edges are avoided. Figure 4.1 (c) shows a colored scanning electron picture of the signal line of a 2 µm wide CPW.

4.1.2. Electron beam lithography

For electron beam lithography (e-lit) the individual steps read as follows:

- Draw a mask with the lithography software
- Clean the piece of substrate with acetone using ultrasonic

- Rinse strongly with isopropanol and dry with nitrogen
- Coat the sample with PMMA 50K resist using a spin coater at 4500 rpm for 60 seconds and bake the sample on a hot plate for five minutes at 160 °C
- Coat the sample with PMMA 950K resist using a spin coater at 4500 rpm for 60 seconds and bake the sample on a hot plate for five minutes at 160 °C
- Expose the sample with a dose of about 200 $\mu C/cm^2$ by moving the focused electron beam (acceleration voltage 20 kV) according to the mask designed before
- Develop the exposed sample in AR-600-56 developer for 65 seconds, rinse with isopropanol and dry with nitrogen
- Deposit the specific material in the evaporation chamber
- Do a lift-off process by putting the sample into 1165 remover, use ultrasonic if necessary, rinse with isopropanol and dry with nitrogen

Again the two-layer resist provokes an undercut structure and tear-off edges are avoided. Using this approach minimum feature sizes on the order of 100 nm can be realized.

4.2. Ferromagnetic freestanding bridges

One main goal of this thesis was to investigate ferromagnetic thin-film devices subject to temperature gradients in ferromagnets. In order to narrow these gradients to the in-plane direction of the film and to exclude possible contributions of the substrate itself the aim is a completely freestanding ferromagnetic stripe over a certain distance of several micrometer. Additionally in order to be able to measure the expected physical effects we integrate thin platinum contacts to this ferromagnetic bridge that are also freestanding over a certain distance. Due to the small thicknesses of the structures this is a very challenging preparation process and needs to be done very carefully. In the following we will describe two different ways how to realize such freestanding thin-film devices. We discuss advantages and disadvantages of the different processes.
First we discuss the basic challenges of this sample preparation:

- In order to get self-supporting structures we intend to fabricate the corresponding materials on a flat substrate and take away the supporting wafer in a final step. Using etchants to remove the substrate is one possibility. However most etchants that are suitable for wafers etch the ferromagnetic material as well. Because of this it has to be ensured that the bridge materials are not in touch with the etchant.

- Due to the large aspect ratio, i.e. the large freestanding length compared to the small thicknesses, any mechanical stress and electric discharge during the preparation process have to be avoided.

- The structure consists of a 40 - 65 nm thick ferromagnetic stripe with 15 nm thick Pt contacts which are crossing the FM perpendicularly. In order to increase the stability height variations in the crossing region have to be minimized.

4.2.1. Preparation based on GaAs

In this section we describe the optimized fabrication cycle to establish a freestanding bridge on a GaAs substrate. We will give an overview over the single steps as well as some explanations on the background of specific steps. In order to follow the necessary height-leveling and protection of the FM from the etchant we use aluminum in the following. This has the advantage, that it can be easily solved by the standard photo lithography developer MF-26A.

- Clean a piece of GaAs with acetone and isopropanol.

- Deposit 21 nm Al on the whole sample.

- Define the Pt contact structure consisting of four 5 µm wide stripes by photo lithography (described above) on top of the Al layer, but use only a single layer S1813 and develop 75 seconds to solve the Al at the predefined areas. The single layer resist is used to avoid that the developer dissolves Al in a wider area than necessary (cp. undercut described above).

- Refill the etched area with 6 nm of Al and 15 nm of Pt [Fig. 4.2 (a)].

- Define the Py stripe by photo lithography (double layer resist), but develop only 13 seconds. This duration is long enough to just develop the resist completely but sufficiently short to not solve the Al below the Py area. Before deposition of 40 nm of Py the surface is cleaned in-situ via Ar milling for 25 seconds. During evaporation the sample is swiveled with the rotation axis perpendicular to the long axis of the permalloy stripe in order to cover small steps homogeneously, that could remain from the underlying layers.

- Define etch windows next to the Py stripe via photo lithography and develop 75 seconds to solve the Al in this area. This gives access for the etchant to the substrate.

- Put the sample in the etchant (42 ml H_2O, 18 g citric acid and 4 ml H_2O_2) for approx. 60 minutes. The exact etching time depends on the position of the etch windows and has to be checked optically during etching in solution. The sample is carefully taken out of the etchant, put into water and checked with a water droplet on top under the microscope. We take care that the sample doesn't dry. This prevents mechanical stresses due to surface tension that would very likely destroy the sensitive bridge. Etch until the bridge is completely freestanding [Fig. 4.2 (b)].

- Solve the resist by carefully putting the sample into acetone and afterwards in isopropanol.

- Take away the Al layer by solving in developer until the layer is obviously gone [typically 90 seconds].

- Put the sample into water then into isopropanol for some minutes. Let the sample dry at air.

In the end a freestanding Py/Pt hybrid structure remains [Fig. 4.2 (c) and (d)]. The advantage of this preparation technique is that all stripes are leveled and smooth. However the yield of this way of preparation is not very high. The main reason except mechanical stresses could conceivably be that during the embedding of Pt in Al a small gap remains between the two materials where later on the etchant can reach the FM. This assumption is supported by the fact that in many samples the thinner Pt stripe stayed undamaged but the Py stripe was broken at the edge to the Pt stripe.

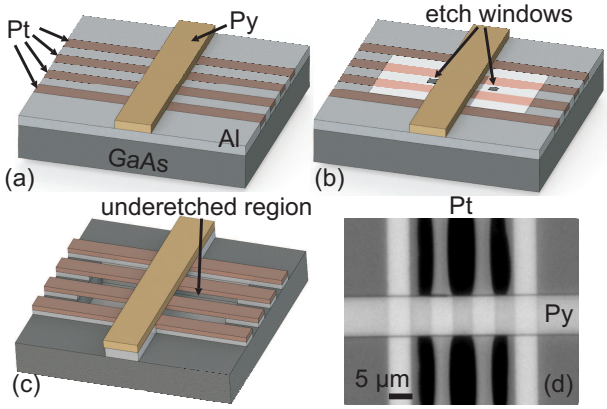

Figure 4.2.: Sketch of the preparation cycle for a freestanding ferromagnetic bridge based on GaAs. (a) In a first step the Pt stripes are embedded in an Al matrix. (b) A Py stripe is defined on top. Etch windows are put next to the Py stripe so that the etchant can access the substrate. The whole Al/Pt/Py hybrid structure is underetched. (c) Resist and Al are taken away, a freestanding ferromagnetic bridge with Pt contacts remains. (d) Photography of a freestanding bridge. The Py stripe is 10 µm wide.

4.2.2. Preparation based on silicon on insulator

In the last section we mentioned that although protected by Al the FM is probably attacked by the etchant. We therefor developed another technique where any wet etchants that could harm the FM are not needed. We use a silicon on insulator (SOI) wafer instead of GaAs. This wafer consists of bulk Si followed by a 3 µm thick SiO_2 layer which has on top a 220 nm thick Si layer. The main idea of this preparation process is to embed an Al layer in the top Si layer, prepare all the structures on top of this and solve the Al later on with the standard developer. The single steps plus explanation read as follows:

- Define a marker system on the SOI wafer via photo lithography and etch the markers through the Si top layer with reactive ion etching (RIE): reactive gases C_4F_8 and SF_6 for 80 seconds.

- Define a square of 20×20 µm^2 by e-lit and etch the top Si layer via

RIE. The buried SiO_2 layer acts as a etch stop layer as its etch rate is a factor of about 10 lower compared to the rate of Si. Atomic force microscopy (AFM) data show that the averaged surface roughness in the etched region amounts to 2 to 4 nm [Fig. 4.3 (a) and (b)].

- Refill the etched area with Al in order to get a planar surface that is as flat as possible. We therefor choose a very slow evaporation rate of 0.4 Å/s as this should decrease the grain size of the Al layer [Bor12]. AFM data show that a nominal Al layer thickness of 230 nm is needed to planarize the substrate again [Fig. 4.3 (c)]. However especially on the edges the Al surface is grainy and shows grain heights of mostly 20 to 60 nm and partly up to 100 nm [Fig. 4.3 (d)]. The highest topological features are located close to the edge of the Al region.

- Define four Pt stripes (5 µm wide, 23 µm long) via e-lit on top of the SOI-Al-plane. For height-leveling reasons the Al/SOI is etched via Ar milling before the deposition of Pt. The etch rate is determined to be 2.5 nm/min resulting in a total etching time of 6 minutes. Afterwards a 15 nm thick Pt layer is deposited.

- For stability reasons the previously defined Pt stripes are covered by 65 nm thick Pt contacts that reach almost to the Py stripe that is defined in the next step. This should increase the stability of the freestanding structures.

- Prepare a 65 nm thick, 10 µm wide Py stripe on top. The surface is cleaned with ion milling. Rotate the sample during evaporation between +45° and -45° with the rotation axis perpendicular to the Py stripe.

- Solve the underlying 230 nm thick Al layer with diluted developer MF-26A:H_2O 1:1 to decrease the dissolution rate and decrease possible stresses.

Using this technique the yield for freestanding devices has been increased. The leveling of the single layers is guaranteed. Still the roughness of the Al layer (especially in the edge region as described above) affects the topography of the hybrid structures on top. The electrical and magnetic properties of such devices will be discussed below. To improve the planarization one

might start from thinner Si top layers (e.g. 50 instead of 220 nm). Then the Al layer is expected to be smoother.

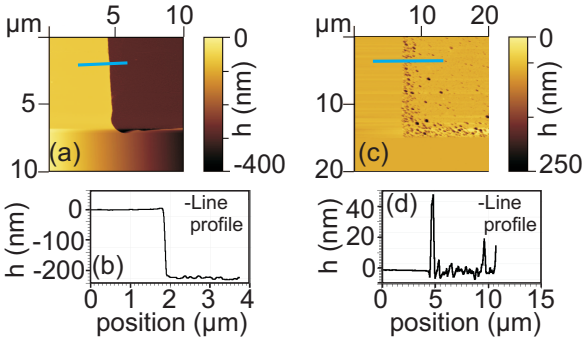

Figure 4.3.: Color-coded height profiles recorded by atomic force microscopy for the sample (a) after RIE and (c) after Al deposition. (b) and (d) show the corresponding height profiles taken at the position of the blue line in (a) and (c) respectively.

4.3. Magnetron sputtering

The samples investigated in chapter 7 are grown by magnetron sputtering [Kel00, Lah13]. In a vacuum chamber Ar gas is inserted and ionized in an electric field (Fig. 4.4). Ar is used as it is an inert gas. The Ar^+ plasma is concentrated in the region above the target by a magnetic field generated by permanent magnets placed below the target. Via an electric field the Ar^+-ions are accelerated and the target plate is bombarded with ions. Target atoms are ejected and condense - among others - at the substrate. A thin film is grown. The growth speed can thereby be controlled via the pressure of the Ar gas and the strength of the electric field applied. Typical pressure values are on the order of $10^{-3} - 10^{-4}$ mbar. The growth rate for the CoFeB films used in this thesis is about 0.12 nm/s. During the growth of the film the $BaTiO_3$ substrate is heated to a temperature of 300°C.

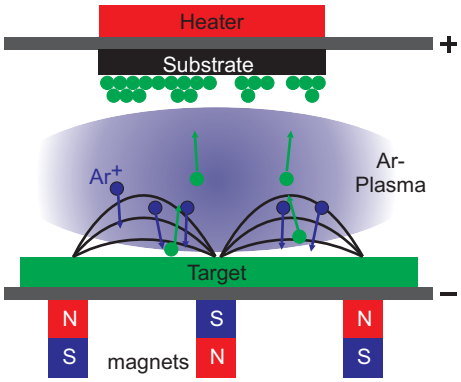

Figure 4.4.: Sketch of the magnetron sputtering chamber. Target atoms are knocked out by Ar^+ ions and deposited at the heated substrate. Permanent magnets confine the plasma.

5. Experimental techniques and methods

In this chapter, we give an overview on the experimental methods and techniques used throughout this thesis.

5.1. All Electrical Spin Wave Spectroscopy (AESWS)

5.1.1. Vector network analyzer setup

In order to perform investigations on ferromagnetic resonance we need a technique allowing a high-frequency excitation of the magnetic system. The AESWS setup therefor consists of the following parts [Fig. 5.1].

1. The heart piece of the setup is a vector network analyzer (VNA) from Agilent PNA N-5222A. It provides four ports, each with the possibility to emit and detect a microwave. The microwave is a continuous wave with a frequency between 10 MHz and 26.5 GHz. If e.g. port 1 emits a microwave all the other ports including port 1 itself can detect a microwave at the same frequency. A typical microwave power used here is 0 dBm (1 mW).

2. For the investigations an external magnetic field is needed. For the AESWS measurements we use two different magnetic field sources:
   - In-plane setup: Four coils mounted pairwise perpendicular to each other provide a magnetic field of up to $\mu_0 H = 100$ mT. A Kepco bipolar current source supplies the coils (maximum current 4 A). The bipolarity ensures that the field can be applied in opposite directions during the measurement without changing the wiring. Yokes are enhancing and guiding the magnetic field to the position of the sample.
   - Out-of-plane setup: Due to strong demagnetizing fields in thin films (cp. section 2.2) a larger field in the perpendicular direction is needed. We therefor use a superconducting field coil cooled with liquid helium and providing a field of up to

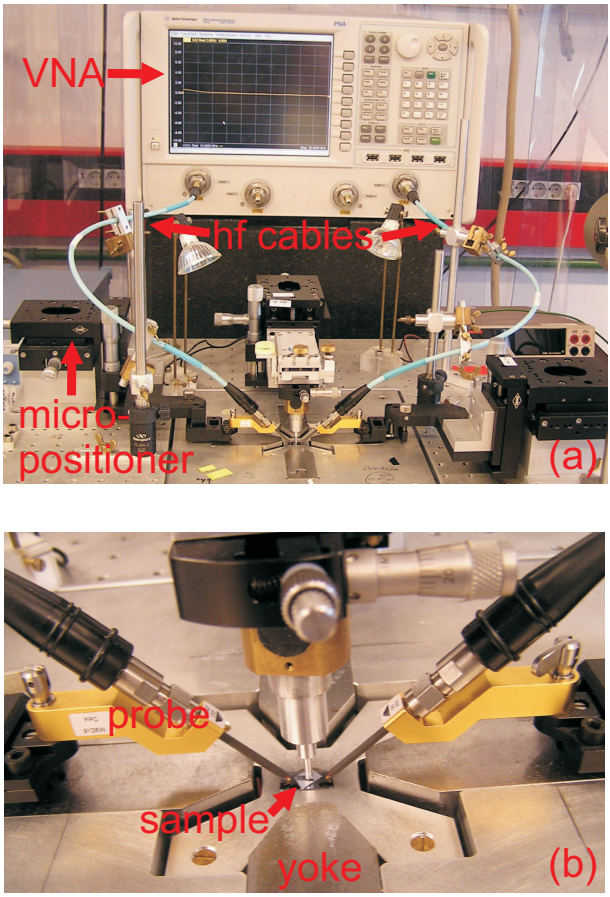

Figure 5.1.: Photograph of the setup that provides in-plane magnetic fields. (a) The sample is connected via microwave probes and hf cables to the VNA. The probes can be moved by micropositioners. (b) Zoom-in of the sample region. The sample is placed between four yokes in flip chip geometry.

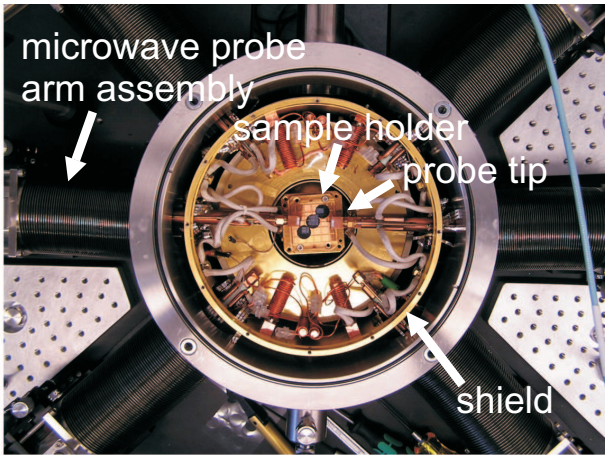

Figure 5.2.: Photograph of the setup that provides out-of-plane fields. It consists of six probe arms. The sample is placed in the center and contacted with probe tips. Temperature shields are necessary to reach low temperatures down to 4.2 K.

$\mu_0 H = 2.5$ T in both directions (Fig. 5.2). Additionally this setup provides the possibility to set the sample temperature between 4.2 K and 400 K.

3. In both magnetic field setups the field is actively controlled. In the in-plane setup Hall sensors are positioned as close as possible to the specimen. They are part of a control-cycle that is adjusting the output of the current source in order to get a stable field.

4. The electrical contact to the device under test (DUT) is established via microwave cables and probes. The probes consist of three parallel tips where the outer two are the ground lines and the center one is the signal line. The connection is impedance-matched in order to avoid reflections of the microwave at the contacts. Mechanical motion has to be avoided as the probe is attached. The setups are therefor mounted on a vibration cushioned table.

5. The AESWS setup is fully controlled by a computer program. The magnetic field is set to a desired value and the data acquisition is performed fully automated.

5.1.2. Coplanar waveguides

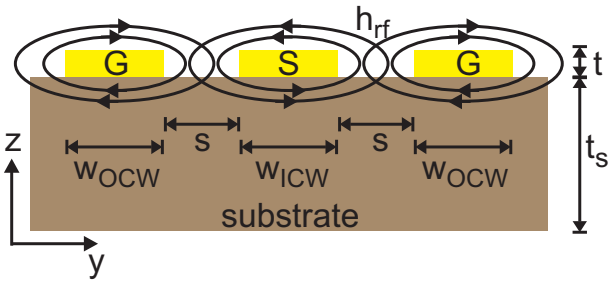

Figure 5.3.: Schematic cross section of a coplanar waveguide consisting of two ground lines (G) and a signal line (S) in the center. The excitation field h_{rf} surrounds the metallic lines. Relevant size parameters are given.

The microwave generated by the VNA has to be guided to the ferromagnetic sample. We therefor use a so-called coplanar waveguide (CPW). It consists of three conducting lines of thickness t placed parallel on a substrate with a thickness t_{s} and a dielectric constant ϵ_r (Fig. 5.3). The center line (width w_{ICW}) is the signal line whereas the outer two lines (width w_{OCW}) act as ground lines. The signal and ground lines are separated by air. The air gap is of width s. The microwave that is propagating through the CPW structure is traveling in areas of different dielectric constants. On the one side there is the substrate on the other side there is air. The wave is therefor no pure TEM mode, but can be approximated as quasi-TEM. When a microwave current flows through the conductors a high-frequency magnetic field is surrounding each line. The CPW has to be tailored in a way that the high-frequency impedance matches 50 Ω. This is essential as an impedance mismatch of microwave components leads to reflections at the corresponding junctions. Following Refs. [Wad91, Sim04] the impedance of a CPW can be calculated via:

$$Z_0 = \frac{30\pi}{\sqrt{\epsilon_{\mathrm{eff,t}}}} \frac{K(k_t')}{K(k_t)} \tag{5.1}$$

The relevant subequations are given as:

$$\epsilon_{\text{eff,t}} = \epsilon_{\text{eff}} - \frac{\epsilon_{\text{eff}} - 1}{\frac{(b-w_{\text{ICW}})/2}{0.7t}\frac{K(k)}{K'(k)} + 1} \tag{5.2}$$

$$\epsilon_{\text{eff}} = 1 + \frac{\epsilon_r - 1}{2}\frac{K(k')K(k_l)}{K(k)K(k_l')} \tag{5.3}$$

$$k_t = \frac{w_{\text{ICW},t}}{b_t}\,, \quad k = \frac{w_{\text{ICW}}}{b}\,, \quad k_t' = \sqrt{1-k_t^2}\,, \quad k' = \sqrt{1-k^2} \tag{5.4}$$

$$k_l = \frac{\sinh\left(\frac{\pi w_{ICW,t}}{4t_s}\right)}{\sinh\left(\frac{\pi b_t}{4t_s}\right)}\,, \quad k_l' = \sqrt{1-k_l^2} \tag{5.5}$$

$$w_{\text{ICW},t} = w_{\text{ICW}} + \frac{1.25t}{\pi}\left[1 + \ln\left(\frac{4\pi w_{\text{ICW}}}{t}\right)\right] \tag{5.6}$$

$$b_t = b - \frac{1.25t}{\pi}\left[1 + \ln\left(\frac{4\pi w_{\text{ICW}}}{t}\right)\right] \tag{5.7}$$

where some terms are corrected for the thickness t which is essential for good results. K and K' are the complete elliptic integrals of the first kind and its complement and $b = w_{\text{ICW}} + 2s$. We find, that the impedance can be adjusted mainly via the geometry of the CPW itself, i.e. the ratio of w_{ICW} and b. This means that keeping this ratio constant causes the impedance to stay approximately constant too. This fact is used to tailor the CPWs as the contact pads connected with microwave probes show a pitch of 250 µm. The parallel conducting lines show a smaller pitch making a tapering necessary.

5.1.3. Microwave excitation

The CPWs are used to excite the ferromagnetic system via a high frequency excitation field. This field has its origin in the microwave current generated from the VNA and sent via cables and probe tips to the CPW. The VNA used here is therefor emitting microwaves of frequencies between 10 MHz and 26.5 GHz. The VNA excites a sinusoidal voltage signal

$$V(x,t) = \widetilde{V}(x)\exp(\mathrm{j}\omega t). \tag{5.8}$$

In the following we will use the assumption of a transmission line comprising two conductors separated by a dielectric. We consider a short element of this line dx that is mainly characterized by the series resistance R and the series inductance L as well as the shunt conductance G and the shunt capacitance C [Bil07a]. This is however only practicable in the approximation of TEM waves. Furthermore we presume that dx is much smaller than the wavelength of the microwave. The change in voltage V and current I in both lines can be written for a infinitely small dx as:

$$\frac{\partial V}{\partial x} = -(RI + L\frac{\partial I}{\partial t}) \tag{5.9}$$

$$\frac{\partial I}{\partial x} = -(GV + C\frac{\partial V}{\partial t}) \tag{5.10}$$

One can show that we get the telegrapher's equations [Sar43]

$$\frac{\partial^2 \widetilde{V}}{\partial x^2} = \gamma^2 \widetilde{V} \quad and \quad \frac{\partial^2 \widetilde{I}}{\partial x^2} = \gamma^2 \widetilde{I}, \tag{5.11}$$

where γ is the propagation constant defined as

$$\gamma = \sqrt{(R + \mathrm{j}\omega L)(G + \mathrm{j}\omega C)}. \tag{5.12}$$

Equations 5.11 can be solved with a linear combination of waves traveling forward and backward [Bil07a]

$$\widetilde{V}(x) = \widetilde{V}^{+}\exp(-\gamma x) + \widetilde{V}^{-}\exp(\gamma x) \tag{5.13}$$

$$\widetilde{I}(x) = \widetilde{I}^{+}\exp(-\gamma x) + \widetilde{I}^{-}\exp(\gamma x), \tag{5.14}$$

where $\widetilde{V}^{+}$, $\widetilde{I}^{+}$, $\widetilde{V}^{-}$, $\widetilde{I}^{-}$ are integration constants. Finally, we can define the characteristic impedance Z_c of the transmission line to be

$$Z_c = \frac{\widetilde{V}^{+}}{\widetilde{I}^{+}} = -\frac{\widetilde{V}^{-}}{\widetilde{I}^{-}}. \tag{5.15}$$

The CPW is used to excite the ferromagnetic material. For data analysis

the knowledge of the wave vector excitation spectrum of a specific CPW is key. While finite element simulations can be used to simulate the spatial excitation we can use an approximation to determine the excitation spectrum [Cou04a, Ken07, Neu11a]. The high frequency field surrounding the CPW is sketched in Fig. 5.3. The component of h_{rf} that is relevant for the excitation of the ferromagnet is $h_{\text{rf},y}$. $h_{\text{rf},x}$ is small as the CPW is considered to be very long and $h_{\text{rf},z}$ can be shown to be much smaller than $h_{\text{rf},y}$ as the CPW is very thin [Neu11a]. As the direction of the current in the ground lines is opposite to the signal line $h_{\text{rf},y}$ varies strongly as a function of y. Furthermore the field value underneath the ground lines is assumed to be half the field value underneath the signal line. We can now perform a Fourier transformation of the spatial current distribution in the CPW and get the excitation spectrum in the k space. In Fig. 5.4 we plot the excitation amplitude as a function of the wave vector for a CPW with $w_{\text{ICW}} = 20$ µm and $s = 11$ µm. The spectrum shows several maxima. For the measurements in this thesis the most relevant wave vector is the first maximum located at $k_{\text{CPW}} = 0.097 \cdot 10^4$ rad/cm. We find a finite wave vector distribution around k_{CPW}. This distribution Δk enters also the frequency linewidth described in section 2.3.2. There are two approximations for the maximum wave vector k_{max} of the first excitation peak. The first one is given in Ref. [Cou04a] by $k_{\text{max}} \approx \pi / w_{\text{ICW}} \approx 0.16 \cdot 10^4$ rad/cm. The second one is given in Ref. [Ken07] as $k_{\text{max}} \approx 2\pi/(w_{\text{ICW}} + 2s) \approx 0.15 \cdot 10^4$ rad/cm. These values are both lower than $k_{\text{max}} = 0.20 \cdot 10^4$ rad/cm extracted from Fig. 5.4.
In Ref. [Sch13b] finite element simulations were performed for a nominally identical CPW like used in this thesis. The value of k_{CPW} was determined to be $0.096 \cdot 10^4$ rad/cm and is very close to the value determined above. However, for the data analysis we will use the value from Ref. [Sch13b] as it is supposed to be more accurate as it considers the finite skin depth.

5.1.4. Scattering parameters

In the case of non-TEM modes the voltage and current at high frequencies are hard to detect. Instead, we use so-called scattering parameters, or S-parameters, to give a relation between the incident and reflected waves. The VNA used in this study directly measures the S-parameters. The scattering matrix for a device with n ports is defined as [Bil07a]

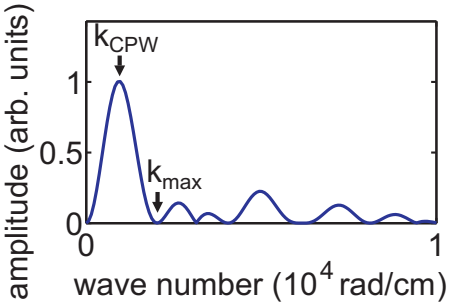

Figure 5.4.: Excitation spectrum of a CPW with $w_{\mathrm{ICW}} = 20$ µm and $s = 11$ µm determined by the Fourier transformation of the assumed spatial current distribution. The amplitude is normalized on the maximum value.

$$a_n = \frac{V_n + Z_{cn} I_n}{2\sqrt{Z_{cn}}} \quad , \quad b_n = \frac{V_n - Z_{cn} I_n}{2\sqrt{Z_{cn}}}. \tag{5.16}$$

Here, a_n and b_n are the complex normalized wave amplitudes and

$$V_n = \sqrt{Z_{cn}}(a_n + b_n) \quad , \quad I_n = \frac{a_n - b_n}{\sqrt{Z_{cn}}}. \tag{5.17}$$

Entering equations 5.13 and 5.14 into equation 5.16 one gets

$$a_n = \frac{V_n^+}{Z_{cn}} \exp(-\gamma x) \quad , \quad b_n = \frac{V_n^-}{Z_{cn}} \exp(\gamma x). \tag{5.18}$$

We see that the a_n parameter describes the incident wave, whereas the b_n parameter is related to the emitted wave. If we now restrict to the case of two ports, the parameters $a_{1,2}$ and $b_{1,2}$ are linked via four S-parameters as follows:

$$\begin{pmatrix} b_1 \\ b_2 \end{pmatrix} = \begin{pmatrix} S_{11} & S_{12} \\ S_{21} & S_{22} \end{pmatrix} \begin{pmatrix} a_1 \\ a_2 \end{pmatrix} \tag{5.19}$$

In Figure 5.5 the definition of the four S-parameters is sketched by reference to the device under test. S_{11} and S_{22} describe the signal reflected from the DUT with the wave originating from port 1 or port 2 respectively. Consequently S_{21} and S_{12} are the signals transmitted through the DUT

from one port to the other.

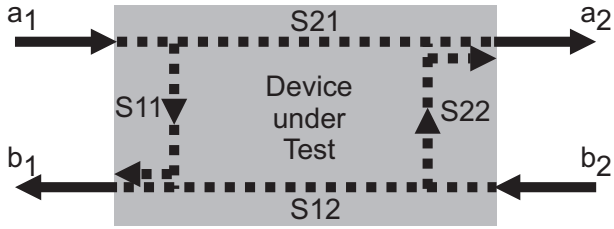

Figure 5.5.: Definition of the four S-parameters. S_{11} and S_{22} mark the reflected signals at port 1 and 2. S_{21} and S_{12} correspond to the transmitted signals through the DUT.

5.1.5. Two-port measurement in flip chip geometry

Let us now consider a ferromagnetic sample that is placed face down on a substrate including a CPW. The ferromagnetic metallic film is mounted close to the CPW. An insulating layer is therefor not needed as the air gap caused by unevenness of the two surfaces is enough to prevent a short of the CPW's signal and ground lines. For simplicity we consider only a short piece of ferromagnet (length dx) that is solely covering the inner conductor of the CPW. We have already shown in section 5.1.2 that the microwave traveling through the conductor lines generates a high frequency magnetic field surrounding the lines. For a CPW with $w_{\mathrm{ICW}} \gg t$ we can state that the field is parallel to the CPW plane close above the center of the signal conductor, i.e. it has only a y-component. First of all we want to estimate the strength of the hf-field surrounding the CPW for a typical VNA microwave power used in this thesis of 0 dBm = 1 mW. For an impedance of $Z_c = 50\ \Omega$ the microwave current i is then given as $i \approx 4.5$ mA. According to Refs. [Cou04b, Bil07a] the field amplitude generated by the CPW can be estimated by $h = i/2w_{\mathrm{ICW}}$. For the CPW used mostly throughout this thesis $w_{\mathrm{ICW}} = 20$ µm. This leads to a field of $\mu_0 h = 141$ µT. Compared to the external field of up to 100 mT this field is orders of magnitude smaller allowing a linear approximation as the magnetization's displacement angles are small [Cou04a]. In fact, the field h is expected to be even smaller, as losses in the cables and contacts are neglected here.
Following Refs. [Cou04b, Cou04a, Pai99] the susceptibility is given as

$$\chi(\omega) = \Delta Z 2 w_{\mathrm{ICW}} / (i\omega \mu_0 d_{\mathrm{m}} L), \tag{5.20}$$

with ΔZ the change in line impedance Z at a frequency ω due to the magnetic material of thickness d_{m}. L is the length of the waveguide. We want to remind the reader that the impedance directly enters the scattering parameters. For the reflection the scattering parameter, i.e. S_{11}, can be written as

$$S_{11} = \frac{\Delta Z}{\Delta Z + 2Z_c}. \tag{5.21}$$

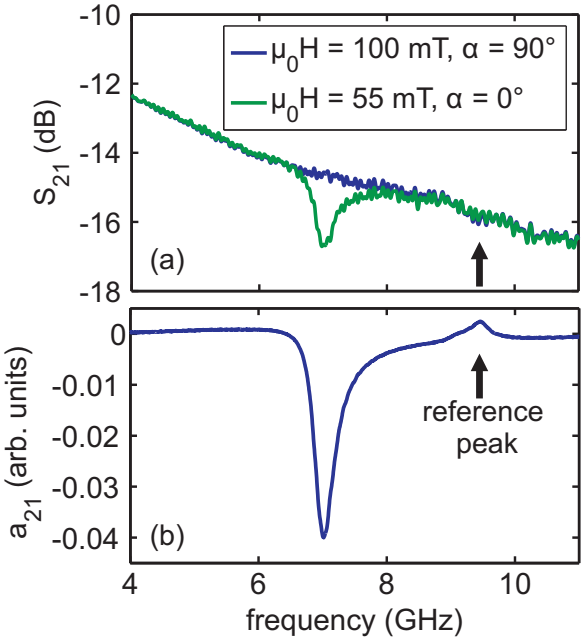

Figure 5.6.: (a) S_{21} for a 47 nm thick CoFeB film for both a field of 55 mT applied along the long axis of the CPW, $\alpha = 0°$, and a field of 100 mT applied perpendicular as a reference. For $\alpha = 90°$ the signal strength is small. (b) Subtracted data, a_{21}, for the data of (a). The signal-to-noise ratio is increased, the small peak from the reference spectrum can be observed.

Next, we discuss spectra taken by the VNA in a typical measurement. We therefor show data taken with a 9 mm long CPW, $w_{\mathrm{ICW}} = 20$ µm, while a 47 nm thick $Co_{40}Fe_{40}B_{20}$ film attached to a $SrTiO_3$ substrate is mounted with the film side down on the CPW. In Figure 5.6 (a) we show S_{21} in decibel (dB) for both the in-plane external field applied along the long axis of the CPW, i.e. $\alpha = 0^\circ$ at $\mu_0 H = 55$ mT, and applied perpendicular with a strength of 100 mT, i.e. $\alpha = 90^\circ$. In general the S-parameters in dB are given as

$$S_{ij}[\mathrm{dB}] = 20 \log \left(\frac{b_i}{a_j} \right), \tag{5.22}$$

with $i, j = 1, 2, ..., n$ for a VNA with n ports (here $n = 2$). We find, that for most frequencies S_{21} is on the same order for both angles. Solely around 7 GHz the two spectra clearly deviate from each other. In order to increase the signal-to-noise ratio we use a difference method and subtract every spectrum from a reference spectrum. In most cases it is most feasible to use a spectrum taken at $\alpha = 90^\circ$ as a reference. The reason for this is the following: Imagine a film with no in-plane anisotropy on top of a CPW. The magnetization follows the external field and we measure the S_{21} parameter. If we now apply the external field perpendicular to the long axis of the CPW the magnetization **M** becomes parallel to the in-plane component of the excitation field h_{rf} generated by the CPW (cp. section 5.1.2). The torque acting on the magnetization is therefor minimum and the signal strength is small. The magnetic independent parts of S_{21} behave the same for $\alpha = 0^\circ$ and $\alpha = 90^\circ$ and their influence to the measurement signal can be reduced by subtraction. In Figure 5.6 (b) we plot the subtracted data taken from Figure 5.6 (a). The subtraction is calculated as

$$a_{21} = 10^{S_{21,\alpha=0^\circ}/20} - 10^{S_{21,\alpha=90^\circ}/20}. \tag{5.23}$$

We see, that the signal-to-noise ratio is increased. The spectrum is smoother as errors that occur in both spectra are eliminated. What remains is a peak around 7 GHz marking the resonance frequency of the ferromagnetic field at 55 mT. At about 9.5 GHz a second small peak is visible showing opposite sign if compared to the peak at 7 GHz. This can be attributed to the resonance frequency in the reference spectrum, i.e. the resonance frequency for $\alpha = 90^\circ$ and 100 mT. The peak is small for the above stated reasons.

As mentioned before in section 2.3.1 the detected signal consists of an imaginary part $\Im(a_{21})$ and a real part $\Re(a_{21})$. In Figure 5.7 we show the real and imaginary part of a_{21} as well as the absolute magnitude $|a_{21}|$ for the 47 nm thick CoFeB film at $\alpha = 0°$ and $\mu_0 H = 5$ mT. The real part shows two extrema symmetric around the resonance frequency, the imaginary part is of Lorentzian shape with the maximum at the resonance. The magnitude can be calculated via $|a_{21}| = \sqrt{\Re^2(a_{21}) + \Im^2(a_{21})}$. The ferromagnetic resonance linewidth Δf can be extracted from the full width at half maximum (FWHM) of the imaginary part or from the FWHM of the magnitude scaled by a factor of $1/\sqrt{3}$ [Sta09, Sch13b].

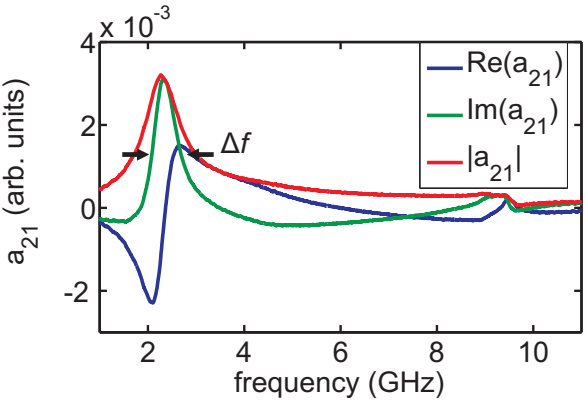

Figure 5.7.: Real and imaginary part of a_{21} for a 47 nm thick CoFeB film at a field of 5 mT and $\alpha = 0°$. The imaginary part of the resonance at about 2 GHz follows closely a Lorentzian shape. The linewidth Δf is defined as FWHM of the imaginary part. The magnitude $|a_{21}|$ is plotted.

5.2. Laser-based heating setup

For the investigations on heat gradients in ferromagnetic structures shown later in chapter 6 a new measurement setup had to be designed in the course of this thesis (Fig. 5.8). For the generation of local temperature gradients we developed a heating setup allowing us to focus a laser spot on the sample. We thereby followed an approach introduced by Gravier et al. [Gra06]

and applied by further groups [MÏ0, Bie13, Wei12]. In Figure 5.8 we show a general overview on the setup. It consists of a laser that is mounted in front of a beam splitter, transmitted through two further beam splitters and focused by a moveable objective on the sample. During the time of this thesis the setup was constantly improved and adjusted. We can mainly divide the states of the setup into two cases that we call setup 1 and setup 2:

- **Setup 1:**
  Here the laser is a Lasertack diode pumped solid state (DPSS) laser of a wavelength of 532 nm and a maximum power of 912 mW. The three beam splitters 1-3 are 50:50 beam splitters. The ratio is a measure for the amount of light that is deflected in the perpendicular direction compared to the amount of light that can pass the beam splitter straight.

- **Setup 2:**
  The laser is replaced by a Toptica iBeam smart diode laser at 407 nm wavelength. The maximum power is 300 mW. Compared to the laser of setup 1 this laser offers better controllability and a better beam profile. Additionally the 3 beam splitters are replaced. Splitter 1 is a 90:10 splitter, meaning 90 % of the light is reflected to the perpendicular direction and splitter 2 and 3 are 10:90. We therefor increased the ratio of light power that is reaching the sample to light power emitted by the laser.

We will mention in chapter 6 which setup is currently used. Both setups have the remaining parts in common. The objective (100x Mitutoyo Plan APO SL) that focuses the laser light on the sample is moveable in z-direction to adjust the focus point. We use an objective positioner MIPOS 500 from piezosystem jena. The laser light is collimated when it comes from the laser. If the objective has the correct distance to the sample the light is focused and partly reflected from the sample. Light that is backreflected at the focus point is parallel after the objective again. It is redirected at beam splitter 2 and focused by a lens on a pinhole that is mounted in the focus point of the lens. If the incoming laser light is collimated, the amount of light coming through the pinhole is at maximum. If the light is not parallel - because the sample is not in the focus of the objective - the intensity through the pinhole is smaller. Behind the pinhole a

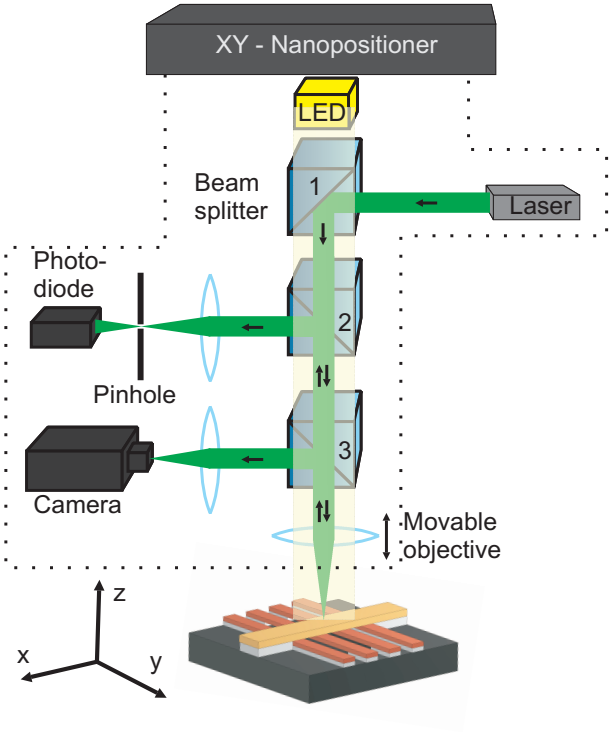

Figure 5.8.: Sketch of the laser-based heating setup. The laser light is redirected by a beam splitter and focused by a movable objective on the sample. An LED illuminates the beam path. The reflected light is transmitted to a camera and a combination of a pinhole and a photodiode. The whole optics is mounted under a XY-nanopositioning system.

photodiode is mounted. The signal of the photodiode is therefor a measure for the focus point that is thereby automatically adjusted.
Additionally, the light reflected from the sample is redirected at beam splitter 3 and focused on the chip of a CCD camera. In order to get a picture of the sample the whole beam path is illuminated by a LED positioned on top of beam splitter 1. All the optical components are assembled via a cage system from Thorlabs (cp. Fig. 5.9). The whole optics is mounted under a two-axis nanopositioning system (Aerotech ANT130-060-XY-PLUS, Fig. 5.9). Not only the focus is adjusted automatically but also the x and y position of the laser spot is controlled. We therefor use a commercially available positioning software (TFPDAS4-MICRO). For the active position control one detail on the sample surface is marked such as a marker or equivalent structure. The software uses the picture of this detail as a reference and compares all the following pictures that are taken by the CCD with the reference one. If there is a drift, the software operates the nanopositioner and moves back to the desired position. Thermal drifts can be eliminated. Additionally, we can define an array of points that should be scanned with the laser spot. The deviation from the original reference position is calculated and a raster scan is performed. In general the positioning accuracy can be estimated to a few tens of nanometer.
A magnetic field is available up to 100 mT rotatable in the plane of the sample and is designed equivalent to the in-plane setup for AESWS. The sample is mounted to a chip carrier and contacted with bonds between the sample and the chip carrier. Wires connect the chip carrier with the electronics. The whole setup is mounted in a box of aluminum for two reasons. First, this acts as a shield for disturbances from the outside and second it grants safety for the work with the lasers. In order to reduce further disturbances the setup is mounted on a vibration cushioned table.
We note that the positioning accuracy would be better if the sample was moved and not the whole optics. However, we designed the setup in a way, that AESWS measurements can be combined with laser heating. Therefor microwave probe tips can be connected and the sample may not be moved.

5.2.1. Determination of the laser spot size

The laser mounted in the setup is focused on the sample surface. The size of the laser spot can be determined by a so-called knife edge experiment [Dur]. Let us assume a laser beam with a Gaussian intensity profile that

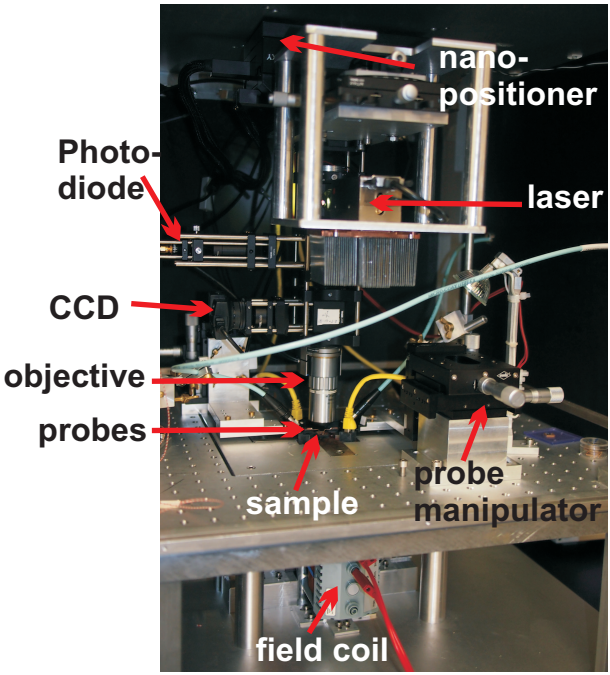

Figure 5.9.: Photograph of the laser-based heating setup. The laser, the objective, the CCD camera and the nanopositioning system can be seen. Additionally, microwave probes can be integrated and positioned by a probe manipulator. Field coils underneath the sample provide in-plane fields of up to 100 mT.

propagates in the z-direction:

$$I(x,y) = I_0 e^{-2x^2/w_x^2} e^{-2y^2/w_y^2}. \tag{5.24}$$

Here, w_x and w_y correspond to radii where the intensity amounts to $1/e^2$ of the peak intensity I_0 in the two directions. We move the laser spot across a sharp edge that separates two regions of strongly deviating reflectivity. The laser spot thereby moves in the x-direction. The position-dependent power $P(U)$ of the reflected beam is given as

$$P(U) = P_{tot} - I_0 \int_{-\infty}^{U} e^{-2x^2/w_x^2} dx \int_{-\infty}^{\infty} e^{-2y^2/w_y^2} dy, \tag{5.25}$$

where P_{tot} is the total power of the beam. It follows:

$$P(U) = \frac{P_{tot}}{2} - \sqrt{\frac{\pi}{2}} I_0 w_y \int_{0}^{U} e^{-2x^2/w_x^2} dx. \tag{5.26}$$

Introducing the error function it can be shown that [Dur]

$$P(U) = \frac{P_{tot}}{2} \left[1 - \text{erf}\left(\frac{\sqrt{2}U}{w_x} \right) \right]. \tag{5.27}$$

In Figure 5.10 we plot the signal of the photodiode that is proportional to the reflected laser power while the spot is moved across a sharp edge. The edge was created by reactive ion etching. The signal is normalized to the maximum value. We find a large signal almost constant from 0 µm to about 4 µm. From 4 µm on the signal drops to about 35% of the maximum value and stays almost constant again. The laser spot is swept from a flat Si surface (grey region in Fig. 5.10) to the SiO_2 area (green region) lying 220 nm below and showing transparency in the visible wavelength regime. The reflected intensity is therefor considered to be significantly smaller in the SiO_2 region. The laser spot size is determined by two definitions and for both setup 1 and setup 2 (cp. section 5.2). The first definition is a $10\% - 90\%$ criterion where the spot size is given by the two positions where the intensity is at 10% or 90% between the maximum and minimum value. For laser setup 1 we determine a spot size of 1.1 µm. Laser setup 2 shows an improved spot size of about 0.5 µm.
A second definition of the spot size is to fit equation 5.27 to the position-dependent data. For laser setup 2 we find $w_x \approx 0.4$ µm. The signal is not that constant when the laser spot is placed completely in the SiO_2 region if compared to the Si region. The reason for this might be the rough surface of the SiO_2 and reflections at the surfaces.

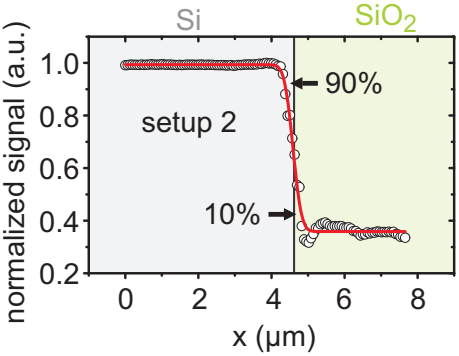

Figure 5.10.: Data taken in a knife edge experiment (circles). The left part (grey) marks the Si substrate that lies in the focus plane of the laser, the right part (green) is the SiO_2 that lies topologically deeper. The $10\% - 90\%$-criterion is sketched. The red line is a fit of equation 5.27 to the data.

5.2.2. Lock-in technique

The signals investigated with the laser heating setup are usually small, meaning on the nanovolt scale. DC measurements based on a conventional voltmeter provide a non-satisfactory signal to noise ratio. Instead we make use of the lock-in technique. In the following we give a brief description of this method following Ref. [Sys]. In order to distinguish small signals from the noise pure amplification is not enough. Assume an AC signal at 10 kHz and an amplitude of 10 nV. A low-noise amplifier with an input noise of 5 nV/$\sqrt{\text{Hz}}$, a bandwidth of 100 kHz and a gain of 1000 will lead to a signal of 10 µV and a noise level of 5 nV/$\sqrt{\text{Hz}}\cdot\sqrt{100\text{ kHz}}\cdot 1000 = 1.6$ mV. The signal-to-noise ratio makes a detection of the signal impossible. A lock-in uses therefor a phase-sensitive detector (PSD). This detector works at a frequency of 10 kHz with a bandwidth of 0.01 Hz. The signal level is the same as above but the noise level is now reduced to 0.5 µV. A signal-to-noise ratio of 20 allows for a detailed signal analysis.

For the PSD a reference frequency is needed. This may come from a function generator that drives the experiment and is linked with the lock-in amplifier, i.e. the experiment is excited with a sine wave at a certain frequency ω_r. The function generator sends e.g. a square wave at the same

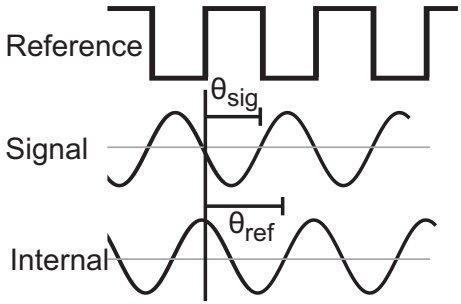

Figure 5.11.: Sketch of the external reference signal that excites the system (top). The signal detected by the input of the amplifier has a certain phase shift θ_{sig} (center). An internal reference is generated by the amplifier with θ_{ref} (bottom). Figure adapted from Ref. [Sys].

frequency via the sync output to the lock-in amplifier (Figure 5.11 top). The signal $V_{\text{sig}} \sin(\omega_r t + \theta_{\text{sig}})$ coming from the experiment to the lock-in follows the excitation and is of sine shape (Figure 5.11 center). V_{sig} is the amplitude and θ_{sig} is the phase. The lock-in generates an internal reference $V_L \sin(\omega_L t + \theta_{\text{ref}})$ locked to the external reference (Figure 5.11 bottom). The signal is amplified and multiplied with the lock-in reference by the PSD. The PSD output is

$$\begin{aligned} V_{\text{psd}} &= V_{\text{sig}} V_{\text{L}} \sin(\omega_r t + \theta_{\text{sig}}) \sin(\omega_L t + \theta_{\text{ref}} && (5.28)\\ &= \tfrac{1}{2} V_{\text{sig}} V_{\text{L}} \cos[(\omega_r - \omega_L)t + \theta_{\text{sig}} - \theta_{\text{ref}}] && (5.29)\\ &\quad -\tfrac{1}{2} V_{\text{sig}} V_{\text{L}} \cos[(\omega_r + \omega_L)t + \theta_{\text{sig}} + \theta_{\text{ref}}] && (5.30) \end{aligned}$$

This output corresponds to two AC signals at the difference frequency $(\omega_r - \omega_L)$ and at the sum frequency $(\omega_r + \omega_L)$. With a low pass filter the AC part is removed. If $\omega_r = \omega_L$ a DC signal that is proportional to the signal amplitude remains from the difference frequency part.

$$V_{\text{psd}} = \frac{1}{2} V_{\text{sig}} V_{\text{L}} \cos(\theta_{\text{sig}} - \theta_{\text{ref}}) \tag{5.31}$$

For $\theta = \theta_{\text{sig}} - \theta_{\text{ref}} = 0$ the signal amplitude V_{sig} can be measured. For $\theta = 90°$ the output is zero. By adding a second PSD that multiplies the

signal with a reference signal shifted by $90°$ the phase dependency can be eliminated. This is called a dual-phase lock-in. The two outputs of the two PSD can then be written as

$$X = V_{\text{sig}} \cos\theta \,, \quad \text{and} \quad Y = V_{\text{sig}} \sin\theta. \tag{5.32}$$

These can be understood as the signal given as a vector. The magnitude R does not depend on the phase and is given as

$$R = \sqrt{X^2 + Y^2} = V_{\text{sig}}. \tag{5.33}$$

The phase reads as

$$\theta = \arctan(Y/X). \tag{5.34}$$

Many lock-in amplifiers provide the possibility to use an internal reference generator, that can be used for the excitation of the device under test instead of an external function generator.

5.3. Magneto-optic Kerr effect

In this thesis we will show data of Magneto-optic Kerr microscopy. These measurements were performed in the group of Prof. Dr. Sebastiaan van Dijken at the Aalto University School of Science, Finland. We will therefor give a short introduction on the underlying effect. For a detailed consideration the reader is refered to Ref. [Hub98]. The magneto-optic Kerr effect (MOKE) [Ker77, Ker78] describes changes in polarized light reflected from a magnetized surface. These changes can be the rotation of the polarization, an introduction of ellipticity or the change in intensity [Oak05]. There are mainly three geometries (cp. Figure 7.3):

- **transverse:** The magnetization points perpendicular to the plane of the incident and reflected light and lies in the plane of the sample.
- **logitudinal:** The magnetization is collinear with the plane of the incident and reflected light and lies in the plane of the sample.
- **polar:** Here, the magnetization points out of the sample plane.

In general a MOKE setup contains a polarizer and an analyzer. Laser light is sent through the polarizer and polarized in a specific way (linear, circular, elliptical). The reflected light is sent through an analyzer (a second polarizer) and the light intensity is measured behind it. If the analyzer is orientated in the same direction as the polarizer and the light experiences no change on its way the intensity after the polarizer is maximum. If their polarization axes enclose an angle of 90° with each other the light intensity would be zero. However, if the light is reflected from a magnetic surface the anisotropic dielectric permittivity ϵ causes a change to the light depending on the magnetization direction. The change in polarization and with this in light intensity after the analyzer is a measure for the magnetization direction. In combination with an optical microscope the MOKE effect can be used to image magnetic domains with a spatial resolution on the order of a μm and better.

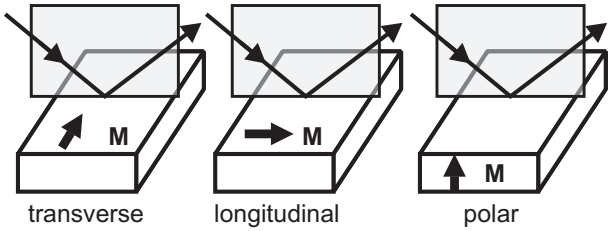

Figure 5.12.: Sketch of three MOKE geometries depending on the magnetization direction. The incident plane of light is sketched by a grey rectangle.

6. Laser induced thermal gradients in freestanding ferromagnets

In this chapter we investigate the influence of temperature gradients on a ferromagnetic material. We therefor start to characterize the ferromagnetic material by the anisotropic magnetoresistance and will afterwards discuss laser-heating induced effects.

Samples investigated in this chapter

Each sample investigated here was prepared like explained in chapter 4 and consists of a Py stripe that is crossed by four platinum stripes (cp. Fig. 4.2). The following table gives an overview of the samples investigated in this chapter and their properties:

sample name	substrate	suspended	w_{Pt} [μm]	w_{Py} [μm]	t_{Pt} [nm]	t_{Py} [nm]
SC028	GaAs	no	5	10	15	40
SC030	GaAs	yes	5	10	15	40
SCSOI_42tr	SOI	no	5	10	15	65
SCSOI_42br	SOI	yes	5	10	15	65

Table 6.1.: Definition of sample names and basic properties of each sample. w and t stand for the width and the thickness of the single materials, respectively.

6.1. Anisotropic magnetoresistance

To explore the magnetic properties of suspended bridges we performed AMR experiments. In Fig. 6.1 (a) we plot the field-dependent resistance of sample SC030 measured between the outer two Pt stripes [cp. contacts 1 and 4 in Fig. 6.2 (a)] by applying an ac current of 100 nA at a frequency of about 1 kHz along the Py stripe. The voltage is detected with a lock-in

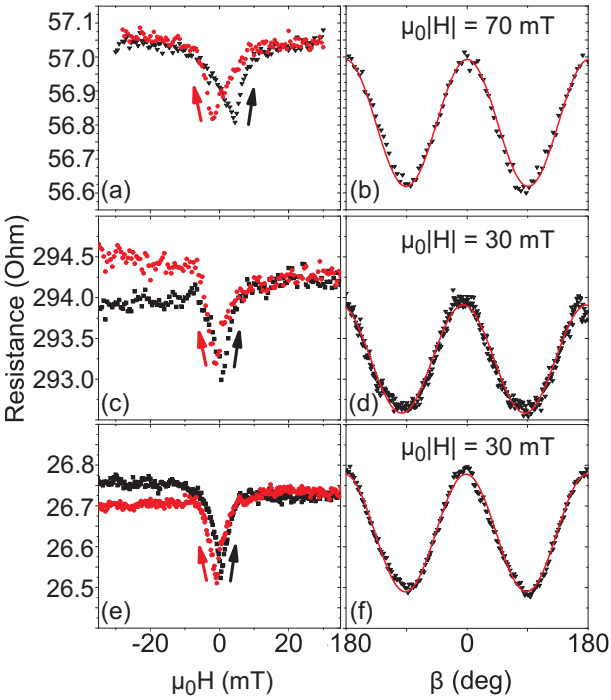

Figure 6.1.: Field-dependent (left row) and angle-dependent (right row) resistance variations. In the left row black (red) arrows mark the up (down) sweep. The field is applied along the Py stripe ($\beta = 0°$). In the right row the red lines represent sine fits from which relevant data are extracted. The data are taken on sample SC030 [(a) and (b)], sample SCSOI_42br [(c) and (d)] and sample SCSOI_42tr [(e) and (f)]. The resistance drift in (c) and (e) is attributed to temperature variations in the lab and heat generated by the magnetic field coils.

amplifier (see section 5.2.2). The external field points along the Py stripe, i.e. $\beta = 0°$, and is swept in steps of 0.5 mT between -20 and +20 mT for the up sweep (black) and between +20 and -20 mT for the down sweep (red). In the regime of $\mu_0|H| > 10$ mT the resistance is almost constant while the magnetic field is swept. When applying an opposing magnetic field in the up (down) sweep the resistance drops by approximately 0.25 Ω towards the minimum at about +3 mT (-3 mT). The minima are assumed to indicate the coercive field. The field position can be explained by a shape anisotropy due to the limited width of the Py stripe. The relevant demagnetizing field is a bit smaller than the value reported in Ref. [Bie13] where Py from the same evaporation plant was taken and deposited on a MgO substrate. Following Ref. [Dem01] one can estimate the demagnetizing field of a ferromagnetic stripe via $\mu_0 H_{\text{dem}} = \frac{2t_{\text{Py}}}{\pi w_{\text{Py}}} \mu_0 M_s = 2.5$ mT with $t_{\text{Py}} = 40$ nm the thickness, $w_{\text{Py}} = 10$ µm the width and $\mu_0 M_s = 0.97$ T [Neu11b]. This value for the demagnetizing field is in a good agreement with the coercive field determined by the fieldsweep above. Additionally the resistance is investigated by rotating a fixed magnetic field of 70 mT [Fig. 6.1 (b)]. The angle of $0°$ marks the direction along the Py stripe. The resistance follows the $\cos^2$-dependency described in section 2.5.1. The relative change in resistance amounts to 0.63 % in the anglesweep but only 0.44 % in the fieldsweep. This fact can be explained as the ferromagnet is very likely to fall into domains close to the coercive field in order to minimize stray fields [Ash76]. As a consequence the resulting overall resistance is not minimal as some domains might point along the direction of the electric current. The MR ratio itself is smaller than the values of $2.0 - 4.0$ % reported in literature [Wan06]. However the reported values strongly depend on the thickness and the surface quality of the thin film.
We obtained similar findings on sample SCSOI_42br. The AMR ratio is extracted to be about 0.56 % [Fig. 6.1 (d)]. The coercive field amounts to approx. +1 mT (-1 mT) [Fig. 6.1 (c)]. However, the overall resistance is about a factor of five higher than in sample SC030. This could possibly have several reasons: As shown in section 4.2.2 the roughness of the aluminum layer during preparation of SCSOI_42br is quite large. This affects of course the roughness of the Py layer prepared on top. As shown in Refs. [Plo06, Ros04] an increased surface roughness influences the resistance of a ferromagnetic thin film. Additionally very high topological features at the surface (as they occurred especially in the edge regions of the Al

layer) could lead to a drastically thinned FM causing higher resistance in a short segment. This segment adds to the overall resistance in series and could dominate. As a last contribution a crack in the Py could reduce the effective width of the Py stripe and add a segment of increased resistance in series. Importantly we do not find the relative AMR effect to be reduced significantly compared to sample SC030.
In order to verify that the Al roughness and suspending process is responsible for the enlarged resistance we perform the same experiment on sample SCSOI_42tr. This sample is prepared on the same chip as SCSOI_42br so that the Py and Pt materials are deposited in one and the same evaporation step. In Fig. 6.1 (e) and (f) we plot the field-dependent and angle-dependent resistance. The field direction of (e) is along the Py stripe, the field strength in (f) is 30 mT. We find that the overall resistance is a factor of approx. 11 smaller compared to the freestanding SOI-based device. This fact supports the explanation that the roughness provoked by the underlying Al layer is responsible for the increased resistance. The AMR ratio in the not underetched sample is higher and amounts to about $1.07\ \%$. The reason for this can be found in the surface of the Py that is supposed to be smoother as Py is deposited directly on the smooth Si wafer. In both measurements shown in Fig. 6.1 (c) and (e) we find that the initial value of the overall resistance (black data point at -35 mT) is different from the end value of the back sweep (red data point at -35 mT). This drift in resistance is attributed to temperature variations through both, variations in the lab temperature and heat produced by the magnetic field coils.

6.2. Laser-induced Seebeck effect

The investigation of spin caloric transport effects [Uch08, Wal11, Qu13] requires the possibility to generate large enough temperature gradients in a ferromagnet. Due to size limitations the occurring absolute temperatures and temperature gradients can usually not be measured directly and have to be determined in a different way. We therefor scan in a further experiment a laser spot over the suspended bridge while detecting voltages at specific contacts in a similar way like in Ref. [Bie13]. In Ref. [Bie13] however thick Au was used for electrical contacts attached to Py. Thus, the ISHE (cp. section 2.5.3) and possible heat-induced spin currents were not studied. The voltage is detected with a lock-in amplifier (see section 5.2.2)

while the laser is modulated with a square wave of a frequency of 171 Hz. In Fig. 6.2 (a) we show data taken along Pt wire 2 on sample SC030 with no current applied. Here, we use laser setup 1 (cp. section 5.2). The laser with a nominal output power of about 8 mW is scanned in the region marked with a red dashed rectangular. The centers of the Pt stripes in x-direction are located at $x = 10,\ 20,\ 30,\ 40$ µm, respectively. The plot includes the spatial information in the x- and y-direction and the voltage value is plotted color-coded. Large positive (negative) voltage means red (blue) color. The measured power reaching the sample is about 660 µW. We find that large absolute voltages occur when the laser is positioned in the contact region where Pt stripe 2 contacts the Py stripe. Roughly at the center of the Py stripe the sign of the voltage changes. These voltages are attributed to the Seebeck effect. The Py/Pt hybrid structure forms a thermocouple as Py and Pt exhibit different Seebeck coefficients S_{Py} and S_{Pt}. An asymmetrical heating of this thermocouple results in a net voltage. At the top side of the contact region the maximum voltage amounts to 140 µV. This voltage difference is a direct measure for the temperature variation within the contact region. This specific temperature can be estimated following Ref. [Bie13] via an effective Seebeck coefficient given as $S_{\text{eff}} = (\sigma_{\text{Pt}} S_{\text{Pt}} + \sigma_{\text{Py}} S_{\text{Py}})/(\sigma_{\text{Pt}} + \sigma_{\text{Py}}) = -6.57$ µV/K, using $\sigma_{\text{Pt}} = 9.44 \times 10^6$ S/m [NDT], $\sigma_{\text{Py}} = \rho_{\text{Py}}^{-1} = 1.1 \times 10^6$ S/m, $S_{\text{Pt}} = -5$ µV/K [Moo73] and $S_{\text{Py}} = -20$ µV/K [Sla11]. The effective Seebeck coefficient is then used to calculate the temperature rise $\Delta T = 140\ \mu V/(S_{\text{Pt}} - S_{\text{eff}}) = 89.2$ K across the width of the Py stripe [i.e. between the top and bottom side of the contact region in Fig. 6.2 (a)]. In order to estimate a rough number for the in-plane temperature gradient in y-direction we assume the gradient to be linear over the 10 µm wide bridge and get a temperature gradient of $\nabla T \approx 9$ K/µm. In x-direction we can estimate the gradient if we take into account that the substrate (e.g. under Pt wire 1) acts as a perfect heat sink. The maximum distance to the substrate region is also 10 µm. With this the gradient in x-direction is at least as large as the estimated gradient in y-direction and could be even larger if the bottom side of the contact region from wire 2 is heated above room temperature while the laser spot is located at the top side.

In Fig. 6.2 (b) we show voltage data taken along the Py wire while the laser is scanned over the structure. Please note that the scanned area slightly differs from the one in the previous graph. The laser parameters are identical.

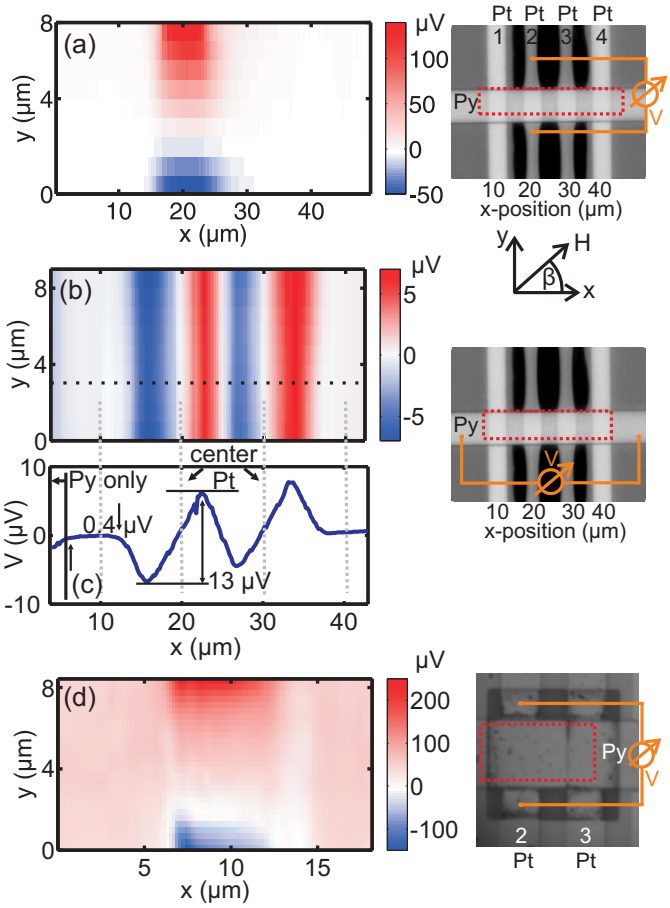

Figure 6.2.: Color-coded position-dependent voltages (left row) with the corresponding measurement geometry (right row). The voltage data is plotted red (blue) for positive (negative) values. Sample SC030: (a) voltage detected along Pt lead 2 while laser (setup 1) is scanned over the area marked by the red rectangle. (b) Almost the same scanning region, but voltage recorded along the Py stripe. Grey dashed lines mark the centers of the Pt stripes. (c) Lineplot from (b) marked by a black dashed line. Sample SCSOI_42br: (d) voltage along Pt wire 2 (laser setup 2).

We find a periodic voltage pattern while scanning over the Py/Pt hybrid region. When the laser spot is positioned on the left side of the crossing region of the Py wire and Pt wires 2 or 3, we find a negative voltage along the Py wire. On the right side we detect a positive voltage respectively. This again is a proof that the assumption of an effective Seebeck coefficient holds for the crossing region of Py and Pt. Otherwise no voltage would be expected in this geometry as the voltage is measured along one and the same Py wire. In Fig. 6.2 (c) we show an exemplary lineplot for a fixed y-value marked by a black dashed line in Fig. 6.2 (b). We find the periodic voltage signal around the inner two Pt stripes at 20 and 30 µm. With increasing x-value we find a trend towards slightly increasing positive voltages. We attribute this to thermal drifts over time as the plot is taken while the laser is scanned from small x-values to large x-values and at each x the y-values are swept. The time difference from small to large x-value of the plot is several hours. Additionally, we find that the large voltage values only occur close to the inner two Pt stripes, although the laser scans also over the outer two ones in the same way. This is explained if we assume the substrate as an efficient heat sink. The temperature difference between the left and the right side of a Pt stripe is expected to be large, when the heat has to flow in the in-plane direction. This causes a large Seebeck voltage. In the case of a not-underetched Pt stripe, most of the heat is supposed to flow directly to the substrate. The in-plane temperature difference between the left and the right side is then expected to be small. We can give a rough estimation of the variation in temperature difference for the underetched and not-underetched case if we have a look at the voltage values. Around Pt stripe 2 (around $x = 20$ µm) the voltage changes from -6.8 µV to +6.2 µV amounting to 13 µV. If we assume the same distances from the center position of the Pt for stripe 1 and evaluate the voltage difference it amounts to about 0.4 µV. We can therefor expect the temperature difference between the left and right side of Pt wire 1 to be in a rough estimation at least a factor of 33 times smaller than for stripe 2. This confirms that the underetching helps to get large temperature differences over a reasonable distance. Please note that the voltage difference of 0.4 µV close to stripe 1 would be even lower if we would subtract the thermal drift discussed above. On the left side of Fig. 6.2 (c) we find that the voltage starts to decrease with decreasing x. This starts just when the laser leaves the Pt/Py/Al structure and reaches the pure Py/Al region on the GaAs substrate. The metal thickness is then 61 nm instead of 76 nm

in the Pt/Py region. We therefor attribute this voltage to a photovoltage as more photons reach the substrate through the thinner metal layer.

Figure 6.2 (d) shows a comparable data set where the laser is scanned on sample SCSOI_42br in a region again marked by a red dashed rectangular. For this measurement not only the sample is changed but also the improved laser setup 2 with a wavelength of 407 nm and a nominal laser output power of 0.5 mW is used (cp. section 5.2). The absolute voltage value is again found to be maximal when the laser spot is positioned on the top/bottom side of the contact region. However the voltage in the areas outside the contact region is not zero in this case but shows a positive base value. The averaged base voltage amounts to 48 μV and is attributed to a photo voltage due to photons reaching the semi-conducting substrate through the illuminated thin bridge [Bie12]. Reasons for the larger base voltage compared to 6.2 (a) might be as follows. In each case the substrate is a semiconductor. In sample SC030 GaAs is used showing a direct band-gap of 1.42 eV. Laser setup 1 provides photons of 2.3 eV energy. For SCSOI_42br the underlying substrate consists of Si exhibiting an indirect band-gap of 1.1 eV and a direct band-gap of 3.4 eV. Laser setup 2 provides photons of 3 eV energy such that direct interband transitions should not play a vital role. In general direct interband transitions are more efficient as indirect transitions as for the latter case phonons have to be involved for the absorption of a photon. We suppose the reason for the increased base voltage in Si to be found in the distance between the place where photons are absorbed in the semiconductor and the place where the electrical contacts are located. For the GaAs-based sample SC030 the underetching of the metallic stripes is on the order of $5-10$ μm deep. Photons are absorbed in this depth and the distance to the metallic leads is large. For sample SCSOI_42br 230 nm underneath the Py bridge there is SiO_2 showing a rough surface. As a consequence photons are reflected diffusively and illuminate the semiconducting side walls of the underetched region. There a photo voltage is generated. The distance to the metallic leads is $20 - 40$ times shorter if compared to the GaAs sample.

6.3. Spin Seebeck effect and anomalous Nernst effect

As described in section 1.1 the freestanding bridges were developed in order to investigate the origin of the predicted transverse spin Seebeck effect [Uch08]. One indication for the spin Seebeck effect is the angular dependency that is depicted in section 2.5.3. Accordingly we have taken angle-dependent data along one Pt stripe for different samples. In Fig. 6.3 (a) we plot the corresponding results on Pt wire 2 of sample SC030 while the laser of setup 1 is centered on lead 3 [see Fig. 6.3 (d)]. The voltage is again detected with a lock-in amplifier (see section 5.2.2). An external magnetic field of 70 mT is externally applied and rotated in the plane of the sample. We find a cosine like behavior with an amplitude of 19 nV with a certain offset voltage of -11 nV. The offset voltage is attributed to a remaining Seebeck voltage and a photo voltage (cp. section 6.2). The maximum values are observed at $\beta = (n + 1) \times 180$ degrees with $n = -2, 0, 2$. At these positions the magnetic field is orientated parallel to the ferromagnetic stripe and perpendicular to the Pt stripes. The measured signature fits to the TSSE (cp. section 2.5.3). However, the sign of the voltage should change if the in-plane temperature gradient direction is changed by 180 degrees. In Fig. 6.3 (b) we show the relevant data for the same laser position like in (a) but this time the voltage is detected on the opposite side of the laser spot, namely at lead 4. Again, a cosine-like voltage with an amplitude of 23 nV plus an offset voltage of 439 nV is detected while the magnetic field is rotated. Nevertheless the sign of the oscillatory part of the voltage does not change. Additionally, as lead 4 is located directly on the substrate one would expect a smaller amplitude as the in-plane temperature gradient is expected to be much smaller. These facts rule out the TSSE as an origin for the detected voltage and supports the findings in experiments on ferromagnets on thin membranes [Ave12, Sch13a]. In the above-mentioned publications the planar Nernst effect is found instead. This is however not the case here due to the symmetry that we observe in our experiment. One further effect that might explain the detected voltages is the longitudinal spin Seebeck effect [Uch10, Bau12]. Here, the voltage is generated by an out-of-plane temperature gradient in a stack of a ferromagnet and a suitable normal metal, i.e. platinum. The contact region of Py and Pt together with a remaining out-of-plane gradient could lead to the voltage signature described above. Such a temperature gradient is especially very likely to occur in the contact region of the Py and Pt stripe as the Pt acts as a heat

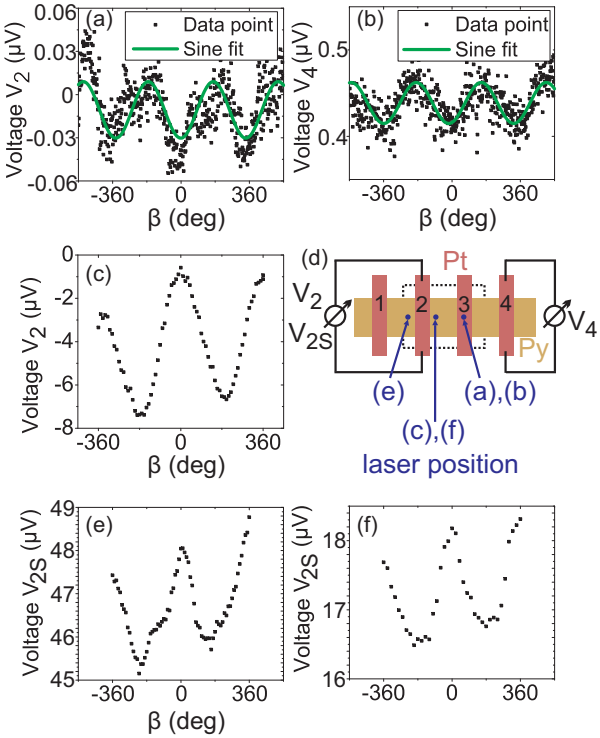

Figure 6.3.: Angle-dependent voltages for different samples and sketch of the particular contacts. (a) and (b) Sample SC030, voltages V_2 and V_4 while the laser spot is positioned on the center of wire 3. The magnetic field strength is 70 mT. (c) Sample SC028, voltage V_2 while the laser is positioned next to wire 2, $H_{ext} = 70$ mT. (d) Sketch of the contacts. (e) and (f) Sample SCSOI_42br, voltages V_{2S} while the laser heats on the left or right side of wire 2. (a)-(c) laser setup 1, (e)-(f) laser setup 2.

sink for the bottom side of the Py while the upper side is on air. However, as the LSSE scales linearly with the area of the FM/NM stack subject to an out-of-plane temperature gradient [Bau12] we can rule out the LSSE as an origin because of the following reason. For the voltage along Pt lead 2 the whole area of the Py/Pt stack can contribute to the LSSE as this stripe is underetched and an out-of-plane gradient is very likely to exist in the whole area. Lead 4 however is attached to the substrate that is supposed to act as an efficient heat sink (cp. simulations in section 6.4). The heat is conducted to the substrate over a short distance. This means that only a small part of the Py/Pt stack is supposed to be subject to an out-of-plane gradient. As the voltage scales linearly with the area where the heat gradient exists we would expect the voltage at lead 4 to be significantly smaller as the one at lead 2. In fact the voltage is 23 nV for lead 4 and 19 nV for lead 2. This rules out the LSSE.

Instead we attribute the detected voltage to the anomalous Nernst effect [Ner87] based on the remaining out-of-plane temperature gradient (section 2.5.4). Taking into account an anomalous Nernst coefficient of $S_{\mathrm{N,Py}} = R_{\mathrm{N}} \times S_{\mathrm{Py}}$ with $R_{\mathrm{N}} = 0.13$ [Sla10] and S_{Py} from section 6.2 the calculated difference in temperature across the thickness of the Py stripe is 7 mK for the above-mentioned amplitude of 19 nV and 9 mK for the amplitude of 23 nV respectively. The voltage detected on the other Pt leads showed the same behavior.

As a reference we investigate the not underetched sample SC028 and record the voltage along Pt lead 2 while the laser spot is positioned next to wire 2 [see Fig. 6.3 (d)]. The angular-dependent data are shown in Fig. 6.3 (c). As before a cosine-like behavior is observed. The amplitude voltage and the offset voltage amount to 3.5 μV and -3.6 μV respectively. These enlarged amplitude and offset values are explained by a larger ANE and photo voltage. The underlying out-of-plane temperature gradient is likely to be enhanced as the ferromagnet is in direct contact with the substrate which acts as an efficient heat sink.

As a control experiment we perform additional measurements on sample SCSOI_42br using laser setup 2. We compare the voltage recorded at lead 2 while we change the external field angle when the laser is placed on the left side [Fig. 6.3 (e)] and on the right side [Fig. 6.3 (f)] of wire 2. The magnetic field strength is set to 30 mT. Again, we do not see a signature of the TSSE and find a cosine-like voltage that is independent from the in-plane temperature direction. However, the absolute voltages are larger

compared to sample SC030. We record an amplitude of 680 nV (950 nV) and an offset of 17.2 μV (46.6 μV) for the laser spot positioned on the left (right) side of Pt lead 2. The enhanced amplitude can be explained by a more inhomogeneous heating of the 65 nm thick Py bridge that is additionally very likely to show a certain roughness. The calculated temperature gradient amounts to 262 mK (365 mK) across the thickness of the Py stripe for the laser positioned on the left (right).

6.4. Simulated temperature gradients

Simulations with Comsol Multiphysics are performed to monitor the heat distribution in the suspended structure and evaluate the expected temperature gradients. Therefor we use the following material parameters:

Material	C_P [J/(g K)]	ρ [10^3 kg/m^3]	λ [W/(m K)]
Pt	0.13	21.45	72
GaAs	0.35	5.32	46
Py	0.45	8.74	30
Al	0.90	2.7	160

Table 6.2.: Heat capacity C_P, density ρ and thermal conductivity λ for the materials used in the model. The values are taken from the Comsol Multiphysics material library and Refs. [Sch, Bie12].

For the simulations the diameter of the laser spot of 1.1 μm is taken from the knife edge experiment with laser setup 1 described in section 5.2. The laser heating is modeled as a heat source following a Gaussian distribution. The diameter is entering the Gaussian function via a definition of the diameter namely $d = 4\sigma$, where σ is the standard deviation. The heating in z-direction across the thickness of the Py stripe is modeled via the penetration depth of the light. The resulting position dependent heat source is given as $P(x, y, z) = (1-R) \cdot P_{\text{in}} \cdot \text{gp}(x) \cdot \text{gp}(y) \cdot \exp(-\alpha_n \cdot z)$ with R the reflectivity, P_{in} the incoming power, $\text{gp}(x)$ and $\text{gp}(y)$ a Gaussian distribution in x and y direction and $\alpha_n = 3.0 \cdot 10^5$ cm^{-1} [Smi65] the attenuation coefficient in Py for light at 500 nm.
Of course some amount of light is reflected from the metal surface and

does not contribute to heating. Therefor we need to determine the reflectivity of Py at a wavelength of 532 nm. The refractive indexes of Py are taken from Ref. [Neu04] and are given as $n = 1.75$ and $\kappa = 2.75$. The reflectivity R can then be calculated via $R = \frac{(n-1)^2+\kappa^2}{(n+1)^2+\kappa^2} \approx 0.54$ [K̈98]. The averaged laser power is detected with a laser power meter while the laser is modulated. The measured power value is 330 µW. However the power meter is measuring with a refresh rate of 20 Hz which is much slower than the laser modulation so that we assume that the power meter shows the averaged value over time. The maximum value is then estimated to be double the measured value meaning 660 µW.
The simulated temperature distribution is shown in Fig. 6.4 (a). The geometry is restricted to a 10 µm wide, 40 nm thick Py stripe and one 5 µm wide, 15 nm thick Pt stripe for simplicity. The heights are leveled via Al layers like in the real sample described in section 4.2.1. The temperature is shown color-coded. Yellow/white color means high temperatures, (dark) red color depicts low temperatures. The center of the heat source is positioned in the center of the Pt stripe and 0.5 µm from the top edge of the Py/Pt contact region. With increasing distance of the spot center the temperature decreases in all directions. In order to evaluate the temperature gradients further we extract the position-dependent values in three directions. Along line 1 in the y-direction [white line in Fig. 6.4 (a)] we can extract an averaged temperature difference of 93 K over a length of 9.5 µm resulting in an averaged gradient of 9.8 K/µm [Fig. 6.4 (b)]. This value is in a good agreement with the measured value of 9 K/µm depicted in section 6.2. The maximal gradient occurs between 0.2 and 0.8 µm away from the center of the laser spot and amounts to 29.4 K/µm. The relevant region is marked by vertical dashed lines in Fig. 6.4 (b). In Fig. 6.4 (c) the position-dependent temperature is plotted along the blue line 2 describing the x-direction. The temperature decreases for increasing distance and reaches room temperature at a distance of 10 µm to the laser spot. There the substrate region starts that acts as an efficient heat sink. The averaged temperature gradient amounts to 15.6 K/µm. The out-of-plane temperature gradient in z-direction is relevant for the anomalous Nernst effect. In the center of the spot the temperature variation over the thickness of the permalloy stripe amounts to 381 mK [Fig. 6.4 (d)]. This value is two orders of magnitude larger than expected from the anomalous Nernst effect measurement. Please note that convection is not considered in the simula-

tions.

As a comparison we perform simulations with identical parameters on a structure that is in direct contact with the substrate and not underetched. We also assume Al layers underneath the structure to stay as close as possible to the previous simulations and for height leveling reasons. In Fig. 6.4 (e) we show the simulated heat distribution in the structure. Again, the heat source is positioned 0.5 µm from the top edge of the Py/Pt contact region. Obviously the heated region is restricted to a much smaller area if compared to the freestanding device. The maximum temperature is only 4.8 K above room temperature what is consistent with our previous explanations that the substrate acts as an efficient heat sink. A more detailed view is given in Figs. 6.4 (f) and (g) where we evaluate the temperature distribution along the two in-plane directions, i.e. along line 3 and line 4. We find that in both cases the temperature decreases from the top value of 297.95 K to almost room temperature within a short distance. For line 3 the maximum temperature gradient is extracted to be about 5.7 K/µm. This is more than a factor of 5 smaller than in the freestanding sample. The averaged gradient over 9.5 µm is about 0.5 K/µm, what is even a factor of 20 lower than the gradient in the underetched device. In both cases, along line 3 and line 4 the temperature drops almost to room temperature within a distance of two or three times the laser spot size. In Fig. 6.4 (h) the temperature drop in z-direction in the center of the spot is shown. Within the Py thickness of 40 nm the temperature is decreased by 797 mK. This value is more than twice the one in the freestanding sample.
In summary we find in the simulations that the underetching of the ferromagnets developed in this thesis helps to increase in-plane temperature gradients. Additionally the enlarged gradients exist over a larger area as the substrate is lacking as an efficient heat sink.

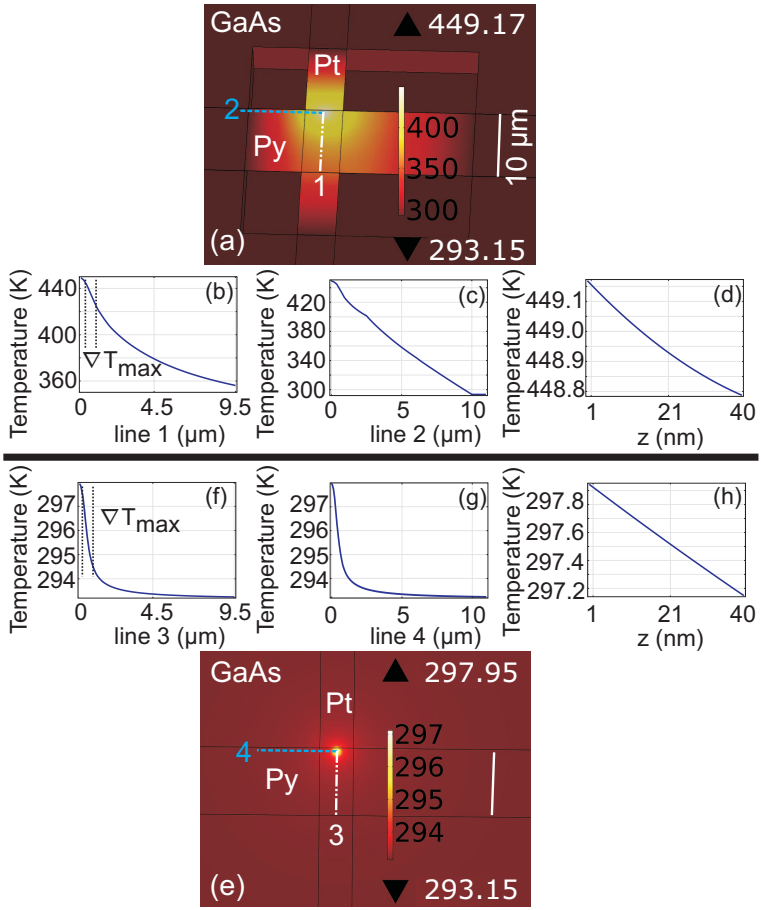

Figure 6.4.: (a) Comsol simulation data. Color-coded temperature distribution in a suspended Py bridge with one Pt contact. (b) Temperature drop along the white line 1. (c) Temperature along the blue line 2. (d) Out-of-plane temperature distribution across the thickness of the Py stripe. Taken at the crossing point of lines 1 and 2. (e) Simulation data for a Py/Pt device attached to the GaAs substrate. (f)-(h) Temperature along line 3, line 4 and in z-direction in the center of the spot.

7. Multiferroic grating coupler and prototype spin wave multiplexer with electric field controllability

In this chapter we investigate hybrid structures consisting of a 47 nm thin ferromagnetic layer CoFeB attached to the ferroelectric substrate $BaTiO_3$. To prevent oxidation of the CoFeB layer a 5 nm thin layer of Au is attached on top. We investigate the ferromagnetic resonance shown by this system. We will discuss the influence of the ferroelectric substrate and the application of external magnetic and electric fields on the properties of the ferromagnetic layer. Thereby we find the magnonic grating coupler effect [Yu13] and realize a prototype spin wave multiplexer [Vog14] with electric field controllability.
We will start the chapter with an investigation on a nominally identical ferromagnetic layer based on a $SrTiO_3$ substrate showing no ferroelectric properties. Therefor general characteristics of the FM thin film are discussed and the principle of ferromagnetic resonance experiments is illustrated.
The samples investigated in this chapter were grown and kindly provided by the group of Prof. Sebastiaan van Dijken in Aalto University School of Science, Finland. The quasistatic properties were investigated by K. Franke. The simulation data shown here were performed by Sampo Hämäläinen from the group of Prof. S. van Dijken.

7.1. Ferromagnetic resonance in thin film CoFeB based on a $SrTiO_3$ substrate

In order to extract basic material properties we investigate a $Co_{40}Fe_{40}B_{20}$ film with a thickness of $d = 47$ nm on a $SrTiO_3$ (STO) substrate. The sample is investigated using the flip chip technique and a 20 µm wide, 9 mm long CPW. In Fig. 7.1 (a) we plot color-coded field-dependent data for the external magnetic field pointing along the long axis of the CPW, i.e. $\eta = 0°$. Dark contrast marks the detected resonances. The plot consists of

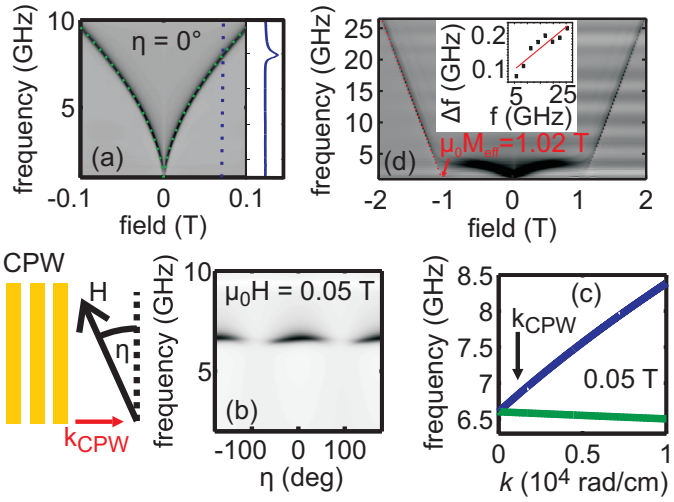

Figure 7.1.: (a) Color-coded field-dependent ferromagnetic resonance data taken on the sample based on $SrTiO_3$ for $\eta = 0°$. Dark contrast marks the resonance. The green dashed line marks the field dependence calculated with the plane-film-model for $\mu_0 M_{sat} = 1.41$ T and $K_{sur} = 10 \cdot 10^{-3}$ J/m^2. (b) Angular-dependent FMR data for an external field of 50 mT. (c) Calculated dispersion branches for DE (blue) and BVMSW (green) configuration. The external field value is 50 mT. The relevant wave vector of the CPW used here is marked. (d) FMR data in the perpendicular field. An effective magnetization of 1.02 T is extracted. Inset: Linewidth vs. frequency for the extraction of the damping parameter of 0.004.

many single spectra. One is shown exemplarily on the right side for a field of 70 mT. There is a spectrum taken every 1 mT starting from -100 mT and ending at +100 mT. We find one prominent mode exhibiting increasing frequency with increasing absolute external field. We find no indication for an anisotropy in this in-plane direction. This is further confirmed by the angle-dependent data at an external field of 50 mT [Fig. 7.1 (b)]. The maximum frequency is given for a field direction along the long axis of the CPW. Like described in section 2.4 the configuration where the magnetization is perpendicular to the wave vector is called the Damon Eshbach geometry. Approaching a magnetic field angle perpendicular to the CPW, the

frequency decreases slightly and the signal strength is drastically reduced. The case $\overrightarrow{M}$ parallel to $\overrightarrow{k}_{\text{CPW}}$ is called Backward Volume Magnetostatic Wave geometry. In the latter case the cross product $\overrightarrow{M} \times \overrightarrow{H}_{\text{eff}}$ entering the signal (cp. section 2.3.1) is minimal explaining the small signal strength. The origin of the change in resonance frequency with external field angle can be seen by regarding the dispersion branches $f(k)$ for the two field configurations mentioned above. In Fig. 7.1 (c) we plot the DE and BVMSW branches for an external field of 50 mT. The underlying formulas were already discussed in section 2.4. The relevant parameters will be discussed below. For the DE branch the frequency increases with rising wave number meaning a positive group velocity $v_g = \frac{d\omega}{dk}$. For the BVMSW the frequency decreases however causing a negative v_g. At the wave vector $k_{\text{CPW}} = 0.096 \cdot 10^4$ rad/cm excited by the CPW used here we get values for $v_g = 12.7$ km/s for DE and $v_g = -0.6$ km/s for BVMSW, respectively. Additionally the frequency at k_{CPW} is about 0.2 GHz larger for the DE case if compared to BVMSW. This explains the shape of the angle-dependent mode shown in (b). Finally in Fig. 7.1 (d) the sample is investigated in a magnetic field pointing perpendicular to the sample plane. The CPW used for the measurement is still the same. Again, one prominent mode occurs. Above a field value of about 1 T the frequency increases linear with the external magnetic field. Below 1 T the frequency exhibits a minimum for zero field and is just increasing slightly for higher fields. Around 1 T a local minimum occurs before the linear increase proceeds. The shape anisotropy due to the small thickness of the magnetic film forces the magnetization to point in the sample plane without an external field applied. With increasing field the magnetization is not completely pointing out of the plane but has still an in plane component as long as the anisotropy field is not overcome. This magnetic state will not be discussed in this work. At the frequency minimum around 1 T the internal magnetic field is minimal and with this the frequency is the lowest. We focus on the high field regime above 1 T where the magnetization is orientated out of the sample plane. In this regime the frequency is described by equation 2.35 considering the effective magnetization M_{eff}. M_{eff} is given by the crossing point of the linear curve at high fields with the field axis. In this sample we find an effective magnetization of $\mu_0 M_{\text{eff}} = 1.02$ T. Additionally we extract the gyromagnetic ratio $\gamma = 28.2$ GHz/T from the slope of the straight line. Following section 2.3.2 the intrinsic damping value α can be determined by plotting

the linewidth as a function of resonance frequency [inset in Fig. 7.1 (d)]. As we plot the linewidth of the magnitude of S21, the linewidth is multiplied with a factor of $1/\sqrt{3}$ [Sta09, Sch13b]. The slope of the straight line is two times the damping, resulting in a damping coefficient of $\alpha = 0.004$. This value is located at the lower edge of literature values of 0.013 [Xu12] and 0.004 [Con13]. The values for γ and M_{eff} enter the plane-film-model given in section 2.4.1. The latter value is used to determine the surface anisotropy K_{sur} via $M_{\text{eff}} = M_{\text{sat}} - \frac{2K_{\text{sur}}}{d\mu_0 M_{\text{sat}}}$. The saturation magnetization $\mu_0 M_{\text{sat}} = 1.41$ T is determined by Vibrating Sample Magnetometry performed by the group of Prof. van Dijken in Finland (not shown). The surface anisotropy is then calculated to be $K_{\text{sur}} = 10 \cdot 10^{-3}$ J/m^2. We use a value for the exchange stiffness $A_{ex} = 28 \cdot 10^{12}$ J/m^2 [Bil06]. However, in the relevant wave vector regime investigated in this thesis, the exchange stiffness influences the resonance frequencies only slightly. Using these values the field-dependent data in Fig. 7.1 (a) can be modeled via the plane-film-model (green dashed line) with quantitative agreement.

7.2. Investigations on thin film CoFeB based on a $BaTiO_3$ substrate

7.2.1. Basic properties and magnetization configuration

We will now focus on thin-film $Co_{40}Fe_{40}B_{20}$ prepared on ferroelectric $BaTiO_3$ substrates. The magnetic film is grown nominally identical to the film in the last section. The $BaTiO_3$ substrate is in the tetragonal phase at room temperature. It exhibits an in-plane polarization showing an almost regular pattern of a_1 and a_2 stripe domains. The width of the stripes is between $5 - 8$ µm. The polarization of each domain encloses an angle of about 45 degree with the domain boundary, i.e. the domain wall between neighboring stripes. A sketch of the sample is shown in Fig. 7.2 (a). The ferroelectric domains induce spatially varying uniaxial anisotropies in the ferromagnet due to inverse magnetostriction [Lah11b, Lah11a]. We call the corresponding areas in the ferromagnet a_1 and a_2 segments. Without an electric and magnetic field applied, the magnetic easy axes also enclose an angle of about 45 degree with the segment boundary and an angle of about 90 degree between neighboring segments. If a large enough electric field is applied across the thickness of the $BaTiO_3$/CoFeB hybrid structure

the polarization in the ferroelectric material points out of the sample plane [Fig. 7.2 (b)]. It was shown that this causes each magnetic easy axis to rotate by about 90 degree and that the strength of the uniaxial anisotropy is significantly increased [Lah12, Fra12].

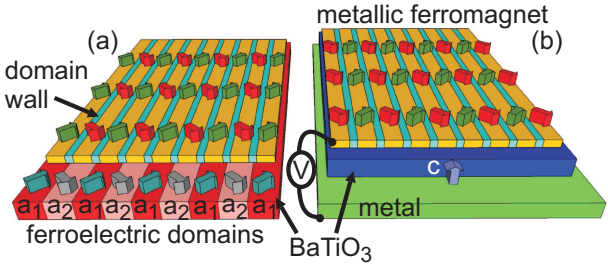

Figure 7.2.: (a) Hybrid structure consisting of the ferromagnet CoFeB (yellow) and the ferroelectric substrate $BaTiO_3$ (dark and light red). Magnetic stripe segments form on top of the ferroelectric a_1 and a_2 domains. The stripe pattern in the ferromagnet is caused by strain transfer and inverse magnetostriction. The blue and grey arrows mark the polarization direction in the ferroelectric domains. Green and red arrows represent the direction of the magnetic easy axes in the ferromagnetic stripe segments. (b) An electric field is applied across the thickness of the hybrid structure. The polarization is rotated out of the sample plane, called c-domain configuration. Strain transfer causes both an in-plane rotation of the magnetic easy axes by 90 degree and an increase of the corresponding anisotropy strength. A metal plate is used as a back electrode. Figure adapted from Ref. [Bra14].

7.2.2. Magneto-optic Kerr effect (MOKE)

Magneto-optic Kerr effect measurements have been performed by Kévin Franke at Aalto University to get insight into the static magnetization properties in the CoFeB film. Therefor an external magnetic field is applied in a certain in-plane direction while simultaneously the magnetization direction is mapped by MOKE. In Fig. 7.3 we plot a set of data where the magnetic field is applied with an angle of 45 degree with respect to the ferroelectric domain walls and is collinear with the easy axis direction of the magnetic segment a_1. At an external field of -60 mT the ferromagnetic film is homogeneously magnetized. At this strength the applied field exceeds the anisotropy field of the a_2 segments and dominates the magnetization di-

rection. The different magnetic segments are not resolved in MOKE as the difference in the magnetization direction is very small. As soon as the field strength is reduced the magnetization of the a_2 segments rotates towards its easy axis and the magnetic stripe pattern occurs. At zero field the magnetization direction is governed by the uniaxial anisotropies in each segment, meaning an angle of 90 degree between the neighboring stripes. If the field is then increased and applied in the opposite direction the magnetization of the a_1 segment switches around 5 mT. The a_2 segment magnetization gradually aligns with the external field when the field strength is further increased. It is found that the static magnetic anisotropy constants differ slightly in both segments. One can determine the anisotropy constants by the slope of the hard-axis hysteresis curves (not shown in this work). We obtain values of $K_{a2} = 2.2 \cdot 10^4$ J/m^3 and $K_{a1} = 1.7 \cdot 10^4$ J/m^3. This is equivalent to anisotropy fields of 36.7 mT and 28.3 mT respectively.

7.2.3. Ferromagnetic resonance with and without electric field applied

Comparable to section 7.1 we position the $BaTiO_3$-based sample on top of the CPW in flip chip geometry [Fig. 7.4 (a)]. The sample is orientated in a way that the ferromagnetic stripe segments are perpendicular to the long axis of the CPW. First, the external field is applied with an angle of $\eta = 45°$ and swept between -60 mT and +60 mT in steps of 0.5 mT. Please note that the angle is identical with Fig. 7.3. The ferromagnetic resonance data show, besides some weaker ones, two prominent modes [Fig. 7.4 (b)]. The origin of the modes with small intensity is not in the focus of this thesis. We will concentrate on the two main modes in the following sections. The upper branch (marked by red squares) shows increasing frequency with rising absolute field values. This behavior is usually attributed to a magnetic configuration where the external field is applied along an easy axis. The lower branch (marked by green circles) however exhibits two minima. This suggests that for this branch the field is pointing along a magnetic hard axis. The scenario is comparable to the measurements in the perpendicular field shown in section 7.1 but the origin of the anisotropy is different. Here the anisotropy field points in a direction in the sample plane and the frequency minimum at a field value of 24 mT also represents the point of a minimal internal field. When we rotate the magnetic field by 90 degree the two sets of branches look similar at a first glance [Fig. 7.4

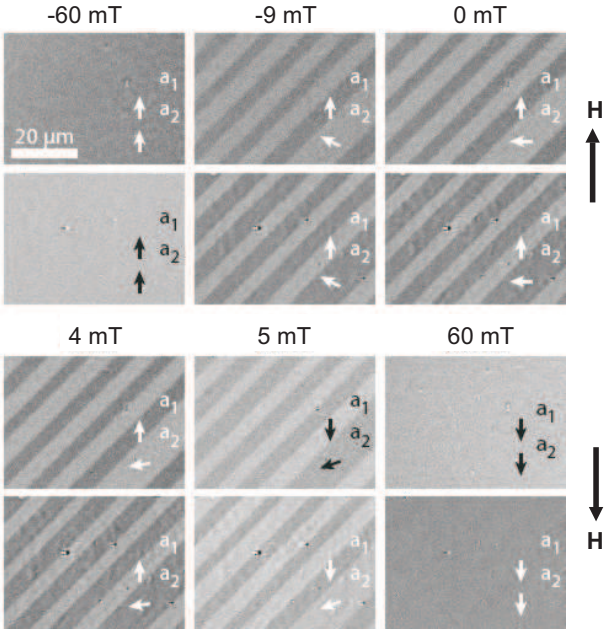

Figure 7.3.: MOKE microscopy images of the CoFeB film on top of the ferroelectric $BaTiO_3$ substrate. The external magnetic field is applied along the vertical axis. The images in the upper (lower) row for each field value are taken with the magneto-optical contrast axis orientated in vertical (horizontal) direction. The magnetization direction in each segment is depicted by the arrows. Figure adapted from Ref. [Bra14].

(c)]. Again there is an upper branch behaving like an easy-axis mode and a lower frequency branch exhibiting two minima. By looking closer we find that the minima positions are however shifted to slightly lower field values, i.e. 22 mT. This is indicative that the anisotropy field, and with this the anisotropy constant, for the lower frequency branch in Fig. 7.4 (c) is lower than in the case of Fig. 7.4 (b). With this and together with the MOKE data above it is obvious that in Fig. 7.4 (b) the upper (lower) branch has its origin in the a_1 (a_2) segment. In Fig. 7.4 (c) the segment allocation is opposite. Additionally we have investigated a nominally identical sample based on $BaTiO_3$ by AESWS. We find comparable resonance frequencies

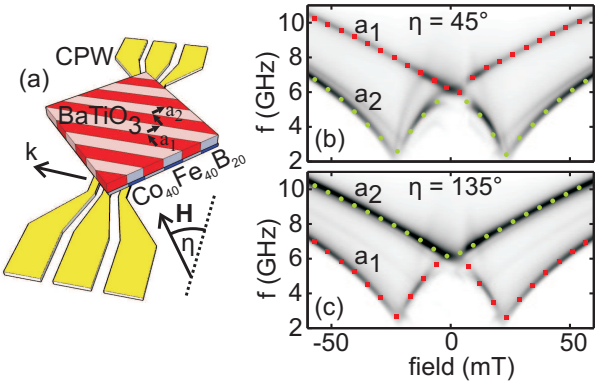

Figure 7.4.: (a) Sketch of the measurement geometry. The hybrid sample is placed with the CoFeB (blue) face down on the CPW (yellow). The $BaTiO_3$ substrate is shown in red. The angle η is defined with respect to the long axis of the CPW. (b) Field-dependent FMR data at an angle of 45°, i.e. $\vec{H}$ is collinear with the easy-axis direction for the a_1 segment and the hard-axis direction for the a_2 segment. (c) Field-dependent data at $\eta = 135^\circ$ consistent with the easy-axis (hard-axis) direction for the a_2 (a_1) segment.

and the same mode profiles. We therefor will not show data on this sample here, but in the appendix A.2.

In the following we provide an overview on the angular dependency of the two modes discussed above. This will give further insight on the mode nature and their origin. We focus on fields larger than the anisotropy fields and show data where the external field of 100 mT is rotated in the plane of the sample between $\eta = -180^\circ$ and $\eta = 180^\circ$ in steps of 2° [Fig. 7.5 (a)]. Consistent with Fig. 7.4 there exist two main branches. Each branch follows a two-fold symmetry and is shifted by 90° with respect to the other branch. The angle showing the highest (lowest) frequency marks the easy (hard) axis direction for modes of the respective branch. Looking closely we find that the minimal frequencies $f_{\mathrm{min,a1}}$ of segment a_1, i.e. at $\eta = -45^\circ$ and $\eta = 135^\circ$ are higher than the minimum frequencies $f_{\mathrm{min,a2}}$ attributed to segment a_2 at $\eta = -135^\circ$ and $\eta = 45^\circ$. These angles describe the hard-axis directions of each mode. The larger the anisotropy is the lower the resonance frequency is expected to be. In Fig. 7.5 (b) we plot the

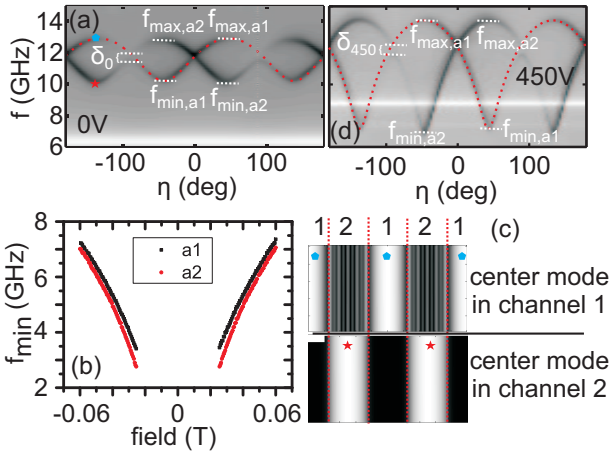

Figure 7.5.: (a) Angle-dependent FMR data on the $BaTiO_3$-based sample for an external field of 100 mT. Two prominent modes are visible. Maximum (minimum) frequency values are located at easy-axis (hard-axis) directions. The red dashed line marks the calculation by the plane-film-model (see section 2.4.1) for a mode at k_{CPW} assuming an infinitely wide film with magnetic properties similar to segment a_1. Relevant values are given in table 7.1. (b) Minimum frequency values for a_1 and a_2 segment in the 0 V case. (c) Micromagnetic simulations: Spatial plots of the spin oscillation amplitude for an external field angle of $\eta = -135°$. White color means large amplitude black color marks no amplitude. Top (bottom) picture gives the amplitude for the upper (lower) frequency branch in the angle-dependent data for the specific angle, marked by blue (red) symbol. (d) Angle-dependent FMR data at 100 mT while an electric field of 450 V is applied across the thickness of the sample. Calculation for the a_1 segment is shown as a red dashed line.

field-dependent minimum frequencies of the two modes that we attribute to segments a_1 and a_2. We find a frequency difference between 0.2 GHz at high fields and 0.7 GHz at low fields. The frequency of the a_1 mode is thereby always higher than a_2 supporting the mode assignment together with the anisotropy strengths from MOKE measurements. The increase in the frequency difference at lower fields confirms that the anisotropy dominates the frequency with decreasing external magnetic field.

In order to finally prove the mode assignment micromagnetic simulations have been performed by S. Hämäläinen at Aalto University to localize the spin excitation in the investigated sample. In Fig. 7.5 (c) we show spatial plots of the magnetization amplitude for a fixed external field angle of $\eta = -135°$ and a fixed frequency. The relevant parameters are $\mu_0 M_{\text{sat}} = 1.4$ T and an anisotropy constant of $K_{\text{uni}} = 15$ kJ/m^3 for both segments. The top picture illustrates the amplitude for the high frequency branch at the considered angle [tagged by the blue pentagon in Fig. 7.5 (a)]. White contrast marks large spin oscillation amplitude, dark contrast means no amplitude. We find the main excitation in channel 1 marking the a1 segment, while in channel 2 there is a standing spin wave with a transverse spin-wave vector given by the finite width w of the channel according to $k = \zeta \frac{\pi}{w}$ with $\zeta \in \mathbb{N}$. In the bottom picture depicting the case of the lower frequency mode [marked by the red star in Fig. 7.5 (a)] the scenario is different. Here, the maximum amplitude is given in channel 2 and almost no spin oscillation is seen in channel 1.

We now investigate how the application of an electric field influences the ferromagnetic resonance. The corresponding angle-dependent data are shown in Fig. 7.5 (d). The symmetry of the branches is equivalent to the case before the electric field was applied. However the frequency values change significantly. The maximum (minimum) frequency values for each mode are higher (lower). This suggests a larger anisotropy for both modes. Furthermore comparing the frequencies in the minima we find that the angle positions of the absolute minima are shifted by 90° compared to the data shown in Fig. 7.5 (a). We can therefor state that in the investigated sample changes in both orientation and strength of the uniaxial anisotropies take place. In each segment the uniaxial anisotropy axis rotates by 90° (cp. section 7.2.1). This was also shown by MOKE experiments in CoFe on $BaTiO_3$ [Lah12, Fra12] and additionally in a nominally

identical sample to the one investigated here[1]. Using the plane-film-model (see section 2.4.1) we can describe each mode and determine basic magnetic parameters (red dashed lines in Figs. 7.5 (a) and (d), only shown for mode a_1). Please note, that the plane-film-model does not consider that each segment consists of 5-8 µm wide stripes. Therefor an additional transverse wave vector due to the finite width that would add up to k_{CPW} could be relevant. Furthermore neighboring domains might be coupled and influence each other, i.e. via stray fields. However, the model is valid for an infinitely extended film with the parameters of one stripe segment. The extracted values from the model might therefor have a certain error bar. We do the fitting for both the as grown sample and at an applied field of 450 V. The following table gives the relevant parameters for the best fits of the a_1 and a_2 modes:

sample state	fundamental mode in segment	$\mu_0 M_{sat}$ [T]	K_{uni} [kJ/m^3]	K_{sur} [mJ/m^2]
as grown	a_1	1.53	13.8	0.1
as grown	a_2	1.53	14.6	0.5
450 V	a_1	1.53	36.1	3.9
450 V	a_2	1.53	37.5	4.5

Table 7.1.: Fitting parameters for the two states of the sample (as grown and saturated at 450 V). For each mode the parameters for the saturation magnetization $\mu_0 M_{sat}$, the uniaxial anisotropy constant K_{uni} and the surface anisotropy K_{sur} are given. The fitting errors of each value are given with $\Delta(\mu_0 M_{sat}) = \pm 0.02$ T, $\Delta K_{uni} = \pm 0.3$ kJ/m^3 and $\Delta K_{sur} = \pm 0.3$ mJ/m^2.

The values for the uniaxial anisotropy deviate from the ones extracted from MOKE measurements in section 7.2.2. However the anisotropy constants extracted from dynamic measurements do not have to be identical to the ones in the static case [Gur96]. After the application of an electric field the anisotropy constants increase by almost a factor of three compared to the as grown values. The a_2 anisotropy stays the strongest one. The saturation magnetization of 1.53 T is slightly higher than the one observed in the nominally identical CoFeB film based on $SrTiO_3$ (1.41 T) from a separate

[1] MOKE data are not shown here. AESWS data on this nominally identical sample are shown in appendix A.2

growth process. The saturation magnetization depends on conditions during growth such as temperature, sputtering rate, etc. [Bil06, Jan11, Lee13]. We consider the discrepancy to be reasonable. Additionally we find that during electric field saturation the surface anisotropy increases. During switching from a_1-a_2 configuration to c-configuration (cp. section 7.2.1) the $BaTiO_3$ crystal experiences structural changes. The lattice is distorted and stresses are transferred to the magnetic film leading to the change in anisotropy. Defects can occur at the surfaces of the magnetic film very likely leading to an enhanced surface anisotropy [Bru88a, Bru88b, Ari99].

7.2.4. Spin wave group velocities

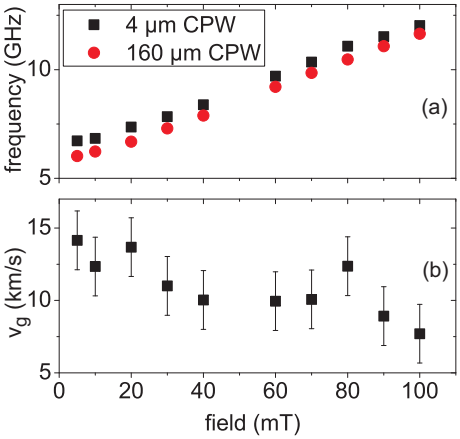

Figure 7.6.: (a) Resonance frequency as a function of the external field for $\eta = 0°$ and two different CPWs with inner conductor widths of 4 µm and 160 µm. (b) Group velocities extracted from frequency values in (a) with the corresponding error bars.

In the following we discuss spin wave group velocities in the ferromagnetic film. Imagine the dispersion branches shown in section 2.4. The group velocity is given by $v_g = \frac{d\omega}{dk}$. A CPW excites with the maximum signal strength at a specific wave vector that depends mostly on the geom-

etry of the CPW [1] (see section 5.1.3). We therefor perform measurements under conditions as identical as possible and use two different CPWs with different w_{ICW}, i.e. 4 µm and 160 µm. The corresponding wave vector for the CPW with $w_{\text{ICW}} = 4$ µm is $k_{\text{CPW,4}} = 0.31 \cdot 10^4$ rad/cm. For the second CPW ($w_{\text{ICW}} = 160$ µm) the wave vector $k_{\text{CPW,160}}$ is about two orders of magnitude smaller and close to $k = 0$. The wave vectors are numerically calculated and consider also the finite skin depth [Sch13b]. We extract the resonance frequencies for different field values in DE-configuration, meaning the external field is applied perpendicular to the wave vector excited by the CPW. In Fig. 7.6 (a) we show the eigenfrequencies as a function of the external field for the two different CPWs. We find a difference of a few 100 MHz over the whole field regime. If we consider a linear slope of the dispersion branch we calculate the group velocity as

$$v_g = \frac{2\pi\Delta f}{\Delta k} \tag{7.1}$$

with $\Delta k = k_{\text{CPW,4}} - k_{\text{CPW,160}} \approx k_{\text{CPW,4}}$ and Δf extracted from Fig. 7.6 (a). The corresponding values are plotted in Fig. 7.6 (b). The group velocities vary between about 8 km/s and 14 km/s and v_g is found to decrease with increasing H. These relatively large velocities and the trend are consistent with the findings on another CoFeB alloy [Yu12].
Now we compare the group velocity data with values from the plane-film-model. The field is applied in a direction perpendicular to the wave vector. The uniaxial anisotropy axis encloses an angle of 45° with both, the field and k. We calculate the dispersion branches for different external field values and determine the slope at the wave vector excited by the CPW. Here, we use the wave number for the CPW with $w_{\text{ICW}} = 20$ µm, that we used throughout this study. The wave vector is $k_{\text{CPW,20}} = 0.096 \cdot 10^4$ rad/cm. We plot the field-dependent group velocities for a plane film with the values of the a_1 mode for both, the sample as grown and at an electric field of 450 V (Fig. 7.7). The relevant parameters are hereby taken from table 7.1. We find $v_g = 11.5$ km/s for a field of 100 mT in the case of the sample as grown. With decreasing field the velocity first increases until it reaches a maximum of 17 km/s at around 20 mT and decreases again towards zero

[1] In fact the CPW excites a distribution of wave vectors around the main peak and shows some higher order excitations. The distribution of wave numbers also contributes to the finite linewidth of the FMR data. The higher order peaks are sometimes seen in spectra as modes of very weak intensity.

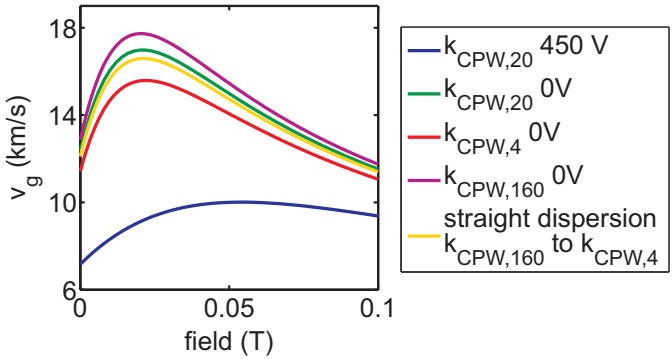

Figure 7.7.: Group velocities calculated with the plane-film-model for the values of a_1 for 0 V at several wave vectors [$k_{CPW,4} = 0.31 \cdot 10^4$ rad/cm (red), $k_{CPW,20} = 0.096 \cdot 10^4$ rad/cm (green) and $k_{CPW,160} \approx 0$ (purple)]. The assumption of a linear dispersion between $k_{CPW,4}$ and $k_{CPW,160}$ is plotted in orange. For the 450 V case the group velocity is plotted for $k_{CPW,20}$ (blue). The relevant parameters for the model are taken from table 7.1.

field. We interpret this trend as follows: At high fields the magnetization is almost aligned with the external field and the geometry is close to DE-configuration. With decreasing field the anisotropy gets more dominant and the magnetization rotates more and more towards the easy axis direction, i.e. 45° with respect to the wave vector. This is an intermediate state between DE and BV configuration and the slope is flatter. For the voltage of 450 V applied the group velocities are smaller all over the field regime. We reach velocities of 9.4 km/s at 100 mT and 10 km/s at the maximum at 54 mT. We have seen before that with the application of the electric field the anisotropy field increases significantly, shifting the maximum in group velocity to higher fields. The calculated group velocities for the a_2 mode (not shown) are slightly smaller than for a_1 but follow the same trend.
With the plane-film-model we want to additionally verify, if the assumption of a linear dispersion between $k_{CPW,4}$ and $k_{CPW,160}$ is justified. We therefor plot the group velocities calculated for the two wave vectors (red and purple lines in Fig. 7.7). We find that the velocities follow the same trend as the values for $k_{CPW,20}$. For $k_{CPW,4}$ the velocities are smaller, while being higher for $k_{CPW,160}$. If we now calculate the velocities via a linearizа-

tion between the two wave vectors as

$$v_g = 2\pi[f(k_{\text{CPW,4}}) - f(k_{\text{CPW,160}})]/(k_{\text{CPW,4}} - k_{\text{CPW,160}})$$

we find that the resulting averaged v_g (orange line in Fig. 7.7) is close to the velocities calculated for the 20 µm CPW that we used throughout our studies.

In a comparison of the data with the calculated velocities from the plane-film-model we find that the experimental data suggest lower velocities and that the trend towards zero field is different. In the experimental data we don't find a maximum around 20 mT but the velocities increase with decreasing field. We attribute the discrepancy especially at lower fields to the fact that the plane-film-model does not consider the finite stripe width of the ferromagnetic segments and segment interaction.

7.2.5. Magnonic grating coupler effect

So far we discussed the overall behavior and found that the plane-film-model in equation 2.50 allows us to remodel measured frequencies over a wide parameter regime (angle, field value). Modeling the two segments a_1 and a_2 as independent entities predicts the crossing of branches close to $\eta = 0°$ and $\eta = 90°$ due to symmetry reasons. We observe however that a frequency separation δ is present at $\eta = 90°$. In order to get further insight in the separation and the different behavior at $\eta = 0°$ we perform field-dependent measurements just at these angles. In Fig. 7.8 (a) and (b) we plot the corresponding data for $\eta = 90°$ and $\eta = 0°$ respectively, both for the as grown sample. In both cases we find that the resonance frequencies increase with rising field. However, in the latter case we find only one prominent branch whereas for $90°$ two branches are clearly visible. The separation between the two branches is called δ_0 for the as grown sample and δ_{450} for the electric field saturated sample. Figure 7.8 (c) shows the field-dependent frequency separations δ_0 and δ_{450}. We find that both increase when the field is lowered. Additionally no significant difference can be found between the separation in the as grown and the saturated sample. In the following we will discuss the origin of δ and find a corresponding model to describe the frequency separation.

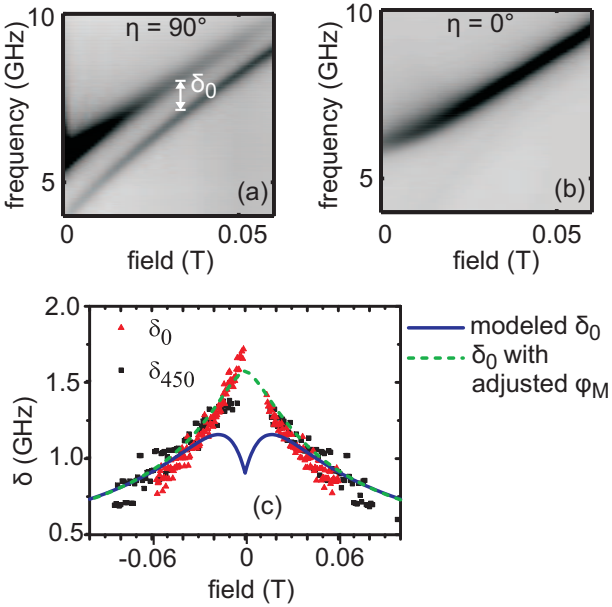

Figure 7.8.: Field-dependent FMR data for (a) $\eta = 90°$ and (b) $\eta = 0°$ including the definition of the frequency separation δ. (c) Frequency separation δ_0 (δ_{450}) for the sample at 0 V (450 V). Blue line: Calculation of the frequency separation. Green dashed line: Hypothetical assumption if angle between external field and magnetization would be halved for each field value.

We perform micromagnetic simulations at $\eta = 90°$ and find the frequency separation there too. In order to learn about the microscopic origin of the frequency separation we show spatial plots of the spin oscillation amplitude A and the corresponding phase information Θ. For the higher frequency branch the spatial plots are shown in Fig. 7.9 (a) for an external field of 98 mT. The plots are arranged as follows: The first column is plotted in the gray scale where light color means high value and dark color means zero. The right column always gives a line plot as cross cut for a fixed y value. In the top row the oscillation amplitude is shown for a fixed frequency, in this case the higher frequency branch. In both kinds of stripes the oscillation amplitude is high in the center of each stripe. Close to the

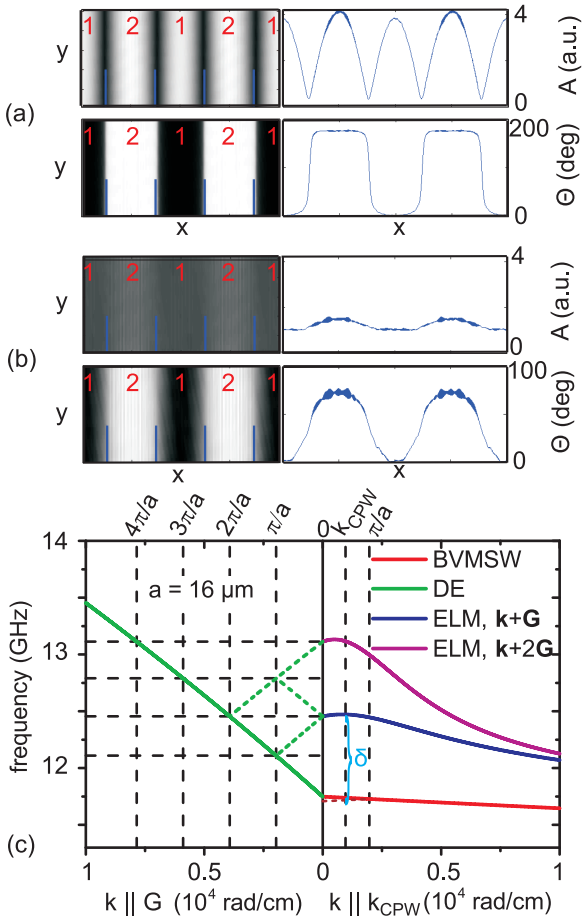

Figure 7.9.: Micromagnetic simulation data of the spin precession amplitude A and the corresponding phase information Θ for (a) the higher frequency and (b) lower frequency mode of Fig. 7.8 (a) for 98 mT. (c) Calculated dispersion branches for the a_1 mode in DE configuration (green) and BVMSW configuration (red). The DE branch is back folded for a periodicity of $a = 16$ µm(broken lines). The dispersion branches for the combined wave vector of first (second) order, $k_{\mathrm{ELM,k+G}}$ ($k_{\mathrm{ELM,k+2G}}$), are plotted in blue (magenta). δ is defined at k_{CPW}. Brown dashed line: Back folded BVMSW branch.

domain walls the amplitude decreases. The lower row of the plots depicts the phase information. We find that the spins in each stripe of the same kind oscillate in phase. There is a phase shift of $180°$ between neighboring stripes. Such kind of oscillation is known for example from phonons and called optical mode [Hel76]. The overall signal strength for inductive detection with a microwave antenna is expected to be weak as anti-phase spin-precessional motion reduces the induced voltage in the CPW. The simulation data for the lower frequency mode are given in Fig. 7.9 (b). We find that the spins precess in both stripes. Taking into account the phase information (bottom row) the stripes oscillate almost in phase. The phase difference amounts to ~ 75 degree and could indicate a forced non-resonant oscillation in one of the two stripes. The behavior of in-phase oscillation can also be compared to phonons where this is called an acoustic mode. The question now is what mechanism is responsible for δ and why it is not visible at $\eta = 0°$. We therefor consider the stripe-like periodic arrangement of the ferromagnetic film investigated here. It was shown by Yu et al. [Yu13] for 2D magnonic crystals that the periodicity of a ferromagnet influences the spin wave properties by adding an additional wave vector to the excitation. This specific wave vector has its origin in the reciprocal lattice vector $G = 2\pi/a$ of the magnonic crystal with a the periodicity. We may remind the reader of Fig. 7.4 (a) where we defined the geometry. In order to find a model describing the separation we imagine two scenarios. First, for the lower frequency mode solely the wave vector of the coplanar waveguide k_{CPW} contributes to the excitation in the homogeneous film that we model. k_{CPW} points along the long axis of the ferromagnetic stripe segments and is collinear with the external magnetic field and - for large fields - the magnetization. The corresponding spin waves are therefor Backward Volume waves and are modeled by the plane-film-model [red dispersion on the right side of Fig. 7.9 (c)]. Second, for the upper mode however we extend the plane-film-model to an empty-lattice-model (ELM) in analogy to Ref. [Kra13]. Here, an artificial periodicity is introduced to the homogeneous material. The periodicity gives rise to a reciprocal lattice vector G pointing perpendicular to the long axis of the ferromagnetic stripe segments and perpendicular to the external field and magnetization, meaning DE configuration. The dispersion for this direction is given on the left side of Fig. 7.9 (c) and is for the first calculated by the plane-film-model for wave vectors collinear with G. When we now use the ELM a combination of the two wave vectors enters the model where G adds up to $k_{||}||k_{\mathrm{CPW}}$

to a combined wave vector $k_{\text{ELM,k+G}} = \sqrt{k_{||}^2 + G^2}$ pointing in a direction between the two single wave vectors. This leads to additional frequencies in the center of the Brillouin zone ($k = 0$). These frequencies correspond to the values that we would get for spin waves with wave vectors at the lattice vector G and its multiples. In the plot we show this correlation by backfolding the pure DE dispersion at the Brillouin zone boundary, namely at $2\pi/a$. We choose $a = 16$ µm as period of the stripes ($G = 0.3927 \cdot 10^4$ rad/cm). The resulting dispersion considering $k_{\text{ELM,k+G}}$ is plotted in blue on the right side of Fig. 7.9 (c). Please note that the combined wave vector rotates more and more towards the direction of k_{CPW} with increasing k. For clarity we show the dispersion $f(k)$ also for $k_{\text{ELM,k+2G}} = \sqrt{k_{||}^2 + (2G)^2}$, where we back fold at $2G = 4\pi/a$. The frequency separation δ is extracted by subtracting the frequencies of the BVMSW branch for $k_{||}$ from the branch considering $k_{\text{ELM,k+G}}$, both at the specific wave vector value of $k_{\text{CPW}} = 0.096 \times 10^4$ rad/cm. At this wave vector the angle between the combined wave vector $k_{\text{ELM,k+G}}$ and k_{CPW} is 76°.

We calculate these dispersion branches for the as grown sample for several external field values and get the field-dependent frequency separation. We therefor use the parameters for the a_1 segment. We compare the model with the extracted values from the dataset [blue line in Fig. 7.8 (c)]. We find that the separation is the lowest at 100 mT, increases for decreasing field, reaches a maximum at ~ 20 mT and lowers towards zero field again. We find a good agreement with the model for high fields above 20 mT. If we would assume a stripe width of only 5 µm the correspondence would be worse, as the calculated frequency separation would be larger by some 100 MHz. We therefor considered the upper limit of the stripe width (8 µm) determined by microscopy for the modeling. For lower fields the data suggest an increasing separation while the model gives decreasing values. We would like to remind the reader that the plane-film-model as well as the ELM do not consider interactions between neighboring stripes. Especially for low fields, when the magnetizations in a_1 and a_2 segments rotate away from each other there might be additional contributions like stray fields from the next neighbors. In order to get a feeling for the extent of deviation from the model we made a hypothetical assumption where we change the following: Due to the anisotropy field the magnetization will in general not point exactly in the direction of the external field when the latter is not pointing in the easy- or hard-axis direction (cp. Fig. 2.5). This

"misalignment" of the magnetization is bigger for low external fields as the anisotropy field has a greater influence. We now assume that the calculated angle between the magnetization and the external field is halved for every field value. We plot the result where we adjusted the magnetization's in-plane angle φ_M in Fig. 7.8 (c) and find that the separation now increases continuously for descending field. The correspondence with the data is quite good.
One question remains: Why is the effect only visible for $\eta = 90°$ and not for $\eta = 0°$ although the symmetry of easy axis and external field is identical? The answer can be given by regarding Fig. 7.9 (c) again. For $\eta = 0°$ the pure spin wave mode for k_{CPW} is of DE character. The dispersion branch for G however would be of BVMSW character. If we would then generate the combined wave vector dispersion we would have to backfold the BVMSW branch. As shown on the right side of Fig. 7.9 (c) the backfolding for G would generate only a very small frequency separation of 40 MHz (brown dashed line). As the typical linewidth of CoFeB is several 100 MHz this separation can not be resolved in the experiment.

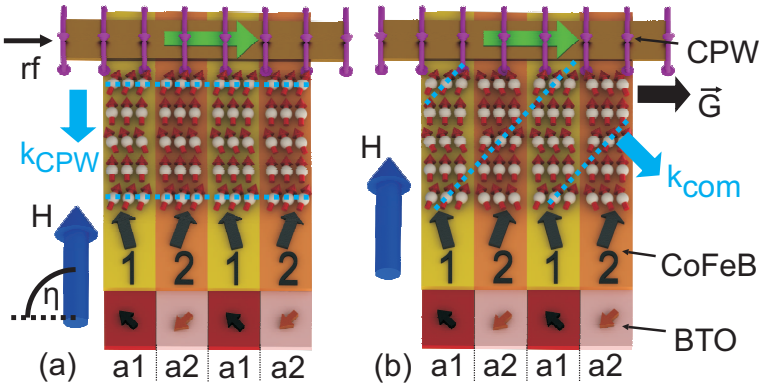

Figure 7.10.: Graphic of (a) the acoustic and (b) the optical mode in the ferromagnetic stripes for $\eta = 90°$. (a) An rf current through the CPW excites an spin waves travelling along k_{CPW} with wavelength λ_{CPW}. Spins in neighboring stripes oscillate in phase, the wave fronts are parallel to the CPW. (b) The periodicity of the 1D magnonic crystal contributes a wave vector G. Spins in neighboring stripes oscillate in antiphase. Waves with a wavelength $\lambda_{\mathrm{com}} < \lambda_{\mathrm{CPW}}$ travel under a finite angle with respect to the CPW.

In order to summarize the physical meaning of the magnonic grating coupler effect discussed above we would like to refer the reader to Fig. 7.10. Here we show a sketch of the hybrid structure of $BaTiO_3$ and CoFeB with an included antenna. In the first case of an acoustic mode all spins with the same distance to the antenna are oscillating in phase in both kinds of stripes. The antenna is exciting a spin wave where the wave front is parallel to the antenna with a wavelength of $\lambda_{\mathrm{CPW}} = 2\pi/k_{\mathrm{CPW}}$. In the second case of an optical mode spins in one kind of stripe oscillate in anti-phase with spins in the other kind of stripe while they have the same distance to the antenna. The wave fronts travel away from the antenna under a certain angle. The angle depends on k_{CPW} and the periodicity a of the 1D magnonic crystal. Here, the wavelength λ_{com} of the magnonic grating coupler spin wave is much smaller than λ_{CPW}.

7.2.6. Prototype spin wave multiplexer with electric field controllability

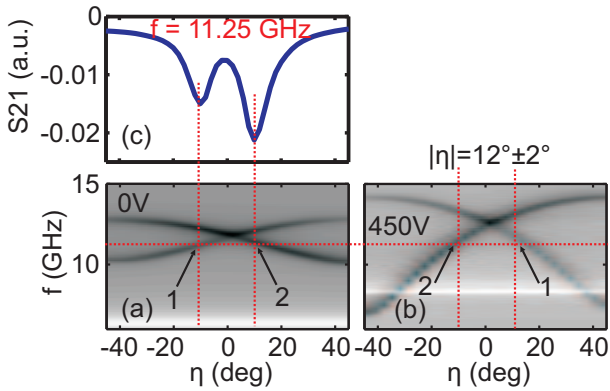

Figure 7.11.: Blowups of the angle-dependent FMR data for η between -45° and +45° for (a) 0 V and (b) 450 V. The resonances match for a fixed frequency of 11.25 GHz and external field angles of $\eta = \pm 12°$. (c) Line plot of S21 versus angle at a fixed frequency of $f = 11.25$ GHz. Discrete steps in branches of (b) reflect the digital stepsize of the angle.

In section 7.2.3 we discussed the angle dependent data for the as grown

sample and the electric field saturated sample. We have already shown that the two prominent modes originate in spin oscillations in the a_1 and a_2 segment respectively and that the two easy axes rotate by 90° when an electric field is applied. Now we focus on the angle regime around $\eta = 0°$. In Fig. 7.11 (a) and (b) we show blowups for angles between $\eta = -45°$ to $\eta = 45°$ of the angle-dependent data for the sample as-grown and at 450 V respectively. In both cases one mode is continuously increasing in frequency while the other one decreases. The two modes cross at about $\eta = 0°$. In the case of 0 V the rising mode is the a_1 mode and the falling one is the a_2 mode. At 450 V this is opposite. In the following we focus on a fixed frequency of $f = 11.25$ GHz. We find that for the 0 V (450 V) case at an external field angle of $\eta = -12°$ the resonance condition for the a_1 (a_2) mode and at $\eta = +12°$ the condition for the a_2 (a_1) mode is fulfilled [cp. also Fig. 7.11 (c)]. We have shown that each mode has its origin in a large spin oscillation in the particular stripes. We now go a step further and attribute the channels with large spin oscillation as active channels where spin waves can propagate along the long axis of the segments, i.e. along the wave vector k_{CPW}. We consequently interpret the findings as switchable spin wave channels. Considering the fixed frequency we find that at $\eta = -12°$ the active spin channel is set to channel 1 [Fig. 7.12 (a)]. This means that spin waves travel along channel 1 only. As the configuration is close to DE geometry we expect large group velocities. If we now rotate the external field to $\eta = +12°$ the active channel is switched to channel 2 [Fig. 7.12 (b)]. Additionally, staying at the same frequency and at one fixed angle, i.e. $\eta = -12°$, the application of an electric field of 450 V leads to a switching of the channels too as the two modes are shifted by 90° like described above [Fig. 7.12 (c)]. We thereby realized a prototype spin wave multiplexer [Vog14] where the propagation path of a spin wave is controlled either by the rotation of the magnetic field or the application of an electric field. The spin waves could thereby be excited by an integrated microwave antenna driven at a constant frequency. Please note that the polarization effect is up to now non reversible. Future materials may give the possibility to reversibly switch spin channels by an electric field.

Remark: In electronics by definition a multiplexer is a device which is used to selectable connect multiple inputs with one output. One input is chosen and connected with the output. The counterpart is called a demultiplexer that connects one input to one of several outputs. In the case of the proto-

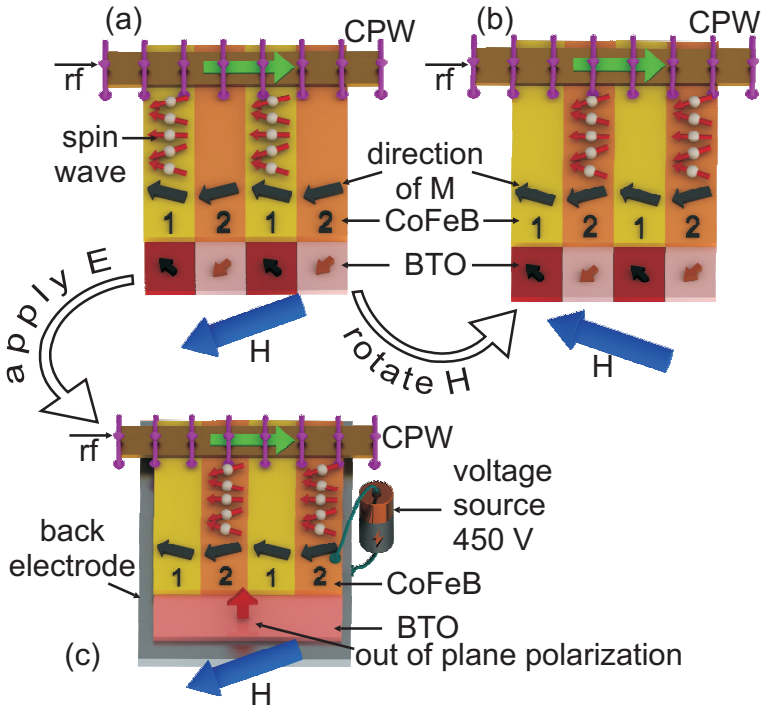

Figure 7.12.: Sketch of a prototype spin wave multiplexer based on the $BaTiO_3$/CoFeB hybrid structure. (a) At $\eta = -12^\circ$ the spin waves excited by the antenna travel in stripes/channels 1. The channel can be switched to channel 2 either by (b) rotating the magnetic field to $\eta = +12^\circ$ or by (c) application of an electric field of 450 V across the thickness of the sample. For the latter case a back electrode is integrated.

type spin wave multiplexer shown above one can think of both: One input signal (microwave in the antenna that excites a spin wave) is selectable connected to two different outputs (channel 1 and channel 2). In this sense this would be a demultiplexer. However, the effect described above is bidirectional, as one can also think of a spin wave propagating in channel 1 or channel 2 (two inputs) that is detected by the antenna (one output). We stay therefor with the term multiplexer. Furthermore we want to point out that the electric field does not have to be applied globally for the whole sample. Instead the local application of an electric field for single or few stripes could lead to a more sophisticated logic device.

8. Summary and Outlook

In this thesis we have investigated two aspects of spintronics: spin caloritronics in freestanding ferromagnets and magnonics in multiferroic hybrid structures. We will summarize these two topics and give an outlook separately in the following.

8.1. Laser heating of freestanding ferromagnets

We investigated thermal effects in freestanding Py ferromagnets with Pt contacts. We therefor developed new preparation processes to realize these suspended structures. The implementation of the temperature gradients was done by laser heating. The respective measurement setup was developed and created in the course of this thesis. We found the AMR effect in the freestanding structures as well as the conventional Seebeck effect. From the latter experiment we determined the in-plane temperature gradients to be on the order of 10 K/µm and found that the exclusion of the substrate as a heat sink increases the in-plane temperature gradient. Initially the experiments should address the transverse spin Seebeck effect (TSSE). However, we found no evidence for the TSSE. Instead, we observed the signature of the anomalous Nernst effect that occurs due to a small out-of-plane temperature gradient on the order of $10 - 100$ mK. We performed simulations with Comsol Multiphysics to verify the order of magnitude of the temperature gradients.
Although we could not observe the TSSE in the suspended ferromagnets the results and techniques developed during this thesis can be used for future experiments. Ferromagnetic nanotubes [RÏ2] consisting of a GaAs core with a diameter of about 100 nm that are coated with ferromagnetic material either by evaporation, sputtering or atomic layer deposition have already been shown to be interesting structures for spin caloritronics [1]. The laser-based heating setup offers the possibility to implement local heat gradients in the nanotube that might be used for the controlled movement of

[1] Measurements are already performed by the master students Johannes Mendil and Shengda Wang

domain walls exemplarily. Furthermore, the freestanding ferromagnets can be interesting for further experiments in spin caloritronics where in-plane temperature gradients are key and where the substrate as a heat sink has to be avoided. Examples are given with the ferromagnetic nanomachines presented in Refs. [Kov10, Bau10b] and the magnetic Seebeck effect that has been reported for an insulting ferrimagnet so far [Bre13]. The latter effect is based on the coupling between a heat current and the magnetization precession. A possible sample setup is sketched in Figure 8.1. An underetched ferromagnet is heated with a laser spot and the influence of the heat current on the magnetization precession can be detected with a coplanar waveguide. The preparation technique reported in this thesis combined with the laser-based heating setup could be very helpful to promote the corresponding research.

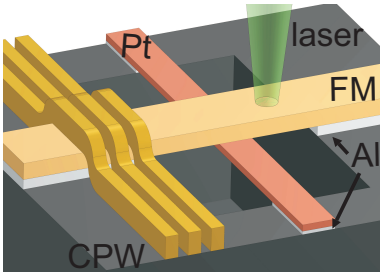

Figure 8.1.: Sketch of a possible sample design for experiments on the magnetic Seebeck effect [Bre13].

8.2. Multiferroic hybrid structures

We investigated spin waves in a CoFeB plane film and in multiferroic hybrid structures consisting of a ferromagnetic CoFeB film on a ferroelectric $BaTiO_3$ substrate. For the experiments we used the all electrical spin wave spectroscopy technique. We determined a low damping parameter of the CoFeB in perpendicular fields in a plane-film sample and investigated the magnetization configuration with the magneto-optic Kerr effect in the hybrid structure. We found a periodic array of ferromagnetic stripe segments a_1 and a_2 with uniaxial anisotropies pointing in the plane of the sample

and rotated $90°$ between neighboring stripes. The application of an electric voltage of 450 V across the thickness of the ferroelectric substrate caused a rotation of the uniaxial anisotropy axes by $90°$ and an increase in anisotropy strength of about a factor of 3. Combining ferromagnetic resonance experiments with micromagnetic simulations we could identify two main resonances that were attributed to the two different stripes. We implemented a plane-film-model known from the literature which provides the possibility to calculate the resonance frequencies for arbitrary in-plane anisotropies. Large spin wave group velocities up to $15-18$ km/s have been determined by both experimental techniques and the calculation with the plane-film-model. The model was also used to extract relevant anisotropy constants. For a large magnetic field orientated along the long axis of the stripes we found a frequency separation that could be attributed to the magnonic grating coupler effect due to the periodic anisotropy variation. Spin waves are therefor propagating not only along the wave vector k_{CPW} excited by the antenna but also along other directions given by a combined wave vector of reciprocal lattice vector of the magnonic crystal and k_{CPW}. The plane-film-model was extended to an empty-lattice-model including the corresponding reciprocal lattice vector. We closed the chapter with the interpretation of the investigated hybrid structure as a prototype spin wave multiplexer. The propagation path of spin waves at a fixed frequency can be switched either by the rotation of the magnetic field or by the application of an electric field. The magnonic grating coupler effect as well as the prototype spin wave multiplexer that we combined in one and the same sample here can be used for future spin wave based electronics.
Future experiments might address several aspects. New substrate materials might provide the possibility to reversibly switch the polarization of the ferroelectric. This would even more fuel the perspectives of the hybrid structure as a logic device. Additionally reversible phase transitions of ferroelectric substrates could be used to create a new degree of freedom and further anisotropies in the ferromagnetic film by switching the temperature between two phases. Furthermore an adjustable width of ferromagnetic stripe domains can provide omnidirectional spin wave propagation due to the grating coupler effect and provide additional aspects for future spintronics devices. In addition, if the application of a fast electric field modulation could be realized the described hybrid structure could be interesting for the excitation of surface acoustic waves in the GHz regime that could drive the ferromagnetic resonance like described by Dreher et

al. [Dre12].

A. Appendix

A.1. List of Abbreviations

Abbreviation	Explicit
PMMA	polymethyl metacrylate
AESWS	All Electrical Spin Wave Spectroscopy
ELM	empty-lattice-model
VNA	Vector Network Analyzer
Py	Permalloy ($Ni_{80}Fe_{20}$)
CoFeB	Cobalt Iron Boron ($Co_{40}Fe_{40}B_{20}$)
CPW	Coplanar waveguide
MSFVW	Magnetostatic forward volume wave
BVMSW	Backward volume magnetostatic wave
MSSW	Magnetostatic surface wave
DE	Damon-Eshbach
MC	Magnonic crystal
BZ	Brillouin zone
FM	Ferromagnet
SEM	Scanning electron microscopy
FMR	Ferromagnetic resonance
e-lit	electron beam lithography
SW	Spin wave
1D	one dimensional
2D	two dimensional
3D	three dimensional
rf	radio frequency
S-Parameter	Scattering parameter
MOKE	Magneto-optic Kerr effect

A.2. Second sample based on $BaTiO_3$

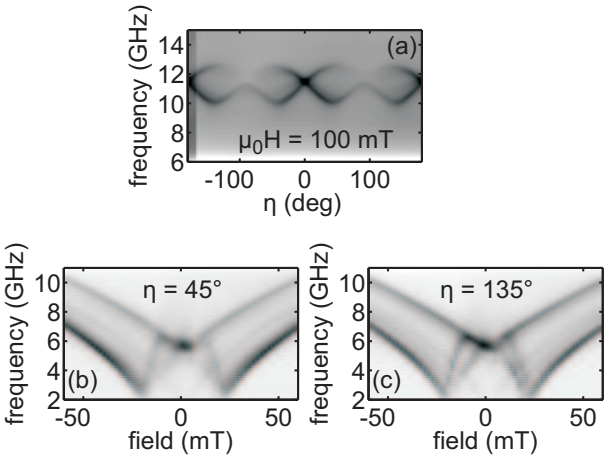

Figure A.1.: (a) Angle-dependent FMR data on a second $BaTiO_3$-based sample that is nominal identical to the first sample for an external field of 100 mT without electric field applied. (b) and (c) Field-dependent data for $\eta = 45°$ and $\eta = 135°$.

A second sample based on $BaTiO_3$ that is nominal identical to the sample investigated in chapter 7 is investigated. We find comparable resonance frequencies and the same mode profiles. In Fig. A.1 (a) the angle-dependent data are shown for an external field of 100 mT. A spectrum is taken every $2°$. The two modes that can be attributed to a_1 and a_2 segments are found. Furthermore, we find the frequency separation δ at $\eta = \pm 90°$ while this separation is missing at $\eta = 0°$. The color scale is reduced by a factor of about 3 as the signal strength is smaller by this value. The reason for this might be a dirt particle between the sample and the CPW. The distance between the ferromagnetic film and the antenna is thereby increased and the signal is smaller. Additionally close to $\eta = -180°$ the contrast is different. We attribute this disturbance to a slight movement of the sample during the measurement. With the plane-film-model we extract the relevant uniaxial anisotropy parameters to be $K_{\text{uni,a1}} = 13.8$ kJ/m^3 for the a_1 segment and $K_{\text{uni,a2}} = 13.5$ kJ/m^3 for the a_2 segment. The saturation magnetization and surface anisotropy for both segments is extracted to be about $\mu_0 M_{\text{sat}} = 1.47$ T and $K_{\text{sur}} = 0.1$ mJ/m^2. We find that for this sample - in contrast to the sample in chapter 7 - the anisotropy is slightly larger for the a_1 than for the a_2 segment. The relevant physics

we discussed in chapter 7 however is supposed to stay unaffected from this small difference. Solely the working frequency of the prototype spin wave multiplexer might be adjusted slightly. In Fig. A.1 (b) and (c) we show field-dependent data for external field angles of $\eta = 45^\circ$ and $\eta = 135^\circ$, respectively. A spectrum is taken every 2 mT between -60 mT and +60 mT. We find the same two prominent modes in both plots like discussed in chapter 7. The modes with weaker intensity are again not discussed.

This sample has not been polarized with an electric field during AESWS. Instead the sample was taken to Aalto University, Finland to perform electric field-controlled investigations there. Data on these experiments are not shown here.

List of Figures

Bibliography

[Aha06] A. Aharoni: *Introduction to the Theory of Ferromagnetism*, Oxford University Press, New York, 2006.

[Ari99] R. Arias and D. L. Mills: *Extrinsic contributions to the ferromagnetic resonance response of ultrathin films*, Phys. Rev. B **60**, 7395 (1999).

[Arn23] H. Arnold and G. Elmen: *Permalloy, an alloy of remarkable magnetic properties*, Journal of the Franklin Institute **195**, 621 (1923).

[Ash76] N. Ashcroft and N. Mermin: *Solid state physics*, Science: Physics, Saunders College, 1976.

[Ave12] A. D. Avery, M. R. Pufall and B. L. Zink: *Observation of the Planar Nernst Effect in Permalloy and Nickel Thin Films with In-Plane Thermal Gradients*, Phys. Rev. Lett. **109**, 196602 (2012).

[Bai88] M. N. Baibich, J. M. Broto, A. Fert, F. N. Van Dau, F. Petroff, P. Etienne, G. Creuzet, A. Friederich and J. Chazelas: *Giant Magnetoresistance of (001)Fe/(001)Cr Magnetic Superlattices*, Phys. Rev. Lett. **61**, 2472 (1988).

[Bau10a] G. E. Bauer, A. H. MacDonald and S. Maekawa: *Spin Caloritronics*, Solid State Commun. **150**, 459 (2010).

[Bau10b] G. E. W. Bauer, S. Bretzel, A. Brataas and Y. Tserkovnyak: *Nanoscale magnetic heat pumps and engines*, Phys. Rev. B **81**, 024427 (2010).

[Bau12] G. E. W. Bauer, E. Saitoh and B. J. van Wees: *Spin caloritronics*, Nature Mater. **11**, 391 (2012).

[Ber70] L. Berger: *Side-Jump Mechanism for the Hall Effect of Ferromagnets*, Phys. Rev. B **2**, 4559 (1970).

[Bie12] A. von Bieren: *Spin and heat transport in magnetic nanostructures*, Dissertation, École Polytechnique Fédérale de Lausanne (2012).

[Bie13] A. von Bieren, F. Brandl, D. Grundler and J.-P. Ansermet: *Space- and time-resolved Seebeck and Nernst voltages in laser-heated permalloy/gold microstructures*, Appl. Phys. Lett. **102**, 052408 (2013).

[Bil06] C. Bilzer, T. Devolder, J.-V. Kim, G. Counil, C. Chappert, S. Cardoso and P. P. Freitas: *Study of the dynamic magnetic properties of soft CoFeB films*, J. Appl. Phys. **100**, 053903 (2006).

[Bil07a] C. Bilzer: *Microwave susceptibility of thin ferromagnetic films: metrology and insight into magnetization dynamics*, Dissertation, Université Paris-sud 11, Faculté des sciences d'Orsay (2007).

[Bil07b] C. Bilzer, T. Devolder, P. Crozat, C. Chappert, S. Cardoso and P. P. Freitas: *Vector network analyzer ferromagnetic resonance of thin films on coplanar waveguides: Comparison of different evaluation methods*, J. Appl. Phys. **101**, 074505 (2007).

[Bin89] G. Binasch, P. Grünberg, F. Saurenbach and W. Zinn: *Enhanced magnetoresistance in layered magnetic structures with antiferromagnetic interlayer exchange*, Phys. Rev. B **39**, 4828 (1989).

[Bla05] J. A. C. Bland and B. Heinrich: *Ultrathin Magnetic Structures III: Fundamentals of Nanomagnetism; electronic version*, Springer-Verlag Berlin and Heidelberg GmbH & Co. KG, Dordrecht, 2005.

[Blo30] F. Bloch: *Zur Theorie des Ferromagnetismus*, Zeitschrift für Physik **61** (1930).

[Blu01] S. Blundell: *Magnetism in Condensed Matter (Oxford Master Series in Physics)*, Oxford University Press, USA, 2001.

[Boc07] L. Bocklage, J. M. Scholtyssek, U. Merkt and G. Meier: *Spin polarization of Ni2MnIn and Ni80Fe20 determined by point-contact Andreev spectroscopy*, J. Appl. Phys. **101**, 09J512 (2007).

[Boo14] S. R. Boona, R. C. Myers and J. P. Heremans: *Spin caloritronics*, Energy Environ. Sci. **7**, 885 (2014).

[Bor12] K. Bordo and H.-G. Rubahn: *Effect of Deposition Rate on Structure and Surface Morphology of Thin Evaporated Al Films on Dielectrics and Semiconductors*, Materials Science **18**, 313 (2012).

[Bot06] B. Botters, F. Giesen, J. Podbielski, P. Bach, G. Schmidt, L. W. Molenkamp and D. Grundler: *Stress dependence of ferromagnetic resonance and magnetic anisotropy in a thin NiMnSb film on InP (001)*, Appl. Phys. Lett. **89**, 242505 (2006).

[Bra14] F. Brandl, K. Franke, T. Lahtinen, S. van Dijken and D. Grundler: *Spin waves in CoFeB on ferroelectric domains combining spin mechanics and magnonics*, Solid State Commun. **198**, 13 (2014).

[Bre13] S. D. Brechet, F. A. Vetro, E. Papa, S. E. Barnes and J.-P. Ansermet: *Evidence for a Magnetic Seebeck Effect*, Phys. Rev. Lett. **111**, 087205 (2013).

[Bru88a] P. Bruno: *Dipolar magnetic surface anisotropy in ferromagnetic thin films with interfacial roughness*, J. Appl. Phys. **64**, 3153 (1988).

[Bru88b] P. Bruno: *Magnetic surface anisotropy of cobalt and surface roughness effects within Neel's model*, Journal of Physics F: Metal Physics **18**, 1291 (1988).

[Car97] G. Carlotti, G. Gubbiotti, F. Hickernell, H. Liaw and G. Socino: *Comparative study of the elastic properties of polycrystalline aluminum nitride films on silicon by Brillouin light scattering*, Thin Solid Films **310**, 34 (1997).

[Car00] M. Cardona and G. Güntherodt: *Light Scattering in Solids VII: Crystal-Field and Magnetic Excitations*, Springer-Verlag GmbH, 2000.

[Chi97] S. Chikazumi and C. Graham: *Physics of Ferromagnetism*, International Series of Monographs on Physics, Clarendon Press, 1997.

[Con13] A. Conca, J. Greser, T. Sebastian, S. Klingler, B. Obry, B. Leven and B. Hillebrands: *Low spin-wave damping in amorphous Co40Fe40B20 thin films*, J. Appl. Phys. **113**, 213909 (2013).

[Cou04a] G. Counil, J.-V. Kim, T. Devolder, C. Chappert, K. Shigeto and Y. Otani: *Spin wave contributions to the high-frequency magnetic response of thin films obtained with inductive methods*, J. Appl. Phys. **95**, 5646 (2004).

[Cou04b] G. Counil, J.-V. Kim, K. Shigeto, Y. Otani, T. Devolder, P. Crozat, H. Hurdequint and C. Chappert: *Inductive measurement of the high frequency permeability of a Permalloy thin film*, Journal of Magnetism and Magnetic Materials **272-276**, 290 (2004).

[Cul09] B. Cullity and C. Graham: *Introduction to Magnetic Materials*, Wiley, 2009.

[Dam61] R. Damon and J. Eshbach: *Magnetostatic modes of a ferromagnet slab*, Journal of Physics and Chemistry of Solids **19**, 308 (1961).

[Dem01] S. Demokritov, B. Hillebrands and A. Slavin: *Brillouin light scattering studies of confined spin waves: linear and nonlinear confinement*, Physics Reports **348**, 441 (2001).

[Din11] J. Ding, M. Kostylev and A. O. Adeyeye: *Magnonic Crystal as a Medium with Tunable Disorder on a Periodical Lattice*, Phys. Rev. Lett. **107**, 047205 (2011).

[Din12] J. Ding, M. Kostylev and A. O. Adeyeye: *Realization of a mesoscopic reprogrammable magnetic logic based on a nanoscale reconfigurable magnonic crystal*, Appl. Phys. Lett. **100**, 073114 (2012).

[Dre12] L. Dreher, M. Weiler, M. Pernpeintner, H. Huebl, R. Gross, M. S. Brandt and S. T. B. Goennenwein: *Surface acoustic wave driven ferromagnetic resonance in nickel thin films: Theory and experiment*, Phys. Rev. B **86**, 134415 (2012).

[Dur] Durham Atomic and Molecular Physics group, Durham University: *Gaussian beams and the knife-edge measurement*, accessed on July 2nd 2014, `massey.dur.ac.uk/resources/grad_skills/KnifeEdge.pdf`.

[Dür12] G. F. Dürr: *Spin Waves in Nanochannels, Created by Individual and Periodic Bi-component Ferromagnetic Devices*, Dissertation, Technische Universität München (2012).

[Eer06] W. Eerenstein, N. D. Mathur and J. F. Scott: *Multiferroic and magnetoelectric materials*, Nature **442**, 759 (2006).

[Far13] M. Farle, T. Silva and G. Woltersdorf: *Spin Dynamics in the Time and Frequency Domain*, Springer Tracts in Modern Physics **246**, 37 (2013).

[Fli12] J. Flipse, F. L. Bakker, A. Slachter, F. K. Dejene and B. J. van Wees: *Direct observation of the spin-dependent Peltier effect*, Nature Nanotechnology **7**, 166 (2012).

[Fra12] K. J. A. Franke, T. H. E. Lahtinen and S. van Dijken: *Field tuning of ferromagnetic domain walls on elastically coupled ferroelectric domain boundaries*, Phys. Rev. B **85**, 094423 (2012).

[Gie05] F. Giessen: *Magnetization dynamics of nanostructured ferromagnetic rings and rectangular elements*, Dissertation, Universität Hamburg (2005).

[Gil04] T. Gilbert: *A phenomenological theory of damping in ferromagnetic materials*, IEEE Trans. Magn. **40**, 3443 (2004).

[Goe07] S. T. B. Goennenwein, S. W. Schink, A. Brandlmaier, A. Boger, M. Opel, R. Gross, R. S. Keizer, T. M. Klapwijk, A. Gupta, H. Huebl, C. Bihler and M. S. Brandt: *Electrically detected ferromagnetic resonance*, Appl. Phys. Lett. **90**, 162507 (2007).

[Goe08] S. T. B. Goennenwein, M. Althammer, C. Bihler, A. Brandlmaier, S. Geprägs, M. Opel, W. Schoch, W. Limmer, R. Gross and M. S. Brandt: *Piezo-voltage control of magnetization orientation in a ferromagnetic semiconductor*, Phys. Status solidi RRL **2**, 96 (2008).

[Gra06] L. Gravier, S. Serrano-Guisan, F. Reuse and J.-P. Ansermet: *Thermodynamic description of heat and spin transport in magnetic nanostructures*, Phys. Rev. B **73**, 024419 (2006).

[Gui07] Y. S. Gui, N. Mecking, A. Wirthmann, L. H. Bai and C.-M. Hu: *Electrical detection of the ferromagnetic resonance: Spin-rectification versus bolometric effect*, Appl. Phys. Lett. **91**, 082503 (2007).

[Gur96] A. Gurevich and G. Melkov: *Magnetization Oscillations and Waves*, Taylor & Francis, 1996.

[He10] H. He, K. Zhernenkov, M. Vadalá, N. Akdogan, D. Gorkov, R. M. Abrudan, B. P. Toperverg, H. Zabel, H. Kubota and S. Yuasa: *The effect of annealing on the junction profile of CoFeB/MgO tunnel junctions*, J. Appl. Phys. **108**, 063922 (2010).

[Hei88] B. Heinrich, S. T. Purcell, J. R. Dutcher, K. B. Urquhart, J. F. Cochran and A. S. Arrott: *Structural and magnetic properties of ultrathin Ni/Fe bilayers grown epitaxially on Ag(001)*, Phys. Rev. B **38**, 12879 (1988).

[Hel76] K. Hellwege: *Einführung in die Festkörperphysik*, Springer, 1976.

[Hil02] B. Hillebrands and K. Ounadjela: *Spin Dynamics in Confined Magnetic Structures I*, Springer, 2002.

[Hil05] B. Hillebrands: *Brillouin light scattering spectroscopy*, in Y. Zhu (Ed.), *Modern Techniques for Characterizing Magnetic Materials*, Springer US, 2005, 543–578.

[Hua12] S. Y. Huang, W. G. Wang, D. Qu, S. F. Lee, J. Kwo and C. L. Chien: *Thermal spin transport and applications*, 2012 IEEE International Electron Devices Meeting (IEDM) , 11.2.1 (2012).

[Hub98] A. Hubert and R. Schäfer: *Magnetic Domains: The Analysis of Magnetic Microstructures*, Springer, 1998.

[Hub13a] R. Huber: *Control of Spin Waves on the Nanoscale in One-Dimensional Magnonic Crystals and Atomic Layer Deposition of Metallic Ferromagnets for Second Generation of Nanomaterials*, Dissertation, Technische Universität München (2013).

[Hub13b] R. Huber, M. Krawczyk, T. Schwarze, H. Yu, G. Duerr, S. Albert and D. Grundler: *Reciprocal Damon-Eshbach-type spin wave excitation in a magnonic crystal due to tunable magnetic symmetry*, Appl. Phys. Lett. **102**, 012403 (2013).

[Jaf71] B. Jaffe, W. Cook and H. Jaffe: *Piezoelectric ceramics*, Non-metallic solids, Academic Press, 1971.

[Jan11] S. Y. Jang, C.-Y. You, S. H. Lim and S. R. Lee: *Annealing effects on the magnetic dead layer and saturation magnetization in unit structures relevant to a synthetic ferrimagnetic free structure*, J. Appl. Phys. **109**, 013901 (2011).

[Jaw10] C. M. Jaworski, J. Yang, S. Mack, D. D. Awschalom, J. P. Heremans and R. C. Myers: *Observation of the spin-Seebeck effect in a ferromagnetic semiconductor*, Nature Mater. **9**, 898 (2010).

[Jaw11] C. M. Jaworski, J. Yang, S. Mack, D. D. Awschalom, R. C. Myers and J. P. Heremans: *Spin-Seebeck Effect: A Phonon Driven Spin Distribution*, Phys. Rev. Lett. **106**, 186601 (2011).

[Jil98] D. Jiles: *Introduction to Magnetism and Magnetic Materials, Second Edition*, Taylor & Francis, 1998.

[Joh87] M. Johnson and R. H. Silsbee: *Thermodynamic analysis of interfacial transport and of the thermomagnetoelectric system*, Phys. Rev. B **35**, 4959 (1987).

[Jos95] A. Joshi: *Matrices and Tensors in Physics*, Wiley, 1995.

[Jul75] M. Julliere: *Tunneling between ferromagnetic films*, Physics Letters A **54**, 225 (1975).

[KÖ8] W. Z. Körner: *Physik III, Optik, Quantenphänomene und Aufbau der Atome*, R. Oldenbourg Verlag München Wien, 1998.

[Kal06] S. Kalarickal, P. Krivosik, M. Wu, C. E. Patton, M. L. Schneider, P. Kabos, T. J. Silva and J. P. Nibarger: *Ferromagnetic resonance linewidth in metallic thin films: Comparison of measurement methods*, J. Appl. Phys. **99**, 093909 (2006).

[Kar54] R. Karplus and J. M. Luttinger: *Hall Effect in Ferromagnetics*, Phys. Rev. **95**, 1154 (1954).

[Kay49] H. Kay and P. Vousden: *XCV. Symmetry changes in barium titanate at low temperatures and their relation to its ferroelectric properties*, Philosophical Magazine Series 7 **40**, 1019 (1949).

[Kel00] P. Kelly and R. Arnell: *Magnetron sputtering: a review of recent developments and applications*, Vacuum **56**, 159 (2000).

[Ken07] K. J. Kennewell, M. Kostylev and R. L. Stamps: *Calculation of spin wave mode response induced by a coplanar microwave line*, J. Appl. Phys. **101**, 09D107 (2007).

[Ker77] J. Kerr: *XLIII. On rotation of the plane of polarization by reflection from the pole of a magnet*, Philosophical Magazine Series 5 **3**, 321 (1877).

[Ker78] J. Kerr: *XXIV. On reflection of polarized light from the equatorial surface of a magnet*, Philosophical Magazine Series 5 **5**, 161 (1878).

[Khi08] A. Khitun, M. Bao and K. Wang: *Spin Wave Magnetic NanoFabric: A New Approach to Spin-Based Logic Circuitry*, IEEE Trans. Magn. **44**, 2141 (2008).

[Kim07] T. Kimura, Y. Otani, T. Sato, S. Takahashi and S. Maekawa: *Room-Temperature Reversible Spin Hall Effect*, Phys. Rev. Lett. **98**, 156601 (2007).

[Kit99] C. Kittel: *Einführung in die Festkörperphysik*, Oldenbourg, 1999.

[Kov10] A. A. Kovalev and Y. Tserkovnyak: *Magnetocaloritronic nanomachines*, Solid State Commun. **150**, 500 (2010).

[Kra13] M. Krawczyk, S. Mamica, M. Mruczkiewicz, J. W. Klos, S. Tacchi, M. Madami, G. Gubbiotti, G. Duerr and D. Grundler: *Magnonic band structures in two-dimensional bi-component magnonic crystals with in-plane magnetization*, Journal of Physics D: Applied Physics **46**, 495003 (2013).

[Kru10] V. V. Kruglyak, S. O. Demokritov and D. Grundler: *Magnonics*, Journal of Physics D: Applied Physics **43**, 264001 (2010).

[Kua05] B. Kuanr, R. E. Camley and Z. Celinski: *Narrowing of the frequency-linewidth in structured magnetic strips: Experiment and theory*, Appl. Phys. Lett. **87**, 012502 (2005).

[LÖ7] H.-F. Lü and Y. Guo: *Pure spin current in a three-terminal spin device in the presence of Rashba spin-orbit interaction*, Appl. Phys. Lett. **91**, 092128 (2007).

[Lac82] E. du Trémolet de Lacheisserie: *Magnetoelastic properties of amorphous alloys*, Journal of Magnetism and Magnetic Materials **25**, 251 (1982).

[Lah11a] T. Lahtinen, J. Tuomi and S. van Dijken: *Electrical Writing of Magnetic Domain Patterns in Ferromagnetic/Ferroelectric Heterostructures*, IEEE Trans. Magn. **47**, 3768 (2011).

[Lah11b] T. H. E. Lahtinen, J. O. Tuomi and S. van Dijken: *Pattern Transfer and Electric-Field-Induced Magnetic Domain Formation in Multiferroic Heterostructures*, Adv. Mater. **23**, 3187 (2011).

[Lah12] T. H. E. Lahtinen, K. J. A. Franke and S. van Dijken: *Electric-field control of magnetic domain wall motion and local magnetization reversal*, Scientific Reports **2** (2012).

[Lah13] T. H. E. Lahtinen: *Ferromagnetic-Ferroelectric Domain Coupling in Multiferroic Heterostructures*, Dissertation, Aalto University School of Science (2013).

[Lan35] L. Landau and E. Lifshitz: *Theory of the dispersion of magnetic permeability in ferromagnetic bodies*, Physikalische Zeitschrift der Sowjetunion **8**, 153 (1935).

[Lan08] P. Landeros, R. E. Arias and D. L. Mills: *Two magnon scattering in ultrathin ferromagnets: The case where the magnetization is out of plane*, Phys. Rev. B **77**, 214405 (2008).

[Lee13] C.-M. Lee, L.-X. Ye, H.-K. Chen and T.-H. Wu: *The Effects of Deposition Rate and Annealing on CoFeB/MgO/CoFeB Perpendicular Magnetic Tunnel Junctions*, IEEE Trans. Magn. **49**, 4429 (2013).

[Liu03] X. Liu, J. Rantschler, C. Alexander and G. Zangari: *High-frequency behavior of electrodeposited Fe-Co-Ni alloys*, IEEE Trans. Magn. **39**, 2362 (2003).

[Liu11] X. Liu, W. Zhang, M. J. Carter and G. Xiao: *Ferromagnetic resonance and damping properties of CoFeB thin films as free layers in MgO-based magnetic tunnel junctions*, J. Appl. Phys. **110**, 033910 (2011).

[MÏ0] P. Möhrke, J. Rhensius, J.-U. Thiele, L. Heyderman and M. Kläui: *Tailoring laser-induced domain wall pinning*, Solid State Commun. **150**, 489 (2010).

[Mac04] A. MacDonald and Q. Niu: *New twist for magnetic monopoles*, Phys. World **17**, 18 (2004).

[Mar00] M. Marder: *Condensed matter physics*, Wiley-Interscience, John Wiley, 2000.

[McG75] T. McGuire and R. Potter: *Anisotropic magnetoresistance in ferromagnetic 3d alloys*, IEEE Trans. Magn. **11**, 1018 (1975).

[Miy95] T. Miyazaki and N. Tezuka: *Giant magnetic tunneling effect in Fe/Al2O3/Fe junction*, Journal of Magnetism and Magnetic Materials **139**, L231 (1995).

[Miy07] T. Miyasato, N. Abe, T. Fujii, A. Asamitsu, S. Onoda, Y. Onose, N. Nagaosa and Y. Tokura: *Crossover Behavior of the Anomalous Hall Effect and Anomalous Nernst Effect in Itinerant Ferromagnets*, Phys. Rev. Lett. **99**, 086602 (2007).

[Moo73] J. P. Moore and R. S. Graves: *Absolute Seebeck coefficient of platinum from 80 to 340 K and the thermal and electrical conductivities of lead from 80 to 400 K*, J. Appl. Phys. **44**, 1174 (1973).

[Mos10] O. Mosendz, J. E. Pearson, F. Y. Fradin, G. E. W. Bauer, S. D. Bader and A. Hoffmann: *Quantifying Spin Hall Angles from Spin Pumping: Experiments and Theory*, Phys. Rev. Lett. **104**, 046601 (2010).

[Nag10] N. Nagaosa, J. Sinova, S. Onoda, A. H. MacDonald and N. P. Ong: *Anomalous Hall effect*, Rev. Mod. Phys. **82**, 1539 (2010).

[Nah10] G. Nahrwold, J. M. Scholtyssek, S. Motl-Ziegler, O. Albrecht, U. Merkt and G. Meier: *Structural, magnetic, and transport properties of Permalloy for spintronic experiments*, J. Appl. Phys. **108**, 013907 (2010).

[NDT] NDT Resource Center: Conductivity and Resistivity Values for Misc. Materials .

[Ner87] W. Nernst: *Über die electromotorischen Kräfte, welche durch den Magnetismus in von einem Wärmestrome durchflossenen Metallplatten geweckt werden*, Annalen der Physik **267**, 760 (1887).

[Neu04] G. Neuber, R. Rauer, J. Kunze, J. Backstrom and M. R´ubhausen: *Generalized magneto-optical ellipsometry in ferromagnetic metals*, Thin Solid Films **455-456**, 39 (2004).

[Neu08] S. Neusser, B. Botters and D. Grundler: *Localization, confinement, and field-controlled propagation of spin waves in $Ni_{80}Fe_{20}$ antidot lattices*, Phys. Rev. B **78**, 054406 (2008).

[Neu09] S. Neusser and D. Grundler: *Magnonics: Spin Waves on the Nanoscale*, Adv. Mater. **21**, 2927 (2009).

[Neu10] S. Neusser, G. Duerr, H. G. Bauer, S. Tacchi, M. Madami, G. Woltersdorf, G. Gubbiotti, C. H. Back and D. Grundler: *Anisotropic Propagation and Damping of Spin Waves in a Nanopatterned Antidot Lattice*, Phys. Rev. Lett. **105**, 067208 (2010).

[Neu11a] S. Neusser: *Spin Waves in Antidot Lattices: From Quantization to Magnonic Crystals*, Dissertation, Technische Universität München (2011).

[Neu11b] S. Neusser, H. G. Bauer, G. Duerr, R. Huber, S. Mamica, G. Wolterstorf, M. Krawczyk, C. H. Back and D. Grundler: *Tunable metamaterial response of a $Ni_{80}Fe_{20}$ antidot lattice for spin waves*, Phys. Rev. B **84**, 184411 (2011).

[Oak05] T. C. Oakberg: *Magneto-optic Kerr effect*, Hinds Instruments (2005).

[O'H99] R. C. O'Handley: *Modern Magnetic Materials: Principles and Applications*, Wiley-Interscience, 1999.

[PÖ99] S. Pöykkö and D. J. Chadi: *Ab initio study of 180° domain wall energy and structure in PbTiO3*, Appl. Phys. Lett. **75**, 2830 (1999).

[Pai99] D. Pain, M. Ledieu, O. Acher, A. L. Adenot and F. Duverger: *An improved permeameter for thin film measurements up to 6 GHz*, J. Appl. Phys. **85**, 5151 (1999).

[Pat68] C. E. Patton: *Linewidth and Relaxation Processes for the Main Resonance in the Spin-Wave Spectra of Ni[single bond]Fe Alloy Films*, J. Appl. Phys. **39**, 3060 (1968).

[Pat75] C. E. Patton, Z. Frait and C. H. Wilts: *Frequency dependence of the parallel and perpendicular ferromagnetic resonance linewidth in Permalloy films, 2-36 GHz*, J. Appl. Phys. **46**, 5002 (1975).

[Per95] N. A. Pertsev and A. G. Zembilgotov: *Energetics and geometry of 90° domain structures in epitaxial ferroelectric and ferroelastic films*, J. Appl. Phys. **78**, 6170 (1995).

[Plo06] J. J. Plombon, E. Andideh, V. M. Dubin and J. Maiz: *Influence of phonon, geometry, impurity, and grain size on Copper line resistivity*, Appl. Phys. Lett. **89**, 113124 (2006).

[Pom93] W. Pompe, X. Gong, Z. Suo and J. S. Speck: *Elastic energy release due to domain formation in the strained epitaxy of ferroelectric and ferroelastic films*, J. Appl. Phys. **74**, 6012 (1993).

[Qu13] D. Qu, S. Y. Huang, J. Hu, R. Wu and C. L. Chien: *Intrinsic Spin Seebeck Effect in* $\mathrm{Au/YIG}$, Phys. Rev. Lett. **110**, 067206 (2013).

[RÜ12] D. Rüffer, R. Huber, P. Berberich, S. Albert, E. Russo-Averchi, M. Heiss, J. Arbiol, A. Fontcuberta i Morral and D. Grundler: *Magnetic states of an individual Ni nanotube probed by anisotropic magnetoresistance*, Nanoscale **4**, 4989 (2012).

[Ros04] S. M. Rossnagel and T. S. Kuan: *Alteration of Cu conductivity in the size effect regime*, Journal of Vacuum Science & Technology B **22**, 240 (2004).

[Rov10] P. Rovillain, R. de Sousa, Y. Gallais, A. Sacuto, M. A. Méasson, D. Colson, A. Forget, M. Bibes, A. Barthélémy and M. Cazayous: *Electric-field control of spin waves at room temperature in multiferroic BiFeO3*, Nature Mater. **9**, 975 (2010).

[Rum10] A. K. Rumaiz, J. C. Woicik, W. G. Wang, J. Jordan-Sweet, G. H. Jaffari, C. Ni, J. Q. Xiao and C. L. Chien: *Effects of annealing on the local structure of Fe and Co in CoFeB/MgO/CoFeB tunnel junctions: An extended x-ray-absorption fine structure study*, Appl. Phys. Lett. **96**, 112502 (2010).

[Sai06] E. Saitoh, M. Ueda, H. Miyajima and G. Tatara: *Conversion of spin current into charge current at room temperature: Inverse spin-Hall effect*, Appl. Phys. Lett. **88**, 182509 (2006).

[Sar43] R. Sarbacher and W. Edson: *Hyper and Ultrahigh Frequency Engineering*, J. Wiley & Sons, Incorporated, 1943.

[Sch] A. Scharmann: *Tabellen und Diagramme zu Kapitel 8, Struktur und Eigenschaften der Materie, Physikalisch Technische Bundesanstalt (PTB)*, accessed on July 18th 2014, `www.ptb.de/cms/fileadmin/internet/publikationen/buecher/Kohlrausch/Tabellen/Kohlrausch_3_Tabellen_und_Diagramme_Struktur_und_Eigenschaften_der_Materie.pdf`.

[Sch13a] M. Schmid, S. Srichandan, D. Meier, T. Kuschel, J.-M. Schmalhorst, M. Vogel, G. Reiss, C. Strunk and C. H. Back: *Transverse Spin Seebeck Effect versus Anomalous and Planar Nernst Effects in Permalloy Thin Films*, Phys. Rev. Lett. **111**, 187201 (2013).

[Sch13b] T. Schwarze: *SpinWaves in 2D and 3D Magnonic Crystals: From Nanostructured Ferromagnetic Materials to Chiral Helimagnets*, Dissertation, Technische Universität München (2013).

[Shi04] J. Shibata and Y. Otani: *Magnetic vortex dynamics in a two-dimensional square lattice of ferromagnetic nanodisks*, Phys. Rev. B **70**, 012404 (2004).

[Sim04] R. Simons: *Coplanar Waveguide Circuits, Components, and Systems*, Wiley Series in Microwave and Optical Engineering, Wiley, 2004.

[Sko08] R. Skomski: *Simple models of magnetism*, Oxford University Press, Oxford, 2008.

[Sla10] A. Slachter, F. L. Bakker, J.-P. Adam and B. J. van Wees: *Thermally driven spin injection from a ferromagnet into a non-magnetic metal*, Nature Phys. **6**, 879 (2010).

[Sla11] A. Slachter, F. L. Bakker and B. J. van Wees: *Anomalous Nernst and anisotropic magnetoresistive heating in a lateral spin valve*, Phys. Rev. B **84**, 020412 (2011).

[Smi55] J. Smit: *The spontaneous hall effect in ferromagnetics I*, Physica **21**, 877 (1955).

[Smi58] J. Smit: *The spontaneous hall effect in ferromagnetics II*, Physica **24**, 39 (1958).

[Smi65] D. O. Smith: *Longitudinal Kerr Effect Using a Very Thin Fe Film*, J. Appl. Phys. **36**, 1120 (1965).

[Sta09] D. Stancil and P. A.: *Spin Waves - Theory and Applications*, Springer-Verlag Berlin and Heidelberg GmbH & Co. KG, 2009.

[Sys] S. R. Systems: *About Lock-In Amplifiers, Amplication Note 3* Accessed on July 18th 2014, `www.thinksrs.com/downloads/PDFs/ApplicationNotes/AboutLIAs.pdf`.

[Tac10] S. Tacchi, M. Madami, G. Gubbiotti, G. Carlotti, S. Goolaup, A. O. Adeyeye, N. Singh and M. P. Kostylev: *Analysis of collective spin-wave modes at different points within the hysteresis loop of a one-dimensional magnonic crystal comprising alternative-width nanostripes*, Phys. Rev. B **82**, 184408 (2010).

[Teh99] S. Tehrani, J. Slaughter, E. Chen, M. Durlam, J. Shi and M. DeHerren: *Progress and outlook for MRAM technology*, IEEE Trans. Magn. **35**, 2814 (1999).

[Tho57] W. Thomson: *On the Electro-Dynamic Qualities of Metals:Effects of Magnetization on the Electric Conductivity of Nickel and of Iron*, Proceedings of the Royal Society of London (1854-1905) (1857).

[Top10] J. Topp, D. Heitmann, M. P. Kostylev and D. Grundler: *Making a Reconfigurable Artificial Crystal by Ordering Bistable Magnetic Nanowires*, Phys. Rev. Lett. **104**, 207205 (2010).

[Top11] J. Topp, G. Duerr, K. Thurner and D. Grundler: *Reprogrammable magnonic crystals formed by interacting ferromagnetic nanowires*, Pure Appl. Chem. **83**, 1989 (2011).

[Uch08] K. Uchida, S. Takahashi, K. Harii, J. Ieda, W. Koshibae, K. Ando, S. Maekawa and E. Saitoh: *Observation of the spin Seebeck effect*, Nature **455**, 778 (2008).

[Uch10] K.-i. Uchida, H. Adachi, T. Ota, H. Nakayama, S. Maekawa and E. Saitoh: *Observation of longitudinal spin-Seebeck effect in magnetic insulators*, Appl. Phys. Lett. **97**, 172505 (2010).

[Uch12] K. Uchida, T. Ota, H. Adachi, J. Xiao, T. Nonaka, Y. Kajiwara, G. E. W. Bauer, S. Maekawa and E. Saitoh: *Thermal spin pumping and magnon-phonon-mediated spin-Seebeck effect*, J. Appl. Phys. **111**, 103903 (2012).

[Ver12] R. Verba, G. Melkov, V. Tiberkevich and A. Slavin: *Fast switching of a ground state of a reconfigurable array of magnetic nano-dots*, Appl. Phys. Lett. **100**, 192412 (2012).

[Vog09] A. Vogel, J. Wulfhorst and G. Meier: *Enhanced spin injection and detection in spin valves with integrated tunnel barriers*, Appl. Phys. Lett. **94**, 122510 (2009).

[Vog14] K. Vogt, F. Y. Fradin, J. E. Pearson, T. Sebastian, S. D. Bader, B. Hillebrands, A. Hoffmann and H. Schultheiss: *Realization of a spin-wave multiplexer*, Nature Commun. **5** (2014).

[Wad91] B. Wadell: *Transmissión line design handbook*, Artech House, 1991.

[Wal57] L. R. Walker: *Magnetostatic Modes in Ferromagnetic Resonance*, Phys. Rev. **105**, 390 (1957).

[Wal11] M. Walter, J. Walowski, V. Zbarsky, M. Münzenberg, M. Schäfers, D. Ebke, G. Reiss, A. Thomas, P. Peretzki, M. Seibt, J. S. Moodera, M. Czerner, M. Bachmann and C. Heiliger: *Seebeck effect in magnetic tunnel junctions*, Nature Mater. **10**, 742 (2011).

[Wan06] D. Wang: *Magnetoresistive thin film materials and their device applications*, in Y. Liu, D. Sellmyer and D. Shindo (Ed.), *Handbook of Advanced Magnetic Materials*, Springer US, 2006, 1635–1666.

[Wei09] M. Weiler, A. Brandlmaier, S. Geprägs, M. Althammer, M. Opel, C. Bihler, H. Hübl, M. S. Brandt, R. Gross and S. T. B. Goennenwein: *Voltage controlled inversion of magnetic anisotropy in a ferromagnetic thin film at room temperature*, New Journal of Physics **11**, 013021 (2009).

[Wei12] M. Weiler, M. Althammer, F. D. Czeschka, H. Huebl, M. S. Wagner, M. Opel, I.-M. Imort, G. Reiss, A. Thomas, R. Gross and S. T. B. Goennenwein: *Local Charge and Spin Currents in Magnetothermal Landscapes*, Phys. Rev. Lett. **108**, 106602 (2012).

[Wil32] S. R. Williams: *THE JOULE MAGNETOSTRICTIVE EFFECT IN A GROUP OF COBALT-IRON ALLOYS*, Review of Scientific Instruments **3**, 675 (1932).

[Wol01] S. A. Wolf, D. D. Awschalom, R. A. Buhrman, J. M. Daughton, S. von Molnár, M. L. Roukes, A. Y. Chtchelkanova and D. M. Treger: *Spintronics: A Spin-Based Electronics Vision for the Future*, Science **294**, 1488 (2001).

[Xia10] J. Xiao, G. E. W. Bauer, K. Uchida, E. Saitoh and S. Maekawa: *Theory of magnon-driven spin Seebeck effect*, Phys. Rev. B **81**, 214418 (2010).

[Xu12] F. Xu, Q. Huang, Z. Liao, S. Li and C. K. Ong: *Tuning of magnetization dynamics in sputtered CoFeB thin film by gas pressure*, J. Appl. Phys. **111**, 07A304 (2012).

[Yan08] T. Yang, T. Kimura and Y. Otani: *Giant spin-accumulation signal and pure spin-current-induced reversible magnetization switching*, Nature Physics **4**, 851 (2008).

[Yin13] S. L. Yin, Q. Mao, Q. Y. Meng, D. Li and H. W. Zhao: *Hybrid anomalous and planar Nernst effect in permalloy thin films*, Phys. Rev. B **88**, 064410 (2013).

[Yu12] H. Yu, R. Huber, T. Schwarze, F. Brandl, T. Rapp, P. Berberich, G. Duerr and D. Grundler: *High propagating velocity of spin waves and temperature dependent damping in a CoFeB thin film*, Appl. Phys. Lett. **100**, 262412 (2012).

[Yu13] H. Yu, G. Duerr, R. Huber, M. Bahr, T. Schwarze, F. Brandl and D. Grundler: *Omnidirectional spin-wave nanograting coupler*, Nature Commun. **4** (2013).

[Zhu05] Y. Zhu: *Modern Techniques for Characterizing Magnetic Materials*, Springer ebook collection / Chemistry and Materials Science 2005-2008, Springer, 2005.

Publications

- S. Neusser, G. Duerr, F. Brandl, R. Huber, T. Schwarze, and D. Grundler: Transmission of GHz spin waves through periodically nanopatterned ferromagnets, Metamaterials '2011: The Fifth International Congress on Advanced Electromagnetic Materials in Microwaves and Optics, Metamorphose-VI, ISBN 978-952-67611-0-7, p. 922 (2011)
- T. Schwarze, R. Huber, G. Duerr, F. Brandl, S. Neusser, K. Thurner, and D. Grundler: Microwave Antennas for Broadband Spectroscopy on Magnonic Metamaterials, Metamaterials '2011: The Fifth International Congress on Advanced Electromagnetic Materials in Microwaves and Optics, Metamorphose-VI, ISBN 978-952-67611-0-7, p. 576 (2011)
- T. Schwarze, M. Okuda, R. Huber, J.-C. Eloi, F. Brandl, L. Dreher, M.S. Brandt, D. Grundler, and W. Schwarzacher: Fabrication and characterization of crystallized magnetoferritin as an artificial magnetic metamaterial, Metamaterials '2011: The Fifth International Congress on Advanced Electromagnetic Materials in Microwaves and Optics, Metamorphose-VI, ISBN 978-952-67611-0-7, p. 125 (2011)
- H. Yu, R. Huber, T. Schwarze, F. Brandl, T. Rapp, P. Berberich, G. Duerr, and D. Grundler: High propagating velocity of spin waves and temperature dependent damping in a CoFeB thin film, Appl. Phys. Lett. 100, 262412 (2012)
- A. van Bieren, F. Brandl, D. Grundler, and J.-P. Ansermet: Space- and time-resolved Seebeck and Nernst voltages in laser-heated permalloy/gold microstructures, Appl. Phys. Lett. 102, 052408 (2013)
- F. Brandl, K.J.A. Franke, T.H.E. Lahtinen, S. van Dijken, and D. Grundler: Spin waves in CoFeB on ferroelectric domains combining spin mechanics and magnonics, Solid State Communications 198, 13 (2014)
- H. Yu, G. Duerr, R. Huber, M. Bahr, T. Schwarze, F. Brandl, and D. Grundler: Omnidirectional spin-wave nanograting coupler, Nature Commun. 4, 2702 (2013)
- F. Brandl and D. Grundler: Fabrication and local laser heating of freestanding Ni80Fe20 bridges with Pt contacts displaying anisotropic magnetoresistance and anomalous Nernst effect, Appl. Phys. Lett. 104, 172401 (2014)

- H. Yu, O. d'Allivy Kelly, V. Cros, R. Bernard, P. Bortolotti, A. Anane, F. Brandl, R. Huber, I. Stasinopoulos, D. Grundler: Magnetic thin-film insulator with ultra-low spin wave damping for coherent nanomagnonics, Nature Commun. (submitted)

Acknowledgements

I would like to express gratitude to all people who contributed to this work. In particular:

- Prof. Dr. Martin Zacharias for the supervision of the PhD examination, Prof. Dr. Dirk Grundler for being the first examiner, Prof. Dr. Martin S. Brandt for being the second examiner.
- Prof. Dr. Dirk Grundler for the supervision of my thesis, the profound discussions, his encouraging and motivating advices and his great support.
- Dr. Haiming Yu for being a great room-mate and for the fruitful discussions.
- The members of the SpinCat group: Klara Beltinger, Johannes Mendil and Shengda Wang for their out-standing working attitude, many discussions and their numerous ideas for the improvement of the laser setup.
- The rest of the spin dynamics group: Georg Dürr, Florian Heimbach, Rupert Huber, Stefan Mändl, Sebastian Neusser, Thomas Schwarze, Ioannis Stasinopoulos, Tobias Stückler, Klaus Thurner for providing a great working atmosphere.
- Prof. Dr. Sebastiaan van Dijken and his group for providing the $BaTiO_3$ based samples and the fruitful collaboration.
- Kévin Franke for providing MOKE data.
- Sampo Hämäläinen for providing micromagnetic simulations.
- Dr. Arndt von Bieren for his initial support with the Comsol Multiphysics simulations.
- Dr. Paul Berberich for his help and advices.
- Thomas Rapp for his great support with the laser setup and all electronic issues.
- Dr. Helmut Schultheiß for his support with the stabilization software.
- Everybody at E10 for providing an extraordinary atmosphere: Stephan Albert, Matthias Brasse, Stefanos Chalkidis, Florian Herzog, Amadeus Mlynarski, Benedikt Rupprecht, Schorsch Sauther, Dr. Marc Wilde.
- Johannes Seitz, Stefan Lichtenauer and Thomas Neukel for their technical support.

- Claudine Voelcker and Roswitha Hoppen for organizational support.
- Mehdi Kashani-Shirazi for recruiting me for E10.
- Prof. Dr. Alexander Holleitner and Peter Weiser for the possibility to use the electron beam lithography at the Center for Nanotechnology and Nanomaterials and for support and the corresponding maintenance.
- Claudia Paulus at WSI for the manufacturing of the photolithography masks.
- Prof. Dr. Sergei Nikitov, Dr. Yuri Filimonov, Dr. Yuri Khivintsev, and Dr. Aleksandr Kozhevnikov at the Kotel'nikov Institute of Radio Engineering and Electronics of RAS in Moscow and Saratov for their support in Russia.
- Last but definitely not least: My family, my wife Lisa and my friends for their unconditional support in every situation in my life.

The research leading to these results has received funding from the European Community's Seventh Framework Programme (FP7/2007-2013) under Grant No. 228673 (MAGNONICS), Grant No. 247556 (NoWaPhen), and the German Excellence Cluster Nanosystems Initiative Munich (NIM), and by the DFG in the German priority program SPP 1538 spin caloric transport via project GR1640/5-1. The support is gratefully acknowledged.